TOWARDS THE DESIGN OF ULTRA-LOW DIELECTRIC CONSTANT MATERIALS

A Dissertation

Presented to the Faculty of the Graduate School

of Cornell University

In Partial Fulfillment of the Requirements for the Degree of

Doctor of Philosophy

by

Alexandra M Raymunt

January 2015

TOWARDS THE DESIGN OF ULTRA-LOW DIELECTRIC CONSTANT MATERIALS

Alexandra M Raymunt, Ph. D.

Cornell University 2015

The inherent trade-off of porosity and mechanical properties in ultra-low dielectric constant (ULK) organosilicate glass (SiCOH) materials is a critical challenge in semiconductor processing. Numerous post-deposition processes have been studied to achieve simultaneous low-k materials with adequate mechanical rigidity, including thermal annealing. Typically, these thermal anneals are characterized by times on the order of seconds to minutes at relatively low temperatures (below 500°C). The goal of this work was to study the potential advantages of sub-millisecond time-frame anneals at extreme temperatures up to 1200°C.

I began by establishing an atomic layout for the amorphous film, and then developed methods of verifying its relevant properties, like porosity, dielectric constant, Bulk and Young's Moduli. I then studied the effects of rapid thermal processing on the structure of ultra-low k materials using Molecular Dynamics computer simulations employing a force-field which enables bond rearrangements, called REAX-FF. This was compared with direct experimental measurements during CO_2 laser-induced spike annealing. Results show structural evolution with increasing temperature leading to densification of the SiO_x network, reduction in the concentration of sub-oxides, and loss of remnant organic moieties from original SiCOH structures. These results provide atomic-scale structure and chemical intuition to guide the development of future low-k materials.

Current efforts are focused on exploring potential new classes of ULK materials, using the information gleaned from our study of organosilicate glasses as a

guide. Ideally a ULK material should be: thermally stable to high temperatures, mechanically strong, chemically resistant, have low polarizabilities and high porosity, with pores no larger than 2nm in diameter. Porous organic polymers, or POPs, are highly interconnected and therefore mechanically stable, but have large ringed structures which frustrate packing and promote high intrinsic material porosities. I have created models of these materials using Molecular Dynamics in order to predict their dielectric and mechanical properties, and therefore their potential viability as future ULK materials.

BIOGRAPHICAL SKETCH

Alexandra Raymunt graduated *summa cum laude* with a Bachelor of Science degree in Chemical Engineering and a Bachelor of Arts degree in German Studies from the University of Connecticut in 2009. She joined the doctoral program in Chemical Engineering at Cornell University in 2009, and received a Master of Science degree from this program in 2013.

Dr. Raymunt has received a number of honors and awards during her time at Cornell. Most notably, in 2010 she received an NSF Graduate Fellowship Award and in 2012 she received an IBM Graduate Fellowship Award.

While studying at Cornell Dr. Raymunt conducted an internship with IBM during the summer of 2011. She has also been extensively involved with Semiconductor Research Corporation events and proceedings, and this has led to her current position as a fulltime member of the research staff at Intel.

Dr. Raymunt presented her research at a number of conferences, including the Spring 2012 Materials Research Society (MRS) Conference, the Fall 2013 MRS Conference, and the 2013 Annual American Institute of Chemical Engineers Conference.

Dr. Raymunt's dissertation *Towards the Design of Ultra-Low Dielectric Constant Materials* was supervised by Prof. Paulette Clancy.

To Mom and Dad: without your constant love, support, and guidance this never would have been possible.

To my husband Jon: without your constant love, patience, and kindness I never would have made it through.

ACKNOWLEDGMENTS

Thesis Committee: Paulette Clancy, Michael Thompson, Christopher Ober, Fernando Escobedo

IBM Researchers: Griselda Bonilla, Peter Brofmann, Xiao-Hu Liu, Dennis Newns, Glenn Martyna, Alfred Grill

Clancy Group Members: Krishna Iyengar, Rebecca Cantrell Stehle, Ananth Kaushik, Brian Koo, Jonathan Saathoff, Robert Bell, James Stevenson, Christina Lenn, Binit Lucose, Cheg-Wei Lee, Victoria Sorg, Yaset Asvedo

Funding Resources: NSF, IBM, SRC, Intel

TABLE OF CONTENTS

LIST OF FIGURES

LIST OF TABLES

CHAPTER 1

AN INTRODUCTION TO AMORPHOUS ORGANOSILICATE GLASS MATERIALS:

Background and Introduction

Continued scaling of devices along Moore's Law presents increasing challenges to all elements of semiconductor device structures and, in particular, to interconnect density and pitch. [1] Interconnect delays and power usage forced the transition from aluminum interconnects to copper starting in late 1997. [2-4] Shortly thereafter, SiO_2 (dielectric constant k = 3.9) was replaced by lower dielectric constant insulators, referred to as ultra-low *k* (ULK) materials. Capacitive crosstalk between signals continues to be exacerbated by shrinking dimensions, leading to continued requirements for ever decreasing dielectric constants. Indeed, the ITRS roadmap [5-6] calls for dielectric constants to fall from approximately 2.5 today to below 2.0 by the end of the decade.

For the last decade, porous organosilicate glasses, often referred to as SiCOH, have been the dominant low-k material. [2, 7] This dominance has been due, in large part, to SiCOH's compatibility with modern semiconductor devices, thermal stability up to 350°C, reasonable oxygen plasma resistance, and acceptable strength-to-*k* tradeoff. The general structure of SiCOH is a Si-O skeleton with organic substitutions and porosity on the nanometer to sub-nanometer scale. The Si-O skeleton consists of both fully networked SiO_4 tetrahedra and suboxides (oxygen coordination less than 4). Organic substitutions are commonly in the Si-O network as, for example, Si-CH_3 pendant methyl groups or Si-CH_2-Si methane bridges. Continued reductions in the dielectric constant are achieved by the addition of substantial porosity, both intrinsically formed from the SiCOH precursors and extrinsically introduced through the use of sacrificial organic porogens. Post-deposition annealing is required to decompose the porogens, typically in

a furnace at ≈400°C or by UV exposure for tens of seconds. [7] These porogens foster porosity as nanoscale voids within an otherwise complete SiO network. [7] Retaining the Si-O framework preserves the known compatibility of SiO_2 and much of the requisite etch resistance. Volksen and Grill have extensively reviewed the history, structures and processing of SiCOH materials. [7-8]

Unfortunately, the increased porosity and carbon content in these films also reduces the mechanical integrity of the material, resulting in reduced modulus and fracture toughness. The dual damascene process for Cu metallization requires a critical mechanical strength, commonly quoted as a modulus above 5-10 GPa. [7] The challenge of simultaneously achieving this mechanical strength with the requisite low-k value is summarized in Figure 1. This scatter plot correlates measured modulus with the dielectric constant for a range of SiCOH materials studied over the past decade. [9-16] No materials currently meet the required targets for the ITRS roadmap. [5-6]

Numerous techniques have been explored to increase the modulus while maintaining the porosity, including furnace annealing [12, 16-19] and exposure to UV [14, 16, 20-21]or e-beam sources [15, 22]. In general, the goal is to increase the extent of SiO linkages within the film, and therefore the mechanical integrity, while avoiding pore collapse and subsequent dielectric constant increase. UV and e-beam exposure locally opens bonds, allowing cross-linking within the Si-O-Si and the Si-CH_2-Si networks. [7] For UV curing, a critical wavelength below 200 nm is required indicating that the mechanism involves direct bond-breaking and local chemical modification. While the chemical changes resulting from exposure can be followed, the mechanisms and final

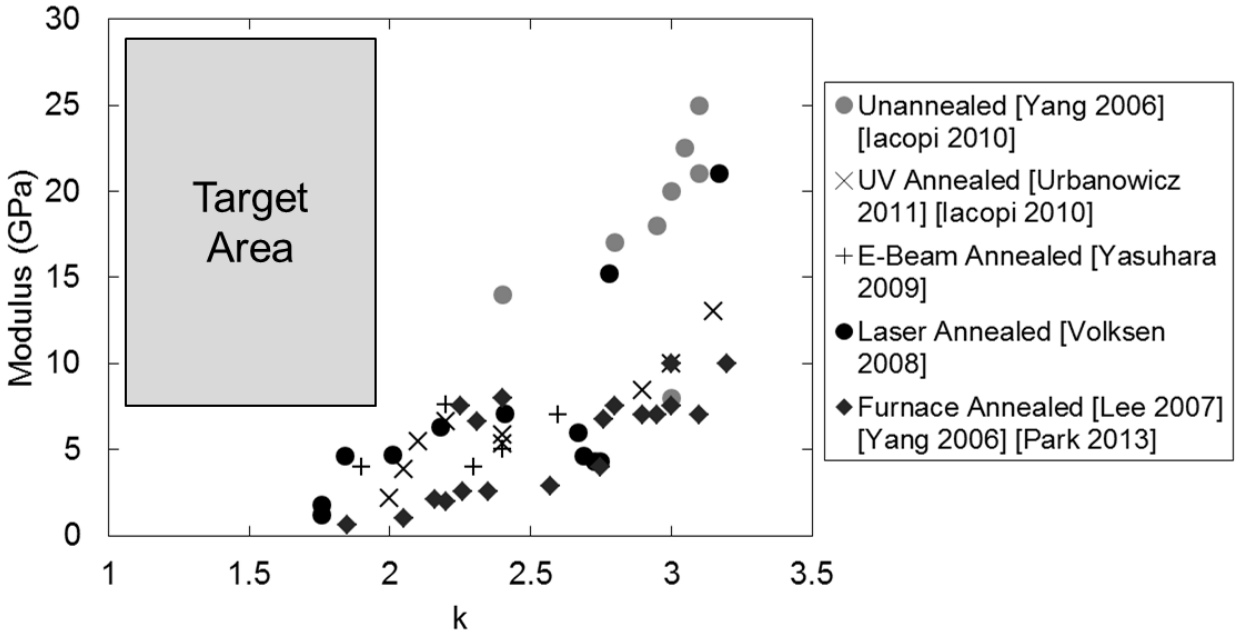

Figure 1. An overview of current characterization of SiCOH films in terms of their elastic modulus as a function of dielectric constant. A clear overall trend is apparent in which, as the dielectric constant of the material decreases (favorably for ultra-low-k applications), the elastic modulus also decreases (unfavorably). This illustrates the difficulty of developing a SiCOH film with a dielectric constant at or below 2, with sufficient mechanical strength (above ~ 8 GPa) to survive the manufacturing process. The shaded box shows that none of the materials characterized to date meets these twin criteria. UV Hybrid and E-Beam Hybrid films indicate annealing with a combination of furnace annealing and UV or E-Beam treatments. [9-16]

structures created by the anneals are not well understood. For thermal anneals, there are likely to be numerous active pathways whose temperature behavior and structural evolution are unknown.

While these anneal and curing methods have succeeded in moderate property improvements, none have been able to substantially shift the limiting curve. As thermal processes normally involve events with multiple activation energies, optimization of properties may be possible by shifting the time and temperature regimes for thermal anneals. Traditional anneals are performed on time scales from minutes to seconds and, for SiCOH materials, at temperatures below 500^{o}C. Laser-induced spike annealing (LSA) offers the potential for thermal processing on sub-millisecond time frames and transient temperatures above 1200^{o}C. In 2006 and 2008, Volksen *et al.* showed the feasibility of this approach with promising results. [9-10] Interestingly, there have been no follow-up studies of this annealing technique. To understand the relative dynamics of the multiple annealing processes involved in curing SiCOH films, it is critical to follow the chemical reactions as a function of time and temperature using both computational and experimental techniques. In this work, I report Molecular Dynamics results utilizing a force-field model (REAX) capable of capturing the salient features of bond reorganization. These results are compared with experimental measurements of a model film under millisecond thermal anneals.

Previous Work

Studies modeling SiCOH materials

Many computational studies have attempted to model SiCOH materials at the atomic scale. [18, 23-32] The first study, conducted by Tajima *et al.* [23, 33], created a set of theoretical SiCOH structures and compared the properties of these structures to experimental data on

structure, Young's Modulus, and dielectric constant. To generate possible structures, they used three types of Si-based starting units to describe the material: $RR'SiO_2$, $RSiO_3$, and SiO_4, where R and R' represent either H or CH_3. They determined a ratio of these units that satisfied experimental atomic composition data, placed the various structures at random throughout a repeating box, and linked these units together *via* oxygen bonds. This method is outlined in Figure 2. The resulting unit cells were treated using standard energy minimization techniques and then used as the input for MD simulations where they were allowed to relax further. The study generated approximately 500 structures, from which they chose the two structures that appeared to provide the best match to experiment for further studies. They based this on comparisons of the simulation and experimental Young's modulus, dielectric constant, and density.

Tajima *et al.* calculated the Young's moduli of the samples from the change in the mean lattice constants over just 20 ps of constant-pressure MD simulations under different external stresses between 0 and 1 GPa. The dielectric constants of the samples were calculated using density functional theory (DFT). They found that density, dielectric constant, and Young's modulus are strongly correlated. This was a discouraging (though expected) result since it implies that when the dielectric constant decreases (the desired target of current low-k studies), the mechanical properties also decrease (which is unwanted).

An underlying implied assumption of Tajima's work is that a roughly 100-atom unit cell, with dimensions 1.21 x 0.94 x 0.74 nm, is sufficiently large to capture the amorphous nature of a SiCOH film. However, it is highly unlikely that such a small sample can adequately depict the behavior of amorphous SiCOH structures. Indeed, it is a practical rule of thumb that molecular simulations of amorphous materials require the consideration of thousands of atoms.

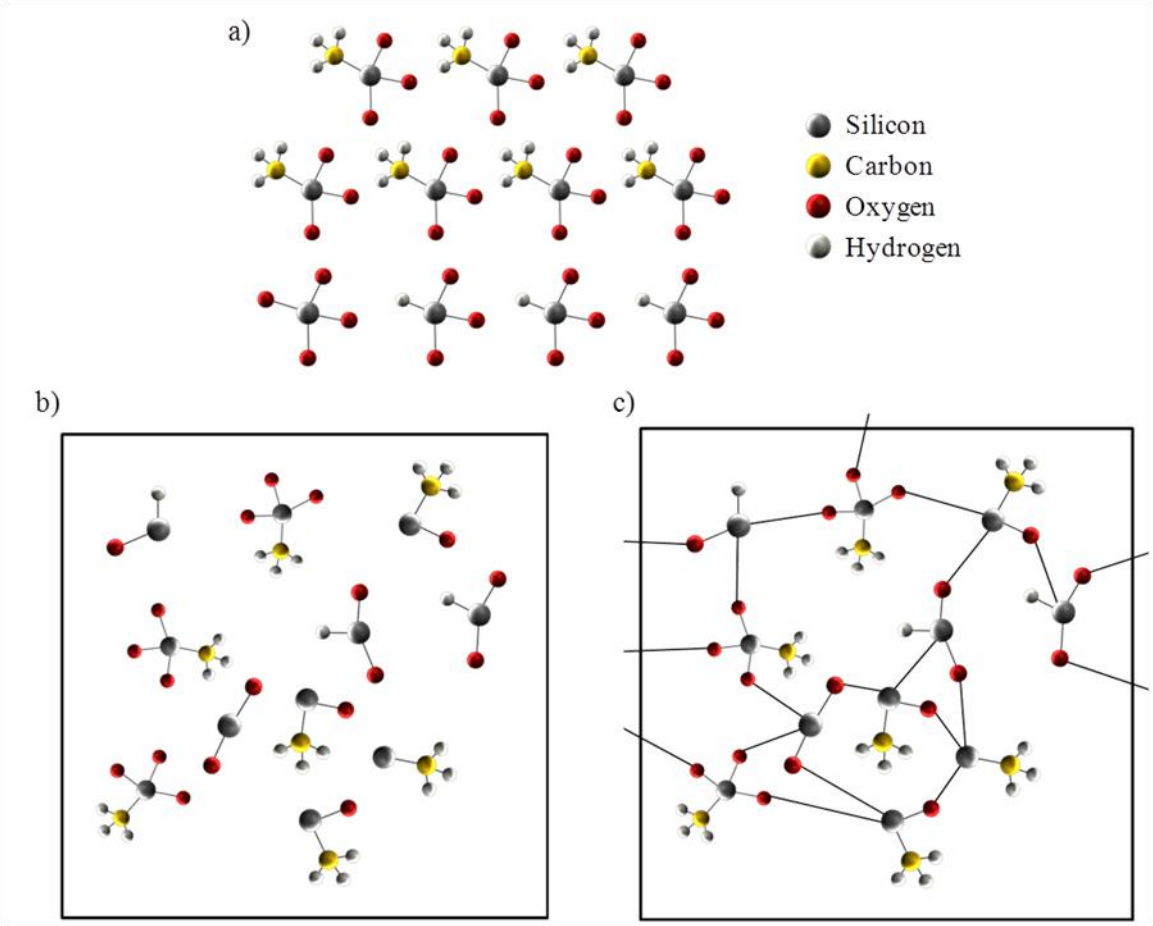

Figure 2. Figure 2 outlines the method used by Tajima *et al.* [10-11] to generate SiCOH structures. They begin with a pre-determined number of specific structural motifs, shown in image (a) above. These motifs are then randomly distributed throughout a simulation box, as shown in image (b). Finally the motifs are connected to one another via silicon-oxygen bonding (image (c)).

Experimental samples exhibit a random configuration of bonding patterns throughout a sample hundreds of nanometers long, with an average pore diameter between 1 and 2 nm. In addition, the Tajima method does not include some significant, experimentally observed, structural motifs, such as methylated bonds and carbon chains.

Zhang *et al.* [32] also performed atomic-scale computational studies of SiCOH structures using the method of Tajima *et al.* [23, 33]. They altered the building blocks used to construct the SiCOH unit cell to include more experimentally observed motifs, *e.g.,* silicon-based motifs with less than three associated oxygen atoms, and -CH_2 bridging bonds. They also used different criteria to choose which of the resulting structures seemed most likely to match experiment, basing their decision on minimum energy configurations as opposed to Tajima's 'least distorted' configurations. Their use of a unit cell on the same scale as Tajima's study leads to the same difficulties in extending their work to comparisons with experimental-scale structures.

Knaup *et al.* [18, 27] also created small unit cell-based models of organosilicate glasses to study the effect of structural composition on the resulting mechanical properties of the film. Their calculations involved a thorough analysis of the elastic response of organosilicate glasses to hydrostatic and shear loading. Their focus seemed to be less concerned with mimicking experimental films, instead focusing on understanding the influence of various types of structural entities on the resulting film mechanical properties. Overall they found that an increase in the number of -CH_2 linking groups creates higher elastic moduli as compared to films with -CH_3 terminal groups. Their simulations did not, however, address the effects that these structural entities have on the dielectric constant, nor did they investigate the effects of porosity.

Oliver *et al.* [29] conducted a study modeling the behavior of *spin-on* type SiCOH dielectric materials. They developed a Stillinger-Weber-like three-body interatomic potential and

used it to link together Si-CH_2-CH_2-Si groups and Si-CH_2-CH_2-Si-CH_3 groups through oxygen bonds. This method does not reflect the properties of the CVD-type films of interest in this study; however, there were several points in their treatment and study of these films that are relevant. First, their decision to treat Si-CH_x-type bonding units as unique entities interacting with oxygen atoms, instead of attempting to model all the bonding connectivity of the system explicitly, is computationally more efficient. It is also more flexible in that the different components have more freedom to relax from their initial configurations when the bonding is not explicitly defined. The second point which differentiated Oliver *et al.*'s study from other computational explorations of SiCOH materials was their investigation of "fracture paths" within the material. This study confirmed that the fracture energy of a Si-CH_2-CH_2-Si-CH_3-based film is lower than that of an Si-CH_2-CH_2-Si-based film, as might be expected. The study points out that, although pendant -CH_3 groups significantly weaken the mechanical integrity of the film, these groups provide other beneficial properties needed in low-k materials and hence should not be entirely eliminated. Oliver *et al.* verified their structures with NMR data and calculated the bulk modulus which was in agreement with the properties of experimental films. They did not investigate the effects of porosity or calculate the dielectric constant of their films.

The Yuan *et al.* [25-26] group produced significant simulation studies of SiCOH materials. Their work outlined a structure-generation method based on a well-defined underlying Si-O framework, with CH_3-groups included at random intervals and of a pre-determined quantity and distribution. Yuan *et al.* assumed only a very limited number of structural elements that interconnect to create the SiCOH structure. For example, Si-CH_2-Si bridging units were not included. They did, however, manage to bridge the random nature of the amorphous film with the known elements of its composition in a well-balanced manner. Their method is also more

adaptable to the inclusion of additional structural possibilities, which makes it attractive as a general-use algorithm. Yuan *et al.* used an energy minimization scheme to relax the structures from a regular 3D mesh framework to one with more reasonable bond angles and lengths. Importantly, however, this approach does not allow for significant structural rearrangements to occur as the entire framework is pre-defined. The results of the study indicate that the algorithm is successful in creating materials with values for Young's moduli that match experiment. The dielectric constant was not calculated nor was porosity addressed.

Prior calculation of porosity both in simulation and experiment

Existing simulation studies have largely overlooked the influence of porosity on the resultant properties of SiCOH materials. Studying the porosity of these materials is important because, while introducing pores lowers the dielectric constant of SiCOH, porosity creates significant integration challenges ranging from weak mechanical properties to copper diffusion into the SiCOH. [4] While many studies focus on the macroscale material properties, such as density, Young's modulus, and dielectric constant, it is also necessary to study the porosity of these materials as an important contributor to the low dielectric constant and poor mechanical properties.

Several studies have calculated the porosity of computer-generated models of other amorphous materials, [34-37] and there are also experimental studies which have established general information about the porosity and pore size distribution of SiCOH materials. [17, 38-44] Most studies of computational porosity begin by defining a certain radius for each atom in the simulated structure. From there, methods are differentiated by the different ways in which they find the void spaces around these atoms. Some studies use a Monte Carlo method to search for

points within the structure which are a certain cut-off distance away from the nearest surrounding atoms. Others use a Monte Carlo method to simulate the insertion of atoms of a given substrate into the material, and then retain those that create a zero net potential energy interaction with the surrounding atoms. [34-35, 37] Another method involves applying a regular 3D mesh to the structure and counting the number of spaces in the mesh that do not overlap with the structure. [35] Many of the studies appropriately emphasize the distinction between *accessible* pore volume and *physical* pore volume; the former is the porous volume that can be penetrated by a chosen substance, and the latter is the total porous volume existing in the sample. It is generally of more interest for porosity calculations of simulated materials to calculate void spaces based on accessible pore volumes instead of simply calculating all the unoccupied space present in the system.

Experimental background on the porosity and pore structure of SiCOH materials is abundant. [17, 38-44] A large variety of experimental techniques have been employed in these studies, including small-angle neutron scattering [41], x-ray porosimetry [17], positron annihilation spectroscopy [38-40], scanning transmission electron tomography [44], small angle x-ray scattering [40], and ellipsometric porosimetry [40, 44]. A comparison across methods tends to show agreement with a conclusion that the majority of pores in a porous SiCOH film are about 1 nm in diameter. Experimental studies have also shown that it is possible for SiCOH films to have very different densities, dielectric constants, and porosities, depending on the procedure used to produce them; hence it is difficult to assign a specific porosity value to a particular SiCOH material. It is more appropriate to draw correlations between the density of the film and the porosity, which is one of the aims of this research. [15-16, 40, 45]

Prior Computational Calculation of Dielectric Constant in Amorphous Materials

The idea of using ~100-atom unit cells as the basis for DFT simulations of amorphous systems is quite common. A computational study of amorphous alumina, hafnia and hafnium aluminate by Momida *et al.* used cells of this size to establish trends between the composition of the different cells and their dielectric constants. [46] Vanderbilt *et al*. also used ~100-atom supercells in their study of amorphous ZrO_2 and HfO_2 to investigate how the crystallinity and coordination of different system elements affected the material's dielectric properties. [47] What distinguishes SiCOH systems from these other amorphous materials is the significantly larger number of possible structural elements which can be present in the SiCOH films, and the lack of uniformity with which they appear.

Clearly the calculation of the dielectric constant in SiCOH systems requires a different approach. A study by Courtot-Descharles *et al.* [48] used DFT to calculate the change in polarizability between Si-O, Si-C, and Si-H bonds. Based on these polarizability changes, they developed a correlation between the atomic composition and the polarizability of hydrogen silesquioxane (HSQ) and methyl silesquioxane (MSQ) materials and then used this correlation to estimate the polarizability of experimentally produced HSQ and MSQ films with known atomic composition (as established using Rutherford Back Scattering). The Clausius-Mossotti equation was then employed to compare their estimate with the experimentally calculated dielectric constant. The Clausius-Mossotti relation has been shown to be accurate for systems with low polarizabilities [49], as is the case in SiCOH systems. This relation links polarizability to dielectric constant, as described in (1)

$$\frac{k-1}{k+2} = \frac{1}{3\varepsilon_0}\sum_i \alpha_i N_i \qquad (1)$$

where k is the dielectric constant, ε_0 is the vacuum permittivity, α_i is the polarizability of species i, and N_i is the concentration of species i. [48] Using this relation, it is possible to estimate the dielectric constant of a system based on composition, volume, and polarizability.

The results showed relatively good agreement between the calculated and measured dielectric constants, in that the values did not differ by more than one. The reported error between the measured and calculated values, however, was on the order of 20% for at least one of the films, which is too high to be reliable in comparing different candidate ULK materials (*e.g.*, obscuring comparisons of a film with a k of 2.0 to one with a k of 2.4). The study was also not focused on chemical vapor-deposited (CVD) SiCOH materials which present much more structural variability and many more structural and compositional arrangements than simple HSQ and MSQ films.

To summarize the past work, DFT calculations of the polarizability, and hence dielectric constant, for small 100-atom cells could, in principle, be used to establish trends for SiCOH systems. However, a fundamental understanding how different structural units influence these trends will be necessary in order to apply these findings to larger-scale systems.

Remaining Challenges

While there has been extensive computational and experimental study of amorphous organosilicate glass materials, a complete understanding of the link between material structure, porosity, dielectric constant, and mechanical properties is still lacking. No single computational model of these materials has encompassed all of these properties simultaneously, leaving only partial understanding of their causal relationships. For example, to what extent does the composition of the material influence the resulting dielectric properties, and to what extent is k

controlled by the porosity? Does the increased porosity drive the weak mechanical properties, or are they a result of a weakened underlying system framework? Do the dielectric and mechanical properties change as a result of the same changes in composition and networking, or do different mechanisms cause these properties to change?

Once a model has been developed that completely encapsulates all of the properties of SiCOH materials, it could be used to understand how ultra-rapid thermal annealing affects the material properties. The hypothesis was that ultra-rapid thermal annealing might promote increased cross-linking within the material, improving the mechanical stability without sacrificing porosity as shown in Figure 3. Without a model that includes structure, porosity, dielectric and mechanical properties, this cannot be investigated. I can also glean insight into whether structure or porosity has the greatest influence on the dielectric constant or the bulk modulus.

In Chapter 2, I explain the initial set-up of a model of SiCOH materials and explain how it was designed to accurately portray the amorphous structure and randomly distributed pores within the material. The main theme is balancing well-established facts about the composition of SiCOH materials with its inherently random nature. I discuss initial materials set-up, relaxation using Replica Exchange Molecular Dynamics (REMD) techniques, inclusion of porous spaces, and pore size distribution analysis.

In Chapter 3, I estimate the dielectric and mechanical properties of the structural model. In order to study the dielectric properties, I use density functional theory (DFT) techniques, which are limited (in practice) to the number of atoms they can handle (relative to Molecular Dynamics simulations). To overcome this challenge, I describe the development of a correlation between atomic composition and overall system polarizability. I also use established

compression-based Molecular Dynamics techniques to calculate the mechanical properties of the system, and draw conclusions about the importance of the underlying material framework.

In Chapter 4, I explore the use of the REAX force field to study bonding changes in the SiCOH material during thermal annealing. The force field approach is almost unique in its ability to allow bond- breaking and forming to occur during simulations. This is a vitally important ability in a situation, like this one, where bond rearrangement is inherently part of the process. I compare these results favorably with complementary experimental studies, and show how the porosity, dielectric constant, and mechanical properties are affected by thermally induced changes in the material's structure.

In Chapter 5, I use the insights gained from the study of organosilicate glasses in order to help predict new classes of ULK materials. This work is focused on highly networked materials with intrinsic porosity which, on a molecular level, is often found in organic compounds with large ring structures. I study how these ring structures might influence the polarizability of the material, and how they might network together to form an effective low-k material.

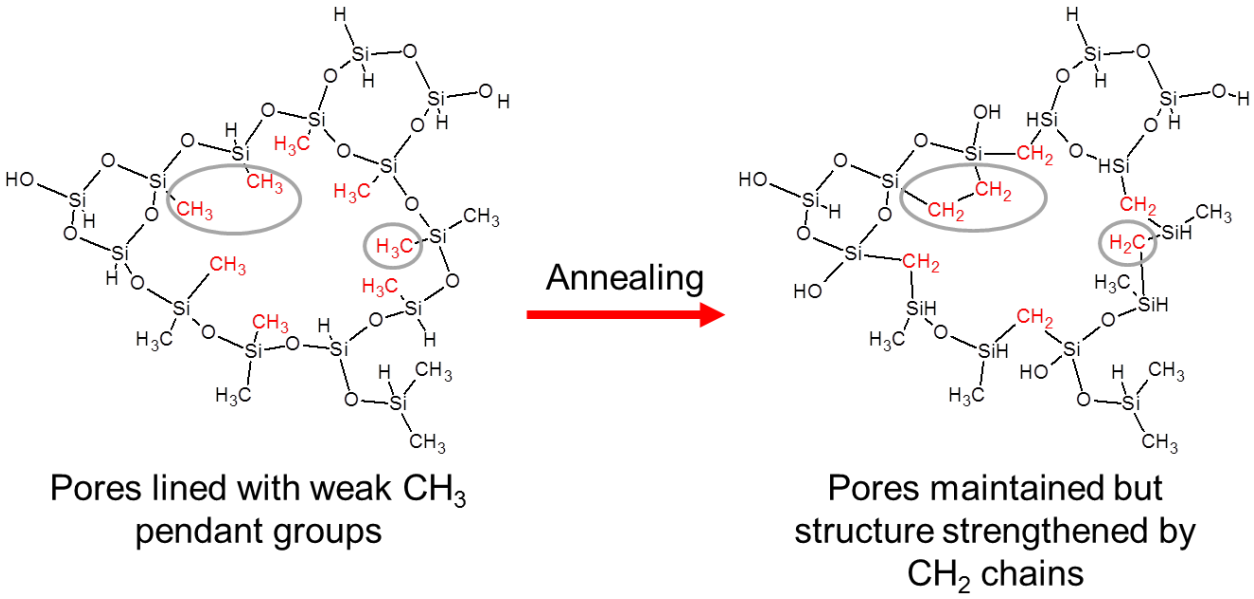

Figure 3. Hypothesized changes in SiCOH structure induced by rapid thermal annealing. It is predicted that the pores of the SiCOH material, which are initially lined with weak pendant methyl (CH_3) groups, would be induced to join the underlying system framework in the form of linking CH_2 bonds. This would promote increased mechanical stability without pore collapse and no change in the system dielectric constant.

CHAPTER 2

DEVELOPING A COMPUTATIONAL MODEL OF AMORPHOUS ORGANOSILICATE GLASS MATERIALS: MATERIAL STRUCTURE AND POROSITY SET-UP

In this chapter, I discuss development of an algorithm to generate a starting structure for an amorphous SiCOH material. A grid-based method to randomly distribute different structural motifs was used which maintained a desired overall composition. This grid-layout necessitates a rigorous relaxation procedure. I discuss using replica exchange (REMD) techniques to address this challenge. Porosity was introduced into the material by using excluded volumes during the system set-up. An algorithm was developed which calculated the porosity and pore size distribution of a given amorphous material.

Structure Generation

Structure Generation Algorithm

The CVD-film model for SiCOH used in this paper was based on a starting configuration similar to that described by Yuan *et al.* [25-26] I begin with a grid-based framework in order to lay out appropriate ratios of different system elements (as listed in Figure 4), while ensuring that their placement is randomly distributed throughout the film. The different ratios of structural motifs were based on the work of Grill *et al.* [40, 45] Modifications to the Yuan method were introduced in order to include porous spaces within the Si-O framework, with carbon chain-based structural elements of the type Si-$(CH_2)_x$-Si, and Si-H. The method was then further modified by allowing the oxygen atoms to move freely within the simulation box, instead of defining the oxygen as explicitly bonded to the silicon. [29]

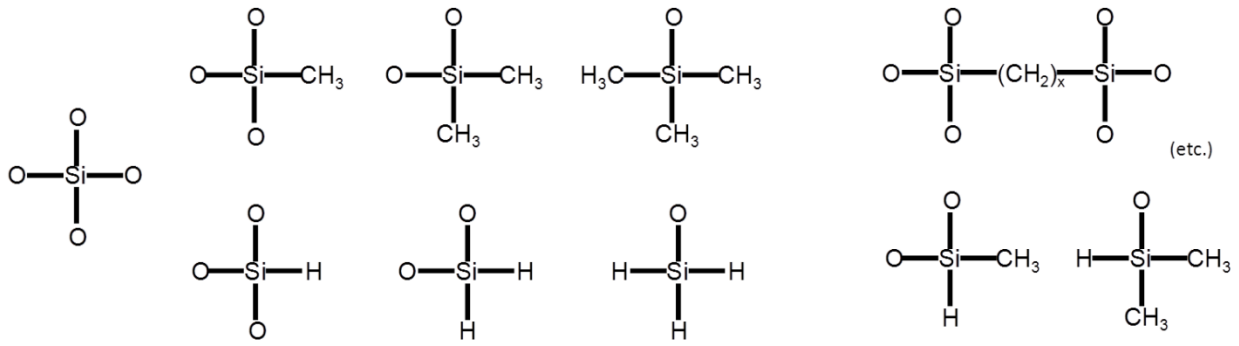

Figure 4. Catalog of different structural entities that can occur during experimental CVD processes using standard organosilane precursors. Assuming silicon always forms four bonds, any combination of silicon with oxygen, hydrogen, a terminal CH_3 group, or a linking CH_2 group is possible.

The film creation process begins by defining a regular simple cubic grid of (x, y, z) coordinates. This is the starting framework for identifying the locations of silicon atoms in the system. As silicon is four-coordinated in SiCOH films, the next step is to remove points on the grid such that as many points as possible have four nearest neighbor points, instead of six (up, down, front, back, right, or left). This is done using a series of simple steps, outlined in Figure 5. First, I choose a point on the grid; consider this to be point "A". Second, I count the number of neighboring points associated with point A. If there are too many neighboring points, I calculate the number of neighbors associated with each of these points (say, points B through G). If any of these points B through G has less than four neighbors, these are the first neighbors removed. If there are no points with less than four neighbors, or there are not enough points with less than four neighbors, points with six neighbors are randomly chosen to be removed, followed by points with five neighbors, followed by points with four neighbors. This method maximizes the number of points on the grid with four neighbors. There will be some small percentage of points on the grid with fewer than four neighbors; however, this will later be rectified by the introduction of carbon atoms and is a low enough percentage that it will not affect the algorithm's ability to maintain an appropriate atomic ratio.

The next step is to introduce porosity. The underlying framework will naturally have a very low porosity and so it is necessary to include porous spaces from the outset if an appropriate porosity and pore size distribution is to result. Porosity is included experimentally through the use of a porogen, which is an organic material introduced to break open the underlying silica framework that is then vaporized from the system leaving behind pores. To replicate this process, I calculate the approximate volume of the system, calculate the porous volume

Figure 5. Pictorial outline of the SiCOH structure-generation method. The method begins with a simple cubic grid, shown in (a). A point on this grid is chosen (shown in dark blue), and the number of nearest neighbors is counted (shown in light blue). The dark blue point in (a) has one too many neighbors, so (b) illustrates choosing one of the blue neighbors, now colored red, and counting the number of neighbors of the red point (shown in pink). The red point has six neighbors, so its removal is preferable for the overall system connectivity to meet its target of desired neighbors. Image (c) shows that the original dark blue point now has four neighbors, as desired. Image (d) shows how a piece of the grid might look when all points have four neighbors or less. Image (e) shows the introduction of a porous region, represented by the blue block. This region is treated as if it cannot be filled with atoms. Image (f) shows silicon atoms being introduced at the main points on the grid. Image (g) shows carbon and hydrogen atoms bonded to silicon atoms at appropriate points to complete the four-fold coordination of the silicon atoms. Image (h) shows the final incorporation of oxygen atoms between all neighboring silicon atoms, as well as any necessary creation of CH_2 network bonds.

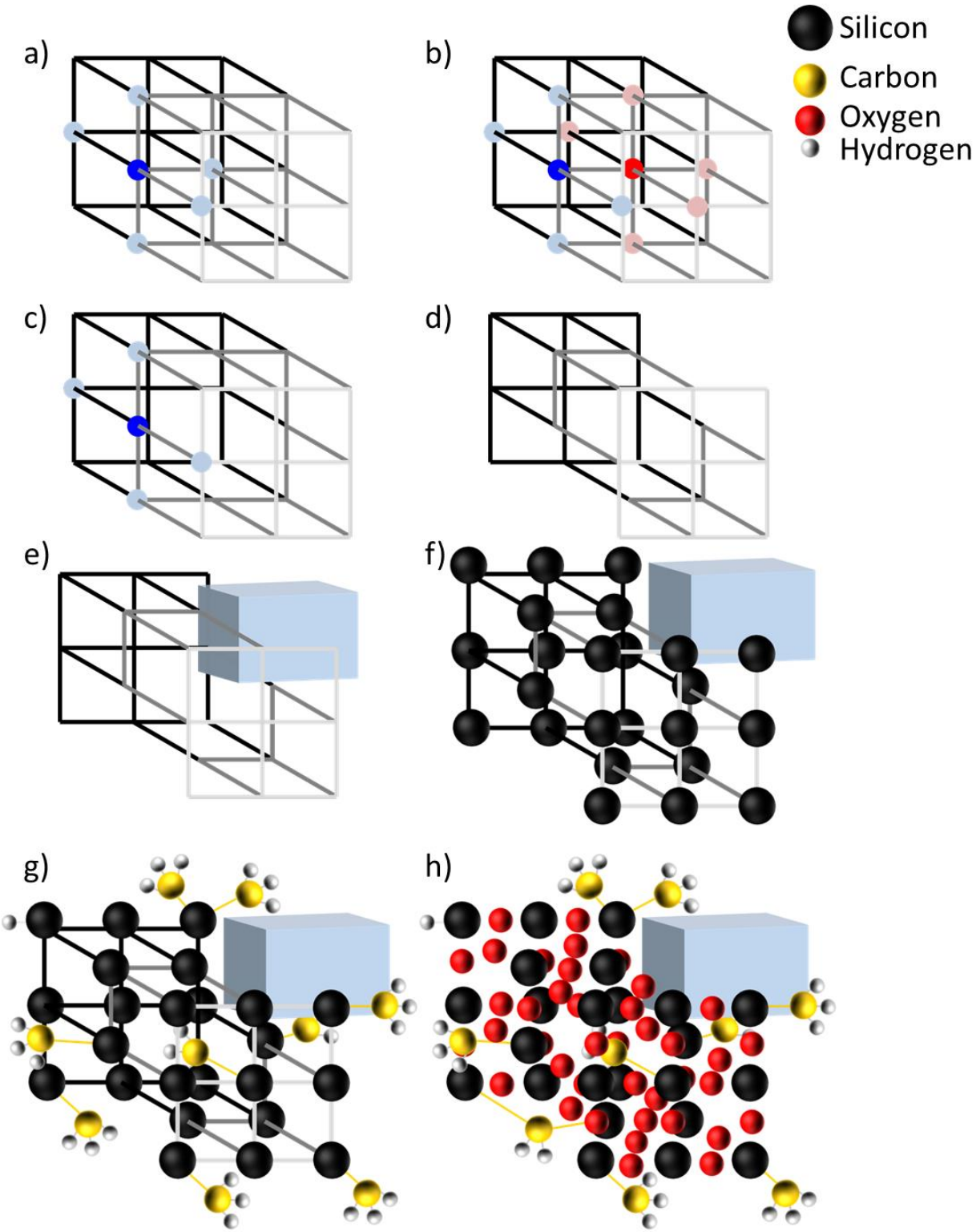
a)
b)
c)
d)
e)
f)
g)
h)
Silicon
Carbon
Oxygen
Hydrogen

needed to reach the desired system porosity, and then distribute small excluded volumes randomly throughout the system until this porous volume is reached. The excluded volumes are cubic sections of $8x10^{-30}m^3$. It might seem easier to randomly remove points on the grid to fulfill the needed porosity, but the resulting pore size distribution will be smaller than is experimentally observed as the porous spaces will be too isolated to form real pores.

After introducing porosity, I add carbon atoms to the system. First, I calculate how many $SiOR_4$, SiO_2R_2, SiO_3R, and SiO_4 groups (where R can represent $-CH_3$, $-CH_2$, or -H) are needed to match experimental structural distributions. [45] Second, silicon atoms with four neighbors are randomly chosen to fulfill the need for SiO_4 groups. These atoms, and their neighbors, are identified as atoms which cannot be removed in later portions of the simulations. Next I identify silicon atoms with only three neighbors to satisfy the requirements for SiO_3R groups. Once a silicon atom with three neighbors is located, a neighboring empty space on the grid is assigned as a carbon atom and the neighbors of the silicon atom in question are flagged so that they are not later removed. If there are not enough silicon atoms with three neighbors, silicon atoms with four neighbors are randomly chosen and their neighbors are removed using the same methodology used to reduce the number of neighbors on the grid from six to four in the first stage of the algorithm. This is repeated for SiO_2R_2 groups and $SiOR_4$ groups. There is often some discrepancy between the initially calculated need for $SiOR_4$, SiO_2R_2, SiO_3R, and SiO_4 groups and the resulting configuration resulting from the random elements of the algorithm, but the effects of this variation on the resulting ratio of structural units is negligible.

Once carbon atom locations and their associated connectivity have been identified, I determine how many $-CH_3$ groups, $-CH_2$ groups, and -H atoms are needed to satisfy experimentally relevant distributions. Hydrogen atoms are included by randomly choosing

carbon atoms and reassigning them as hydrogen until the required number of silicon-bonding hydrogen atoms is reached. The remaining carbon atoms then require an appropriate number of hydrogen atoms. The locations of hydrogen atoms for a given carbon atom are determined based on a tetrahedral arrangement, randomly rotated about the carbon.

The final step in the algorithm is to introduce oxygen atoms between any neighboring silicon atoms, and then resize the grid to reflect appropriate Si-O, Si-C, and Si-H bond lengths. C-H bond lengths are already incorporated in the previous step. A representation of these steps is shown in Figure 5. An example of the final full-scale result is shown in Figure 6.

Molecular Dynamics Force Field Set-Up

All of the Molecular Dynamics simulations were run using the LAMMPS software. [50] The potentials used to define the interatomic interactions of the ULK systems were chosen based on the work of Oliver *et al.* [29] The combination of bonded and non-bonded interactions employed by Oliver *et al.* [29] is an attractive choice because it allows the SiCOH system to reconfigure itself during minimization, independent of the framework introduced by the initial configuration.

The explicitly bonded interactions of the silicon-carbon fragments are described by the Optimized Potential for Liquid Simulations (OPLS). [51] This well-used potential contains expressions defining equilibrium bond length (eqn. 2), bond angle (eqn. 3), and dihedral backbone angle magnitudes (eqn. 4) of the Si-C system.

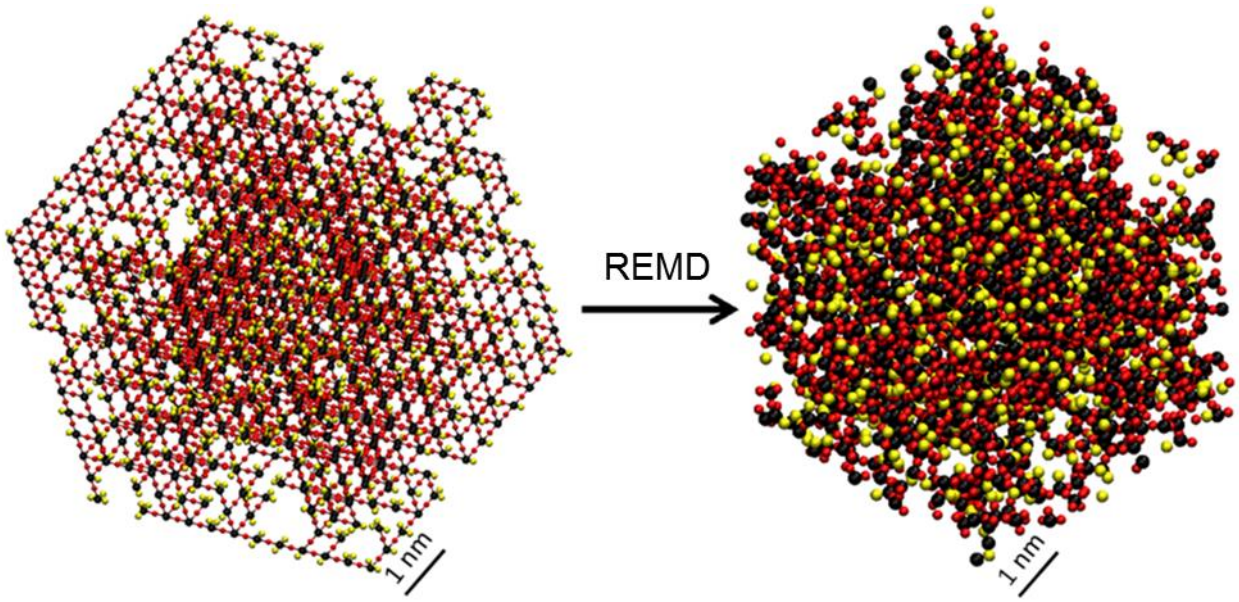

Figure 6. Representative starting structure shown on left. Silicon and carbon atoms are shown in black and yellow, respectively; oxygen atoms are shown in red. In order to incorporate all of the different structural possibilities associated with CVD structures, the system begins on an ordered grid-based layout. However, because the bond angles defined by this layout are unfavorable, the system quickly moves out of this grid structure once relaxed in REMD simulations, as shown on the right.

$$U(r) = k_r(r - r_0)^2 \qquad (2)$$

$$U(\theta) = k_\theta(\theta - \theta_0)^2 \qquad (3)$$

$$U(\phi) = \frac{1}{2}k_1(1 + \cos(\phi)) + \frac{1}{2}k_2(1 - \cos(2\phi)) + \frac{1}{2}k_3\big(1 + cost(3\phi)\big) + \frac{1}{2}k_4(1 - \cos(4\phi))$$

(4)

OPLS employs a united-atom approach with regards to the C-H bonded behavior, meaning that the parameters characterizing the carbon interactions use an effective potential corresponding to $-CH_2$ or $-CH_3$ groups, without explicitly defining the hydrogen contributions. The Si-H bonds of the CVD type model are the only instance in this study where hydrogen is individually modeled using this potential. Although the algorithm described earlier includes these C-H bonds, these bonds were not needed for this model and were not included. The parameterization used for this potential is listed in Tables 1-3. Units of energy in all cases are kcal/mol, as these are the units most commonly used in MD simulations. Units of distance in all cases are Å.

Table 1 OPLS Bond Parameterization

Bond	k_r	r_0
Si-C	187	1.86
C-C	208	1.529
Si-H	166	1.48

Table 2 OPLS Angle Parameterization

Angle	k_θ	θ_0
Si-C-C	60.0	112
C-Si-C	60.0	110
Si-C-Si	35.0	109.5
C-Si-H	35.0	110.5

Table 3 OPLS Dihedral Parameterization

Angle	K_1	K_2	K_3	K_4
Si-C-C-Si	5.2	-0.5	0	0
C-C-Si-C	0	0	0	0
Si-C-Si-C	0	0	0.1	0
C-C-Si-H	0	0	0.15	0
Si-C-Si-H	0	0	0.167	0

The non-bonded Si-O interactions are defined by the Stillinger-Weber potential, as modified by Watanabe *et al.* [52] The Stillinger-Weber potential includes two-body and three-body interaction terms (eqn. 5) and has been shown to be particularly accurate at describing the silicon-oxygen interactions of silica-type compounds [52]. It is thus particularly relevant in SiCOH materials which maintain a silica-like Si-O framework.

$$U(r,\theta) = \sum_i \sum_{j>i} \phi_2(r_{ij}) + \sum_i \sum_{j\neq i} \sum_{k>j} \phi_3(r_{ij}, r_{ik}, \theta_{ijk}) \qquad (5)$$

Here ϕ_2 represents the two-body term, which is a function of the distance r between an atom i and an atom j, and ϕ_3 represents the three-body term, which is a function of the distances r_{ij} and r_{jk} between atoms i, j, and k, and the angle θ_{ijk} formed by the positions of those three atoms. The parameterization for this potential for Si-O interactions, as derived by Watanabe *et al.*, is listed in the Table 4.

The Watanabe *et al.* [52] parameterization for this Stillinger-Weber model included a multiplicative function g(z) in the bonding equation. This function varied as a function of oxygen coordination number, z. The value of this function g(z) for an oxygen coordination of two is unity and so has no influence on the behavior of this system. All oxygen atoms in the system are two-fold coordinated throughout the simulation. This term will affect the process, however, in the discussion of thermal annealing in Chapter 2.

Table 4 Stillinger-Weber Parameterization of relevant three-body Si-O interactions

Set	ε	σ	a	λ	γ	$\cos(\theta_0)$	A	B	p	q	tol
Si Si Si	50	2.0951	1.8	16.404	1.0473	-0.333	7.05	0.602	4	0	0
O O O	50	2.0951	1.25	0	0	0	12.3	2.0	2.24	2.24	0
Si O O	50	2.0951	1.65	3.1892	0.310	-0.333	115.4	0.909	2.59	2.39	0
O Si Si	50	2.0951	1.4	2.9572	0.71773	-0.616	115.4	0.909	2.59	2.39	0
Si Si O	50	2.0951	1.9	10.667	1.94	-0.333	0	0	0	0	0
Si O Si	50	2.0951	1.4	10.667	0.25	-0.333	0	0	0	0	0
O O Si	0	1	1.0	1	1	1	1	1	1	1	0
O Si O	0	1	1.0	1	1	1	1	1	1	1	0

All remaining non-bonded interactions (C-O interactions and fragment-to-fragment Si-Si, Si-C, and C-C interactions) were modeled using the Lennard-Jones potential below.

$$U(r) = 4\varepsilon\left(\left(\frac{\sigma}{r}\right)^{12} - \left(\frac{\sigma}{r}\right)^{6}\right) \qquad (6)$$

The variables σ and ε are parameters unique to each atom-type pair combination (the collision diameter and maximum attractive energy, respectively, and r represents the distance between the two atoms).

Table 5 Lennard-Jones Parameters

Atom Pair	ε/k_B	σ
O-C	0.112	31.3
Si-C	0.181	33.7
C-C	0.102	33.5
O-H	0.102	28.6
Si-H	0.166	31.0
C-H	0.094	30.8
H-H	0.086	28.1

Replica Exchange Set-Up and Relaxation Procedure

A distinguishing feature of this computational ULK study, compared to past efforts [23-26, 31-32, 53], is the use of Replica Exchange Molecular Dynamics (REMD) as a structure-predicting technique. This method has the advantage of improved sampling and hence a greater likelihood of avoiding local (kinetically trapped) energy minima. [54-55] The REMD routine begins with the creation of a certain number of replica configurations (copies) of the system, each of which corresponds to a temperature within the chosen temperature set, in this case from 400 K to 200 K. These replicas are simulated in parallel with each copy on its own independent processor (using an IBM Blue Gene machine). Each replica performs a Molecular Dynamics (MD) simulation at its assigned temperature for a pre-defined number of iterations (typically 10), at which point replicas with neighboring temperatures within the set attempt to swap temperatures (T). This means, for example, that if the swap is accepted a replica running at 300K might swap with a replica running at 305K, and so the first replica will now run at the higher temperature, and the second replica will now run at the lower temperature.

Swaps are accepted with probability $\min\{1; \exp(\Delta\beta\Delta E)\}$ [54], where $\beta=1/k_BT$. At the lower temperatures, the system moves towards a more stable configuration that is closer to equilibrium by fine-tuning the atomic layout. At higher temperatures, there is enough kinetic energy to allow for larger structural changes in parts of the system which may have been unfavorably defined. The Metropolis-type step allows the system to break out of local minima at the lower temperatures, resulting in better sampling of the phase space and a well-equilibrated resultant system.

For this study, 64 replicas of a 5500-atom system were created, spanning a temperature range of 400 K to 2000 K. The low-end (400 K) is close enough to temperatures of interest for

the ULK system to be an effective minimum equilibration point. At the high end, 2000 K is high enough to allow the backbone Si-C-based molecules and oxygen atoms to move about with more freedom, without destroying the structural integrity of the backbone molecules. The distribution of temperatures is shown in Figure 7. This distribution was established to facilitate optimal swapping behaviors between neighboring replicas. [54-55] REMD results are shown in Figure 8.

In order to reach a relaxed structural configuration, the following procedure was adopted. First, the starting atomic layout and backbone bond definitions were defined, as previously described. The films were then thermally equilibrated at room temperature by ramping the simulation temperature from 10 K to 300 K over the course of 0.25 ns of simulation time, with a time step of 0.25 fs. The room-temperature system was replicated into 64 copies, and then spread evenly over 2048 IBM Blue Gene processors in preparation for the parallel tempering simulations. Each replica was equilibrated at its assigned parallel tempering starting temperature, ranging from 400 K to 2000 K, for 0.25 ns. Finally, the parallel tempering method was implemented on the 64 replicas. Each replica progressed through a constant temperature, constant volume (NVT) MD simulation, attempting a temperature swap every 500 time steps (0.125 picoseconds of simulation time). Simulations ran for a total of 10 ns of simulation time, requiring approximately 3 days (72 hours) of real (elapsed) run time.

REMD Behavior

The goal of the REMD parallel tempering method is to allow each replica to sample the full temperature range as many times as is needed for the system to reach a minimum energy state. Since each replica in the system was able to transition from the lowest temperature state to the highest temperature state and back again several times, I can be confident that a uniform state has been reached (Figure 9).

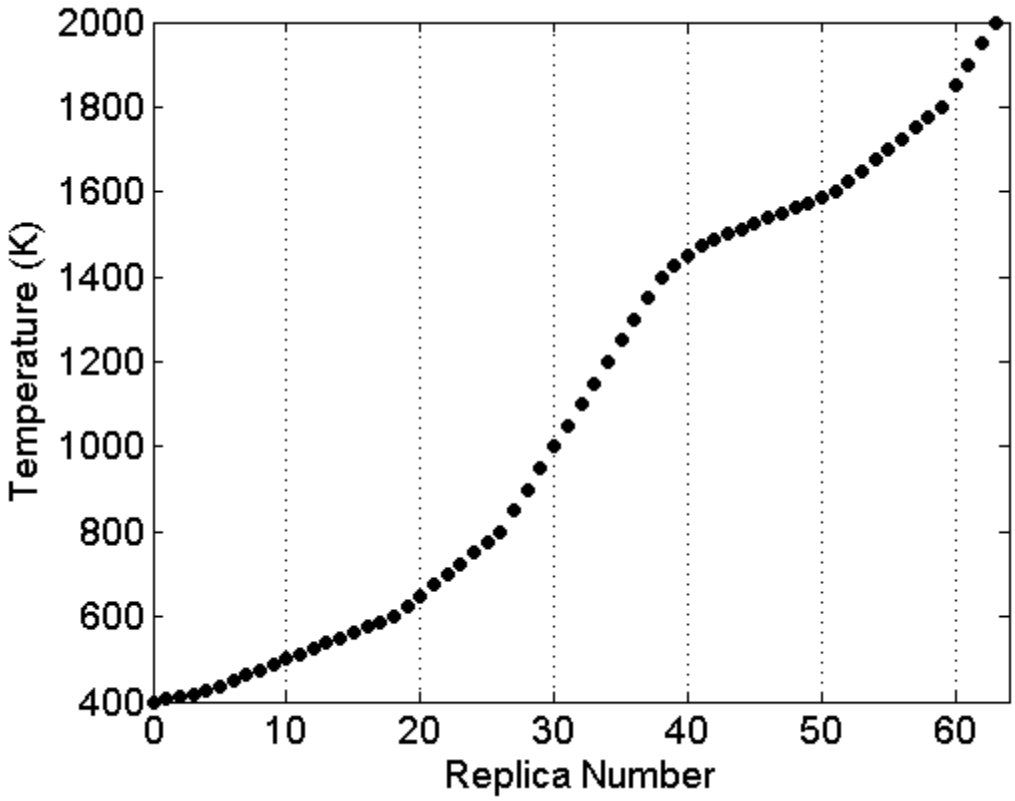

Figure 7. Temperature distribution across the 64 replicas, arranged in order of increasing temperature. The change in temperature is chosen to be smaller when there are large differences in the energy profile over a small temperature range. At other points, the energy profile is much broader and a larger spacing can be used.

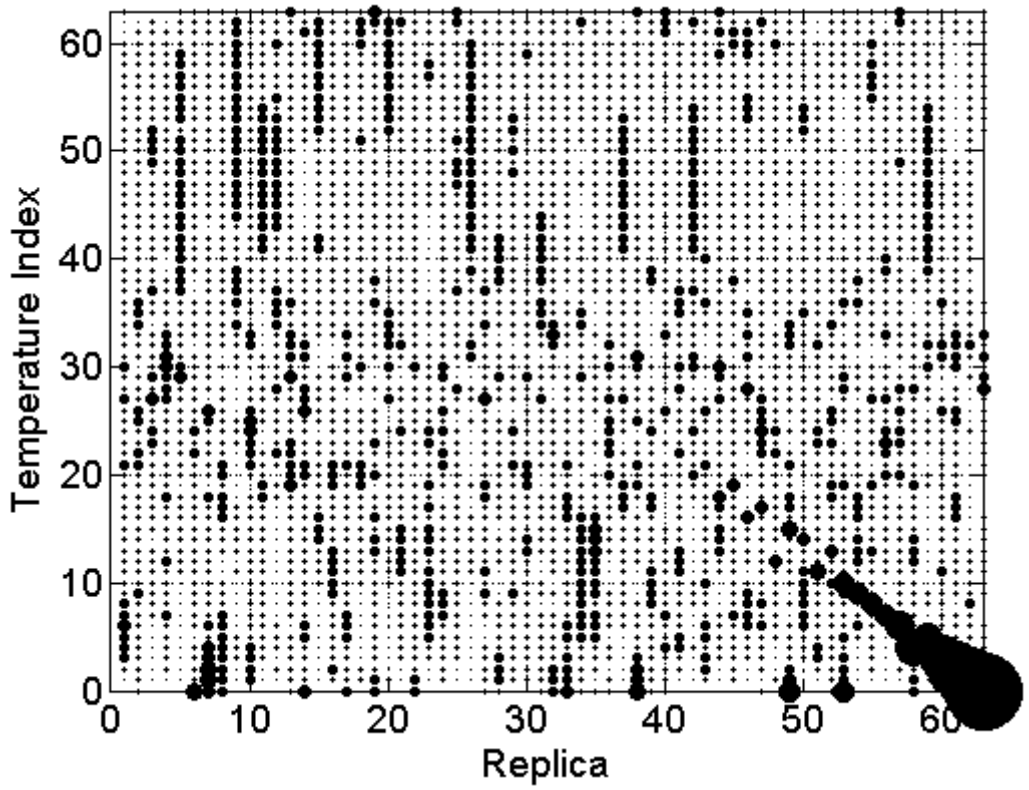

Figure 8. View of REMD data statistics that allows a qualitative visualization of the system behavior. The horizontal axis represents each of the 64 replicas shown in Figure 7. The vertical axis represents the index for each temperature in the set, from 400 K to 2000 K. The size of the dot at each point represents how much time a particular replica spent at a given temperature. So, for example, if point (2,5) were shown as a large dot, this would indicate that replica 2 spent a large amount of time at temperature '5'. Conversely if point (2,5) had a tiny dot, replica 2 did not spend very much time, if any, at temperature '5'. The plot shows that the system swapped and sampled successive temperatures relatively easily and evenly across the temperature range, and exposed temperatures at which replicas are most likely to get trapped – that is temperatures which are so far from the next highest or lowest temperature that the energy profiles do not overlap enough.

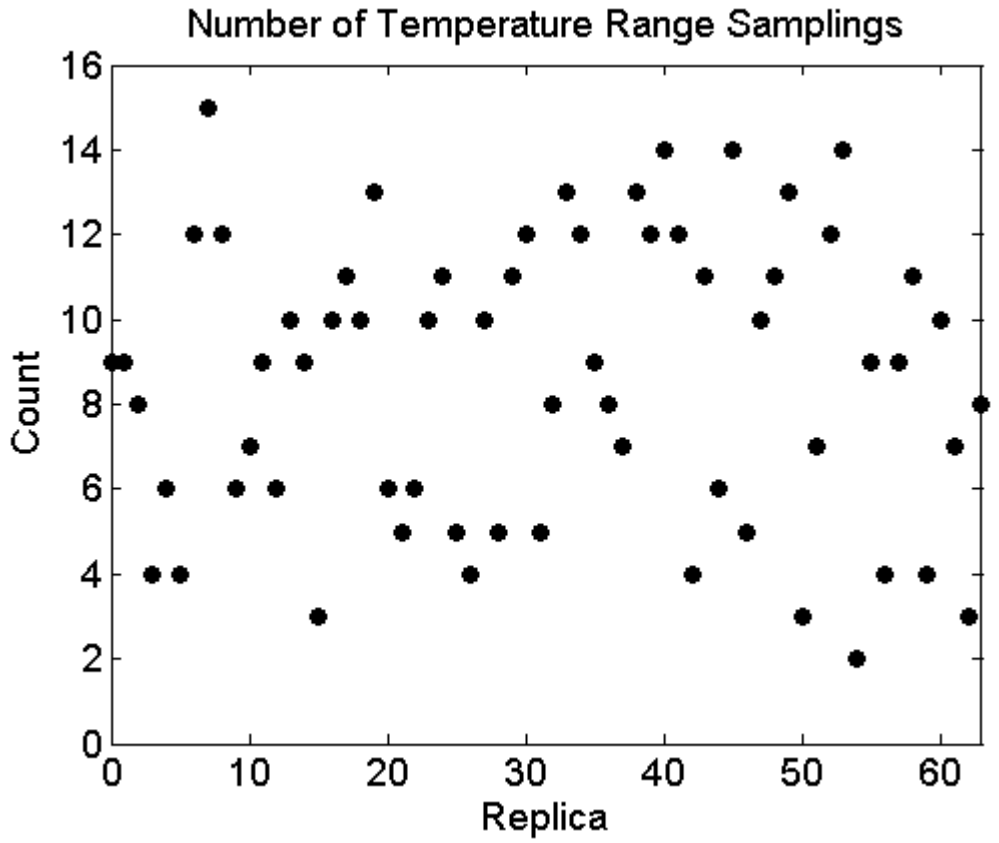

Figure 9. Number of times each replica sampled the full temperature range, either from 400 K to 2000 K or from 2000 K to 400 K. For this system, the temperature range was sampled approximately 500 times.

Another indication of efficient system behavior is manifested as even swapping rates between thermally adjacent replicas. As shown in Figure 10, the system experienced even acceptance rates for attempted swaps, in the 0.2 to 0.5 range, which is considered ideal. [55]

The REMD process more significantly affected the structure of the system, compared to the traditional MD equilibration used to thermalize the initial system. To understand the impact of the REMD approach, I have to revisit the way that bonding is represented in the system. As mentioned above, this study used the Stillinger-Weber potential to define the atomic interactions for the underlying silicon-oxygen framework. This potential is comprised of a two-body term and a three-body term, which strictly regulate the bond lengths and bond angles associated with Si-O interactions. The bonding of each silicon atom with each oxygen atom is not explicitly defined however and, as the system relaxes and rearranges itself, silicon and oxygen atoms are free to move in and out of the cut-off (3Å) used to determine whether or not an effective "bond" exists. This means that silicon-oxygen bonding is allowed to evolve throughout the simulation as thermal fluctuations push silicon and oxygen atoms in and out of the range of the potential model.

Figures 11 and 12 illustrate the extent of silicon-oxygen bonding (as well as Si-Si and O-O bonding) (Figure 11) and changes in the numbers of characteristic angles characteristic (Si-O-Si, O-Si-O, and Si-Si-O) (Figure 12) observed during REMD. These figures clearly show that silicon-oxygen bonding is able to vary throughout the simulation in response to the replica exchanges. This behavior is in contrast to a traditional MD approach (Figures 11 and 12) for which the same data show an initial rapid relaxation of the system in under 0.3 ns as the initial structure adopts appropriate bond lengths and angles, followed by stagnation throughout the rest of the equilibration.

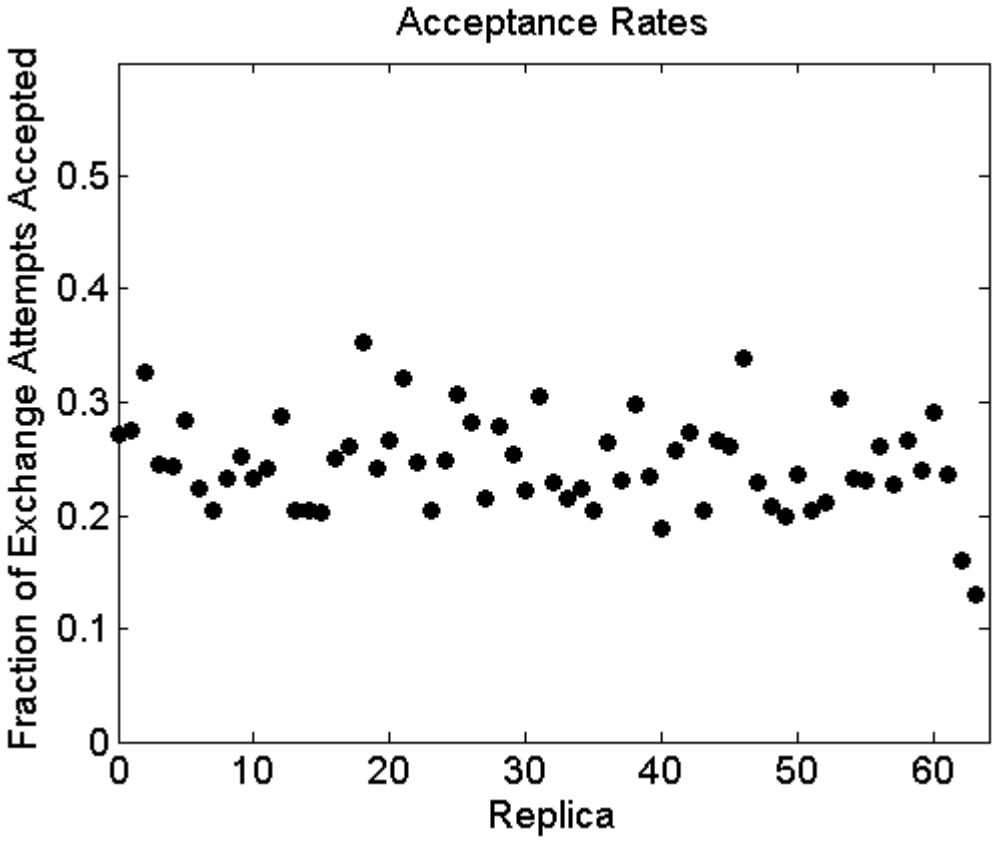

Figure 10. Acceptance rates for each replica in the system showing generally even distribution across all the replicas. The two replicas with slightly lower acceptance rates, 62 and 63, correspond to replicas that started at the highest temperatures. These replicas quickly swapped to lower temperatures and then took some time to equilibrate sufficiently to begin swapping again. Once this initial phase was completed, replicas experienced even swap rates across the board.

The number of Si-O bonds changes by an average of about 200 bonds per nanosecond, whereas during traditional MD annealing the number of bonds changes by only about 60 bonds per nanosecond. I can therefore conclude that the REMD is able to influence the behavior of the underlying silicon-oxygen framework in a way that is more representative of the true bonding in the system than traditional MD.

System Property Verification

Once an equilibrated structure for the amorphous ULK film had been established, the next goal was to verify that properties of the simulated material agree with experimental data. The radial distribution functions (RDF), are commonly used to quantify the structure of a system, as shown in Figure 13, revealing the equilibrium distances between pairs of interacting atoms. An RDF of Si and O, for example, shows that the most favorable spacing occurs between 1.5 and 2 Å (Figure 13a). The net (or overall) RDF in Figure 13b shows the most common atom spacing for all pairs of atoms in the system. By comparing the net RDF with the RDFs for individual atom pairs, it is possible to determine the most common structural elements in the system.

For all systems studied, the largest peak in the net RDF matches the spacing in the Si-O RDF, indicating that the Si-O framework dominates the material's structure, as expected. This is supported by the other RDFs in the system (Figures 13c-13d). The dominant equilibrium length of these three interactions are all significantly longer than that of the Si-O interaction, indicating that the oxygen atoms prefer to interact with the silicon atoms over any other type of atom in the system. The average bond lengths for the various motifs in the system were also tabulated (Table 6) to ensure that they are consistent throughout.

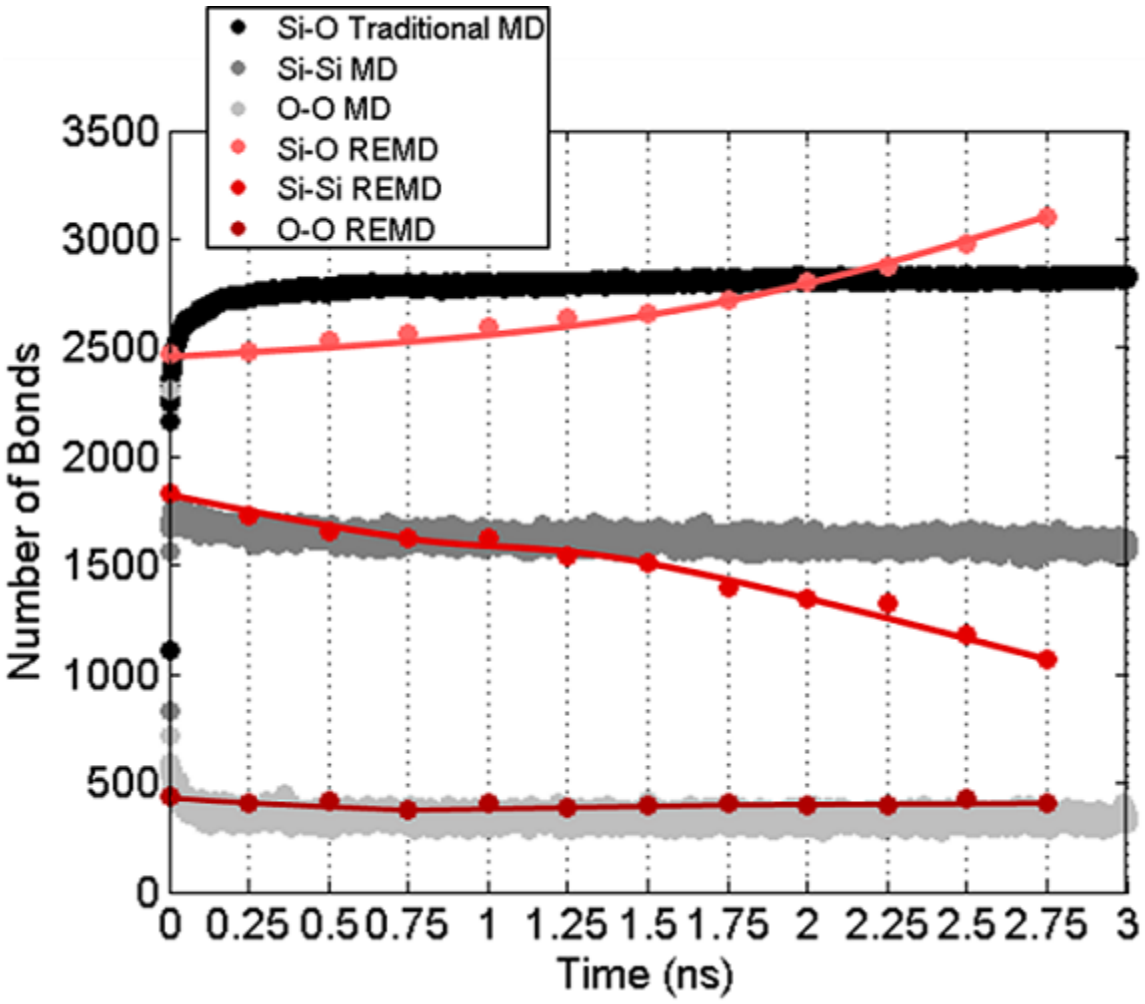

Figure 11. Number of Si-O "bonds" as determined by the Stillinger-Weber interactions as a function of time throughout the course of the REMD simulation and during the thermalization process using traditional MD. In traditional MD, the bonding initially changes rapidly as the as-generated structure relaxes, but then remains unchanged in its structure. The REMD data show the behavior of one replica as it proceeds through all temperatures associated with the REMD process, both high and low, twice. The silicon-oxygen (and Si-Si, *etc.*) bonding is able to vary throughout the simulation, showing the unique effect the REMD process has on the final structure of the system.

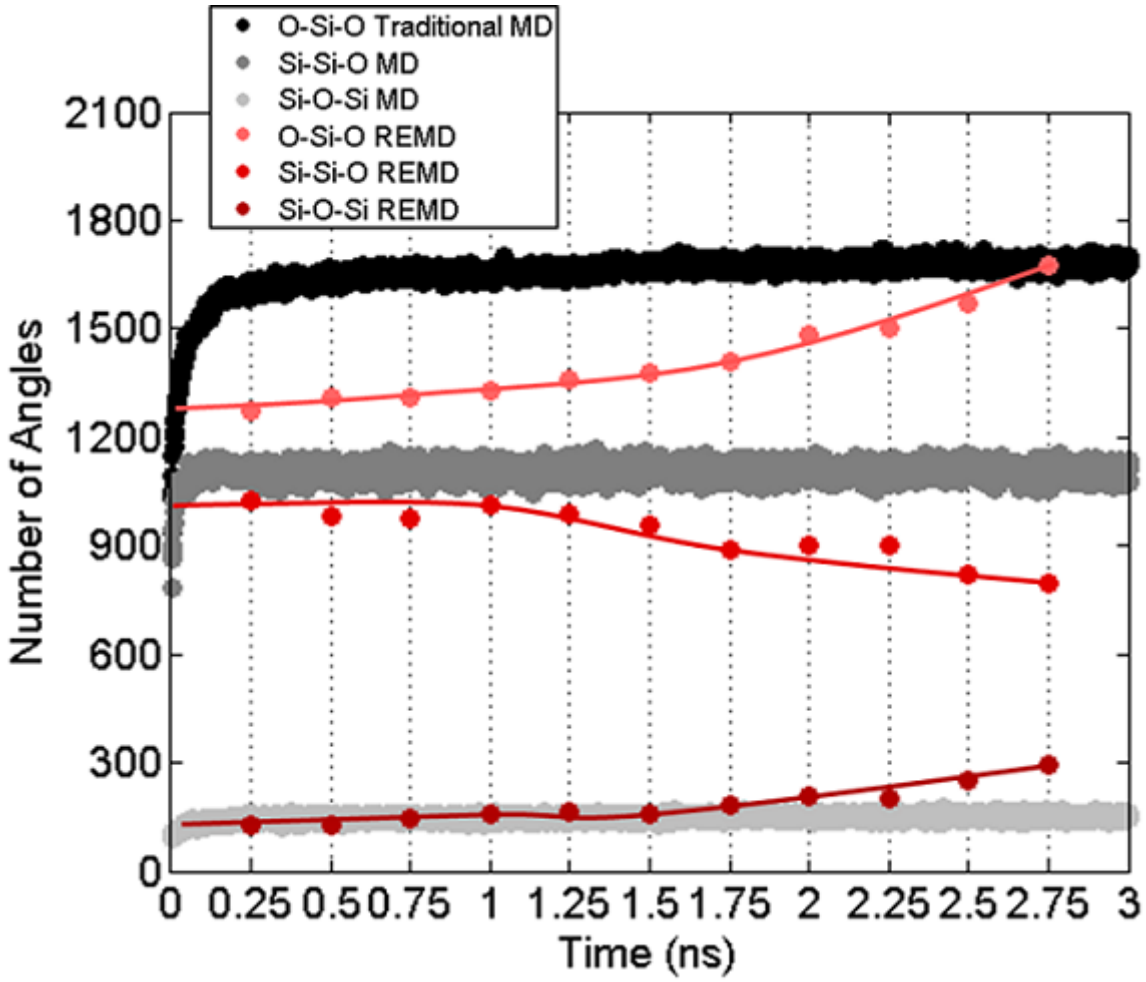

Figure 12. Numbers of different types of bonding angles as a function of time throughout the course of the REMD simulation and during the thermalization process using traditional MD. In traditional MD simulations, the number of angles of a given type initially changes rapidly as the as-generated structure relaxes, but is then unaffected by further equilibration. The REMD data show the behavior of one replica as it proceeds through all temperatures associated with the REMD process, both high and low, twice. The number of angles of any given type (*e.g.*, Si-O-Si) change continuously throughout the simulation.

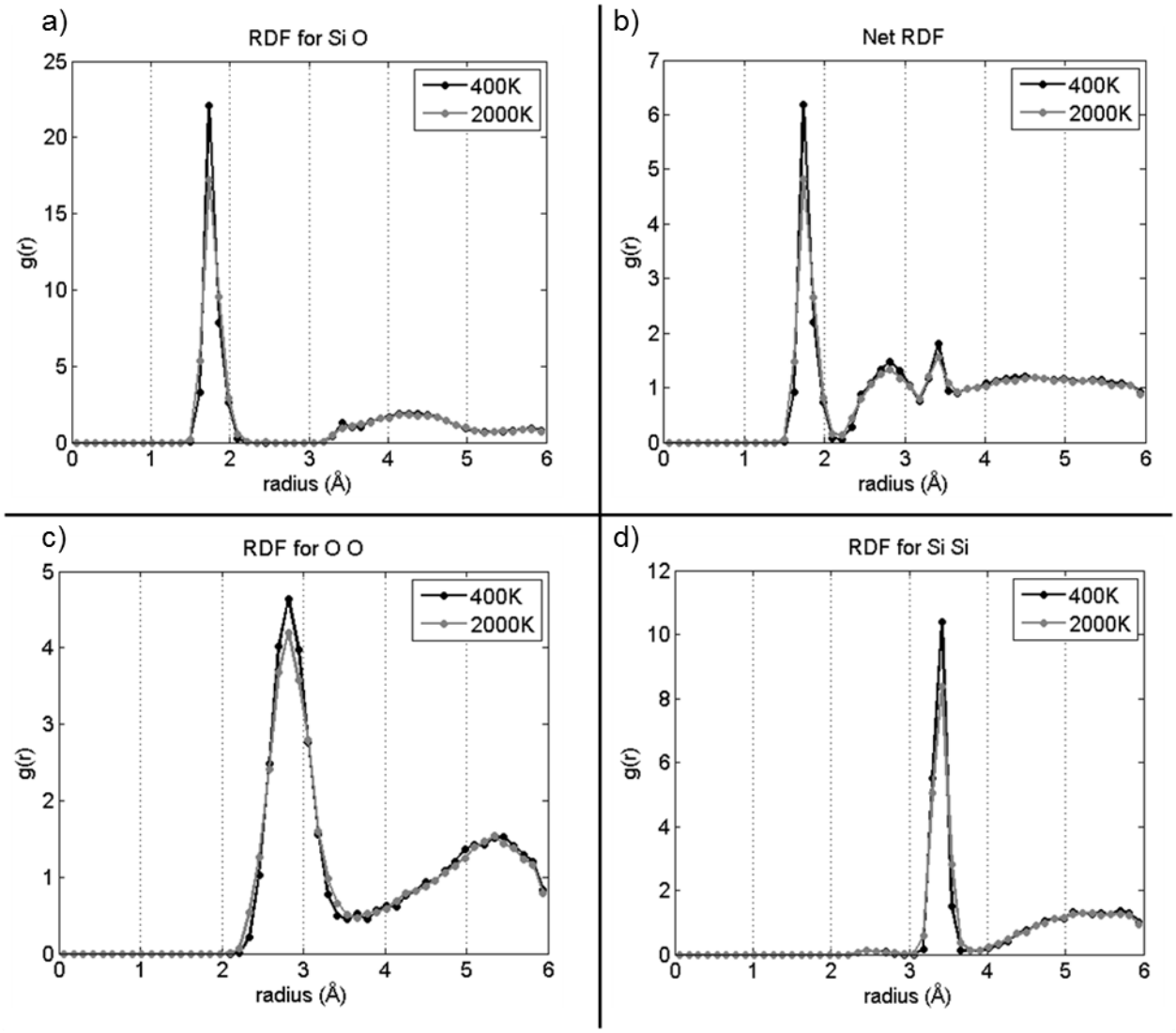

Figure 13. Representative radial distribution functions (RDF) for the SiCOH material studied, comparing structures at the extreme ends of the temperature range explored in the REMD simulations, 400 K (black) and 2000 K (gray). a) RDF for the dominant Si-O network. The equilibrium distance between Si and O atoms is around 1.7 Å. b) Net RDF; key as in (a). The most common spacing within the system occurs between 1.5 and 2 Å, which correlates with the Si-O peak. c) RDF for O-O interactions; key as in (a). The equilibrium distance between oxygen atoms of around 2.8 Å is larger than Si-O. d) RDF for Si-Si interactions; key as in (a). The largest peak at 3.3 Å corresponds to one of the smaller peaks in the "Net RDF." All these results reinforce the dominance of the Si-O network to determine the RDF.

Table 6 Bond lengths associated with the post-REMD, relaxed SiCOH system.

Bond Type	Bond Length (Å)	Standard Deviation (Å)
Si-C	1.94	0.05
Si-O	1.69	0.04
Si-H	1.57	0.04
C-C	1.53	0.03

The new method for developing simulated structures of SiCOH films has either overcome or improved upon a number of technical challenges associated with modeling these materials in the past. The biggest advancement this model offers over past efforts is the random distribution of structural motifs maintained throughout the system model. There is no reliance on a large unit cell-based approach, even in modeling systems on the order of 10,000 atoms in size, as used here. Most previous approaches to modeling SiCOH materials have been limited in terms of the scale of the base system, typically only on the order of 100- atom cells. [18, 23-24, 27, 32, 56]

Additionally, this model incorporates all of the structural motifs seen in experimental films as shown in Figure 4. Previous models of SiCOH films have been limited to Si-O-Si-$(CH_3)_x$ motifs [18, 23-24, 27, 32, 56] or Si-(CH_x)-Si-based motifs [29], but have never mixed both. Si-H bonds have also been unrepresented. The inclusion of a variety of different structural motifs creates a better approximation of a CVD-generated experimental film where more varied structures are likely.

The use of REMD allows for further relaxation and exploration of different system configurations than is accessible in traditional MD, allowing the system to achieve more appropriate bond lengths and angles. Furthermore, the use of a non-explicit bonding scheme, such as the Stillinger-Weber force field, to define the underlying Si-O framework allows for more relaxation than a more traditional bonding definition.

Porosity

Porosity and Pore Size Distribution Calculation

In order to ensure that the simulated films had porosities and pore size distributions on the same scale as experiment, I developed a method for calculating these properties. The only required data is the (x, y, z) coordinates of atoms in the simulation. While the idea is simple, scan through all of the xyz coordinates present in the system and identify porous spaces, there are many details that must be addressed.

First, it is necessary to establish a scanning probe size, essentially defining an underlying system grid. This was achieved by decreasing the size of the scanning probe until the resulting calculated porosity ceased to vary. I searched using a probe that was 0.5 Å in diameter. Choosing an origin I calculate the distances to the (x, y, z) coordinates of all of the atoms in the system. These distances are sorted, and it is then determined whether the closest atoms are near enough to overlap with the scanning probe point in question, or whether the scan point is a porous space.

In order to be considered a porous space, the distance between the probe point and the center of a neighboring atom needs to be greater than the sum of the radius of the atom associated with that distance (shown in Table 7), the radius of the probe (0.25 Å), and 1Å. The radius of the atom in question and the radius of the probe are needed to ensure that there is no overlap between any atoms and the area being searched. The 1Å requirement is added to ensure that the point is far enough away from any neighboring atoms that another atom could reasonably "added" at that point. If this is not included, the calculated porosity will not reflect a meaningful value, it will quantify the porous space present in the system but it will not represent space that can be occupied by another atom or molecule, *i.e.*, the experimentally accessible porosity.

Table 7: Atomic radii [57] of each atom-type in the system used to calculate porosity.

Atom	Radius (Å)
Si	1.17
C	0.77
O	0.66
H	0.31

If the point searched is determined to be a porous space, the coordinates are stored and the next point that does not overlap with the space searched is tested say, (0.5, 0, 0). If that space is occupied by an atom, the next space searched is, say, (0.25, 0, 0). This "back tracking" is included to define the extent of the pore more finely.

Once all of the porous spaces have been identified, they are then grouped into contiguous areas that constitute pores. Since it is known (given the size of the probe) that porous spaces belonging to the same pore must be 0.5Å apart, they can be grouped into different pores based on this information. The porous spaces making up the inside of the pore can then be considered cubic spaces rather than spherical, because there is no concern that atoms are overlapping with the cubic corners. After all the porous spaces have been separated into pores and their respective volumes have been identified, any pores with a volume less than 500 $Å^3$ are discarded, as experimental techniques are not currently capable of identifying pores below this size. The remaining pores are used to find the porosity and pore size distribution.

To verify the accuracy of the calculation, I created a test structure that I knew contained no pores. I then introduced pores of a known size and quantity, and used this method to calculate the porosity and compared these results to known values of the porosity. The results of these method verification tests are summarized in Table 8. The method predicted porous volumes within 10% of known values in all cases, which is sufficient for accurate pore characterization.

Table 8: Comparison of values of the porous volume between known amounts introduced into the test structure and that calculated by scanning through the system.

Introduced Porous Volume ($Å^3$)	Calculated Porous Volume ($Å^3$)	Error
64	62	-3%
85	89	5%
202	179	-11%
256	246	-4%
287	300	5%

Results and Discussion

The porosity and pore size distribution were calculated for the SiCOH systems studied. The goal was to mimic a film with a dielectric constant of 2.4, a density of 1.6 g/cm^3, a porosity of about 20%, an elastic modulus of about 4.2 GPa, and an average pore diameter between 1 and 1.5 nm. [40, 45] The simulated film showed a density of 1.12 g/cm^3, a porosity of 20.2%, an average pore diameter of 1.3 nm, an elastic modulus of roughly 4 GPa and an estimated dielectric constant of 2.2. The pore size distribution is shown in Figure 14, with all of the relevant film properties summarized in Table 9.

Table 9: Comparison of Experimental and Simulated CVD Films

	Density (g/cm^3)	Porosity	Average Pore Diameter (nm)	Modulus (GPa)	Dielectric Constant, k
Experimental CVD-deposited SiCOH Film [5-6]	1.06	20%	<1.5	4.2	2.4
Simulated SiCOH Film	1.12	20%	1.3	4.0	2.2

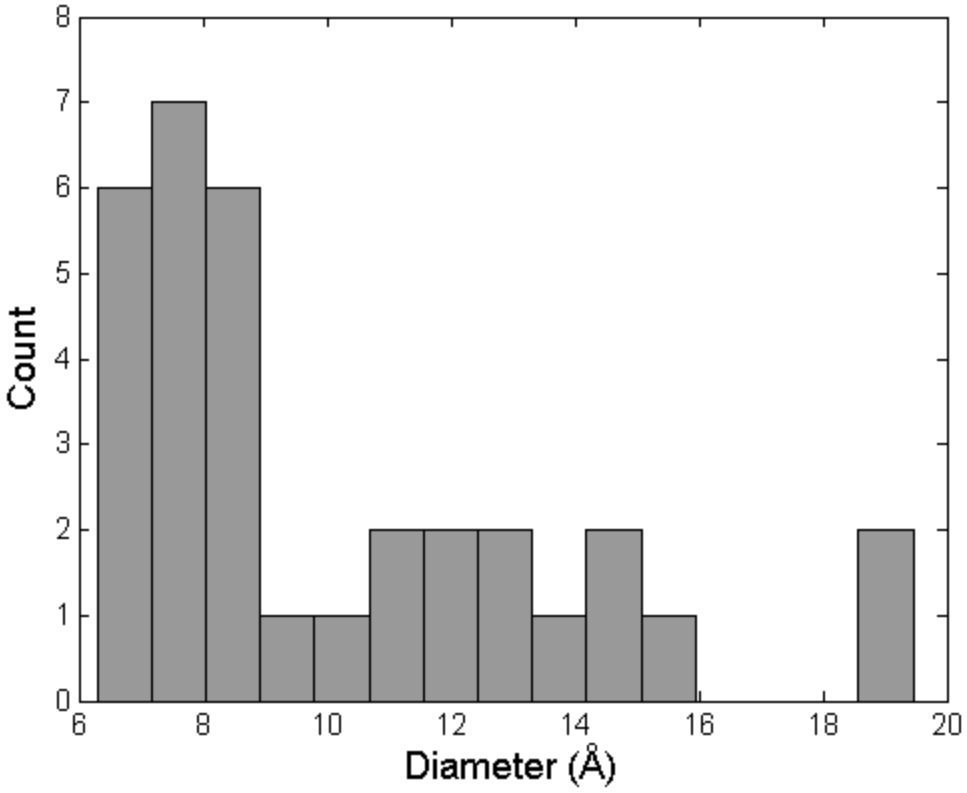

Figure 14. Pore size distribution for the modeled film, showing an average pore diameter of 1 nm. Diameters were estimated by assuming spherical pores and based on individual pore volumes.

This model is the first to systematically incorporate pores of a size comparable to experiment (on the order of 1 nm diameter). This is critical in accurately estimating the mechanical and dielectric properties of the film as pores play a significant role in altering the film's structural integrity. The pores in this system are also shown to be stable at this size post-relaxation, which further suggests that the model is correctly mimicking experimental films.

I have also developed a method for calculating the porosity of an amorphous film, which can be readily implemented on any amorphous modeled system containing pores. This method contrasts Monte Carlo-based [34-37] or grid-based [58] methods in its simplicity, while providing high accuracy.

Conclusions

This chapter details the development of a unique method to balance the amorphous nature of the SiCOH material with known information about its structural make-up. I also showed the challenges and successes associated with using REMD to relax the resulting structural layout. Finally, I incorporated and calculated porosity and pore size distribution within the films.

CHAPTER 3

DEVELOPING A COMPUTATIONAL MODEL OF AMORPHOUS ORGANOSILICATE GLASS MATERIALS: DIELECTRIC AND MECHANICAL PROPERTY ANALYSIS

After establishing the structural layout and porosity of the SiCOH material, the next major task involves calculating the dielectric constant and mechanical properties. Both of these properties are determined as a result of the generated structure and porosity, and represent the "effects" caused by the model set-up. Calculating the dielectric constant of an amorphous material was a challenge. It was necessary to develop a correlation between the system atomic composition and the resulting system polarizability in order to overcome the size-limitations inherent in DFT techniques (100-200 atoms). I show how this correlation predicts sufficiently accurate dielectric estimates, both in the simulated materials and in an experimental study. I used standard compression-based Molecular Dynamics techniques to characterize the stress-strain relationship within these materials and generate estimates of their bulk and Young's Moduli. I show how strongly the networking within the material influences these mechanical properties.

Dielectric Constant

The Clausius-Mossotti equation was then employed to compare dielectric properties. The Clausius-Mossotti relation has been shown to be accurate for systems with low polarizabilities [49], as is the case in SiCOH systems. This relation links polarizability to dielectric constant, as described in (1).

$$\frac{k-1}{k+2} = \frac{1}{3\varepsilon_0}\sum_i \alpha_i N_i \qquad (1)$$

where *k* is the dielectric constant, ε_0 is the vacuum permittivity, α_i is the polarizability of species *i*, and N_i is the concentration of species *i*. [48]

Computational Methods and Approach

Estimates of model system polarizabilities were made using DFT techniques within the Gaussian 09 software. [59] Geometry optimization and frequency calculations were used in tandem to determine the polarizabilities of input structures. Gaussian calculates polarizabilities from static frequencies, which are calculated from the second derivative of the energies with respect to position. [59] Once the polarizabilities were known, the Clausius-Mossotti equation was used to calculate the dielectric constant. While polarizability is a tensor quantity, the non-diagonal *xy, xz, yz* components in all the cases examined were effectively zero, and the *xx, yy, zz,* diagonal components were within 10% of one another. The diagonal components were averaged to obtain a single polarizability value for a given structure.

On order to compare the effects of the choice of functional on the calculated polarizabilities eight different functionals and methods available in Gaussian 09 were used to determine the polarizabilities of six different SiCOH structures. The hybrid functionals tested were B3LYP [60], B3P86 [60] [61], BMK [62], HSE06 [63-65], M06 [66], X3LYP [67], PBE0 [68-69], as well as the Moller-Plesset correlation energy correction, MP2 [70]. *A priori*, it was unknown whether the terms used in the different functionals would significantly influence the results for this class of materials. Variations in the polarizability between different functionals were, in fact, found to be very small and the average standard deviation across the different functionals for a given structure was ±1%. B3LYP was used for all further calculations as it was one of the least computationally expensive methods. The 6-31G(d) basis set [71] was used for all

simulations. To check the variation of results with other basis sets, I also performed calculations with the 6-311G [72] and LanL2MB [73] basis sets for four different motifs of varied sizes and compositions. The results for all three different basis sets were within 10% of one another, and trends were consistent regardless of basis set used. The 6-311G predicted slightly higher polarizabilities and the LanL2MB basis set predicted slightly lower polarizabilities. The 6-31G(d) basis set was used as it provided essentially average or typical results; the polarizability trends were otherwise unaffected.

Small 100-atom sample SiCOH structures were created based on a scaled-down version of the structure generation method. These 100-atom structures have bonding connectivity, but only provide crude guesses for the angular relationships between the different atoms. To prepare these structures for DFT calculations, they are first were relaxed using Molecular Dynamics (MD) energy minimization techniques using the MM3 force field [74] in the software program TINKER. [75]

The MM3 force field combines bond stretching (E_s), angle bending (E_θ), torsional (E_ω), stretch-bend ($E_{s\theta}$), van der Waals interactions (E_{vdw}), and electrostatic terms. Possible bonds include Si-O, Si-C, Si-H, C-C, and C-H. The bonding information for all of the atoms in the system is predetermined in the MD studies, limiting the resultant configuration to the accuracy of the starting system. The key terms of the MM3 force field are as follows:

$$E_S=71.95k_s(l-l_0)^2[1-2.55(l-l_0)+\left(\frac{7}{12}\right)2.55(l-l_0)^2] \quad (2)$$

$$E_\theta=0.021914k_\theta(\theta-\theta_0)^2[1-0.014(\theta-\theta_0)+(5.6)10^{-5}(\theta-\theta_0)^2-(7.0)10^{-7}(\theta-\theta_0)^3+9.0(10^{-10})(\theta-\theta_0)^4] \quad (3)$$

$$E_\omega=\left(\frac{V_1}{2}\right)(1+\cos\omega)+\left(\frac{V_2}{2}\right)(1-\cos2\omega)+\left(\frac{V_3}{2}\right)(1+\cos3\omega) \quad (4)$$

$$E_{s\theta}=2.51118K_{s\theta}\left[(l-l_0)+(l'-l'_0)\right](\theta-\theta_0) \quad (5)$$

$$E_{vdw}=\epsilon\left[-2.25\left(\frac{r_v}{r}\right)^6+1.84(10^5)\exp\left[-12.00\left(\frac{r}{r_v}\right)\right]\right] \quad (6)$$

The geometry was then re-optimized using the optimization routine used in Gaussian, which is based on the Berny algorithm. [76] Smaller strategically designed silicon-based motifs were set up using the software program *Avogadro* [77] and then geometrically optimized within Gaussian [59].

Calculations and Results

The ultimate goal of this study was to use DFT to develop a correlation between polarizability and atomic composition for SiCOH structures accurate enough to scale to larger simulations and experimental films. An appropriately sized SiCOH model structure, which mimics experimental film properties like porosity and mechanical integrity, would far exceed the number of atoms that can readily be managed by DFT methods (10,000 atoms, say, compared to 100). In order to overcome this difficulty, I created representative 100-atom SiCOH structures, with different compositions, and calculated their polarizabilities. I initially hypothesized that there would be a trend between the relative compositions of the structures and the polarizability. However, no such trend was apparent as shown in Figure 15. Increasing the number of representative 100-atom samples as a route to correlations among these structures also proved to be unsuccessful.

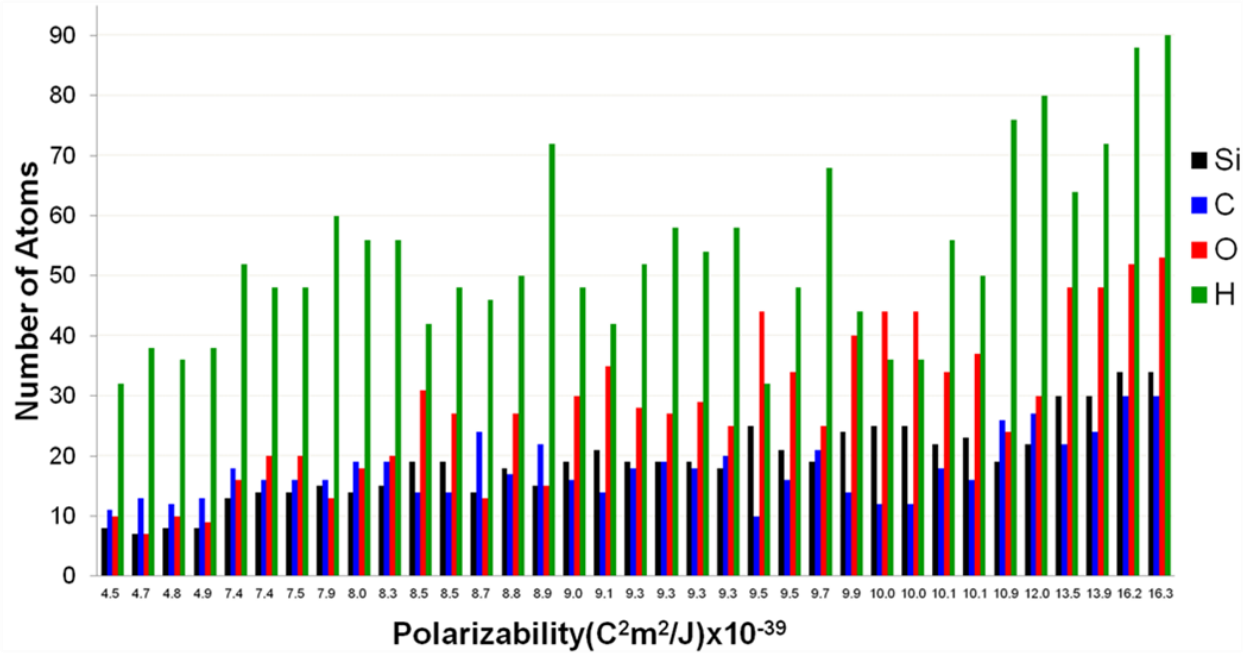

Figure 15. Overall polarizability for 35 different 100-atom structures as a function of their differing atomic compositions.

Table 10. Estimate of the polarizability using the correlation given in Table 11 compared to the value calculated using DFT for the same 35 initial 100-atom SiCOH structures shown in Figure 15.

Polarizability Predicted by Correlation (C^2m^2/J)	**DFT Calculated Polarizability (C^2m^2/J)**	**Difference (C^2m^2/J)**	**Error**
4.7E-39	4.5E-39	2.0E-40	4%
4.5E-39	4.7E-39	-1.5E-40	-3%
4.8E-39	4.8E-39	2.6E-41	1%
5.0E-39	4.9E-39	2.3E-41	0%
7.7E-39	7.4E-39	3.5E-40	5%
7.8E-39	7.4E-39	3.9E-40	5%
7.8E-39	7.5E-39	3.7E-40	5%
8.1E-39	7.9E-39	1.3E-40	2%
8.2E-39	8.0E-39	2.7E-40	3%
8.7E-39	8.3E-39	3.9E-40	5%
9.6E-39	8.5E-39	1.1E-39	12%
9.7E-39	8.5E-39	1.2E-39	14%
9.5E-39	8.7E-39	7.1E-40	8%
9.7E-39	8.8E-39	8.2E-40	9%
8.8E-39	8.9E-39	-5.3E-41	-1%
9.9E-39	9.0E-39	9.2E-40	10%
1.0E-38	9.1E-39	1.3E-39	14%
1.0E-38	9.3E-39	1.0E-39	11%
1.0E-38	9.3E-39	1.1E-39	11%
1.0E-38	9.3E-39	8.4E-40	9%
1.0E-38	9.3E-39	7.8E-40	8%
1.1E-38	9.5E-39	1.9E-39	20%
1.1E-38	9.5E-39	1.1E-39	12%
1.1E-38	9.7E-39	7.9E-40	8%
1.2E-38	9.9E-39	1.7E-39	17%
1.2E-38	1.0E-38	1.7E-39	17%
1.2E-38	1.0E-38	1.6E-39	16%
1.1E-38	1.0E-38	1.3E-39	12%
1.2E-38	1.0E-38	1.4E-39	14%
1.1E-38	1.1E-38	3.6E-40	3%
1.3E-38	1.2E-38	5.8E-40	5%
1.5E-38	1.3E-38	1.8E-39	14%
1.5E-38	1.4E-38	1.5E-39	11%
1.8E-38	1.6E-38	1.8E-39	11%
1.8E-38	1.6E-38	1.6E-39	10%

In consequence, to isolate the factors that influence system polarizability, I investigated small silicon-oxygen based motifs (*i.e.,* intrinsic, iconic, structural environments) and then systematically studied the changes in polarizability that result from changing atomic composition. As carbon-based motifs represent a new addition to the traditional silicon-oxygen based network in silica, the influence of carbon content on polarizability was the first variable isolated for investigation.

First I created small chains and rings of varying numbers of silicon atoms, in which all the atoms were connected to one another *via* oxygen atoms, and then calculated the polarizabilities of each of these miniature units. I started with the smallest configuration possible (three silicon atoms), and then increased the cluster size by small additions of one or two Si atoms. When the number of silicon atoms was increased by two atoms instead of one, it was merely to decrease computational effort. The trends were consistent enough that there was no need to test every possible configuration. I assumed that silicon atoms are four-coordinated and oxygen atoms are two-coordinated. The purpose of studying both rings and chains was to compare Si-O-H configurations against Si-O-Si configurations.

I then replaced each oxygen atom, one by one, with a carbon atom and calculated the new polarizability of the miniature structure with each successive carbon addition until the entire structure was connected *via* carbon atoms instead of oxygen atoms. This method established a strong linear trend between the polarizability and the number of carbon atoms present in the structure. Figure 16 shows the different base structural units tested, while Figure 17 shows the resulting linear trend between polarizability and carbon content.

Although there is clearly a linear trend between system polarizability and the number of carbon atoms present in the system, the contribution per carbon atom appears to be increasing

slightly as the systems become larger. As a result of the way in which the systems were set up (see Figure 16), the system becomes more interconnected with Si-O-Si type bonds and fewer Si-O-H type bonds as the number of silicon atoms increases. This translates to fewer CH_3 groups being added and more CH_2 groups being added. Based on this observation, the data were sorted into the contribution to the polarizability per carbon group for CH_3 groups versus CH_2 groups. The results are shown in Figure 17.

Figure 18 compares the change in polarizability of the Si-based motif systems with each additional carbon-based group, and the magnitude of this change between each additional Si-CH_3-type bond and Si-CH_2-Si type bond. I determined that there is a difference of approximately $0.3x10^{-42}C^2m^2/J$ in polarizability between the addition of a CH_3 group and the addition of a CH_2 group. This difference clearly needs to be included in any correlation of the overall composition versus polarizability in order for the values to scale properly. Assigning the difference in polarizability to the hydrogen atoms allows differences between the Si-CH_3 and Si-CH_2-Si bonding structures to be taken into account. Si-H bonding was studied in the same way as the carbon groups, simply substituting hydrogen atoms for carbon atoms. The results are summarized in Figure 19.

The preceding results have established a predictably linear relationship defining the influence of carbon and hydrogen on the polarizability of the SiCOH system. The next task was to investigate the influence of silicon and oxygen on the base system polarizability. I analyzed the polarizabilities of the 13 starting Si-O systems shown in Figure 16 in terms of the number of oxygen and silicon atoms present. Unfortunately, this information did not reveal trends stable enough to apply to larger systems.

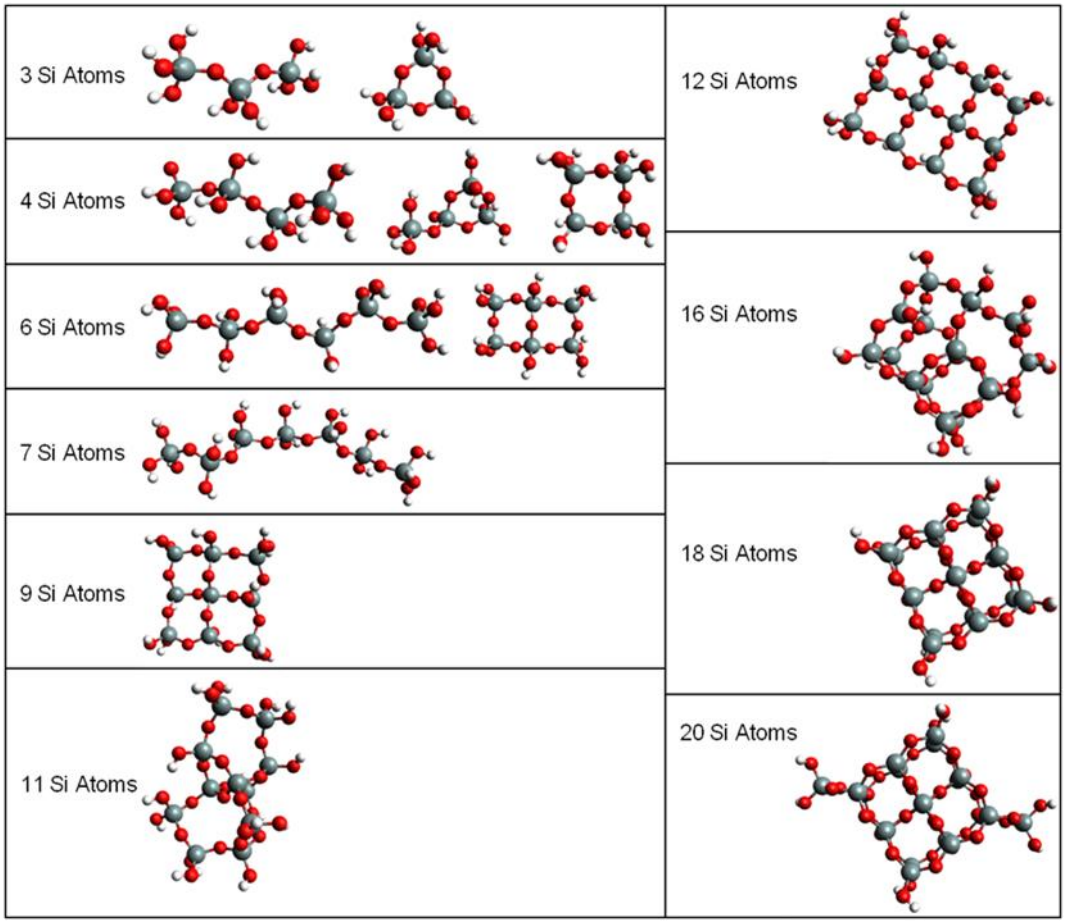

Figure 16. Different Si-based structural units tested. Red atoms represent oxygen, gray atoms represent silicon, and white atoms represent hydrogen. As two examples, these units can be represented as "chains," as in the 7-atom Si motif, or "rings," as in the 9-atom Si motif.

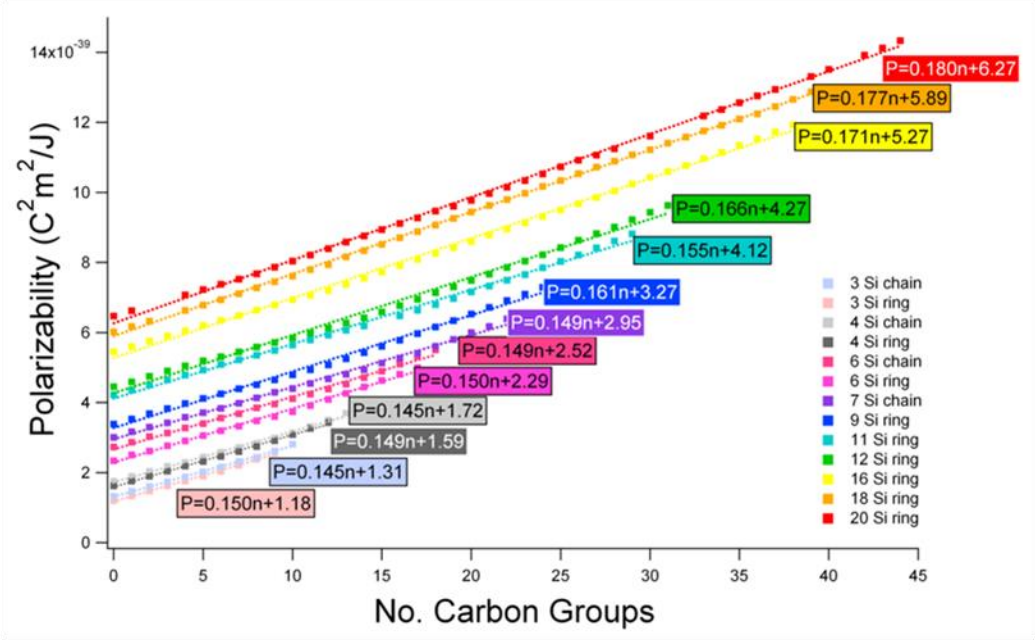

Figure 17. Polarizability of the different silicon-based motif structures (shown in Fig. 1) versus the number of carbon atoms present in the sample. There is a clear linear trend between the number of carbon atoms and the overall polarizability with approximately the same slope for each line, although the slope increases slightly with the number of silicon atoms.

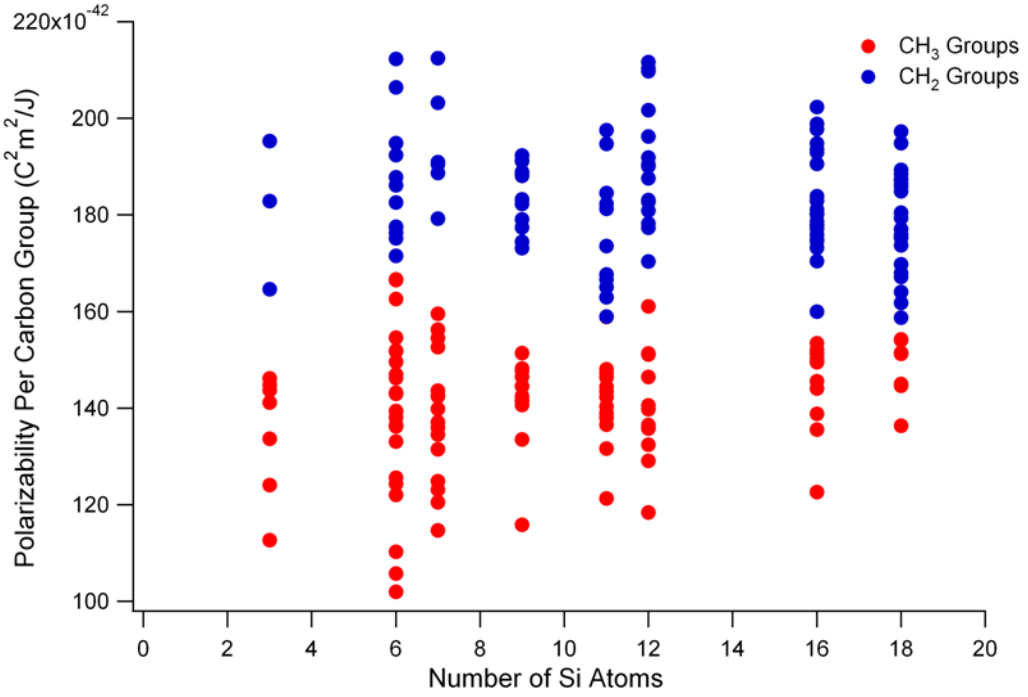

Figure 18. Data from Figure 17 organized in terms of the polarizability as a function of the number of the number of Si atoms in the motif and further delineated between CH_2 and CH_3 groups present.

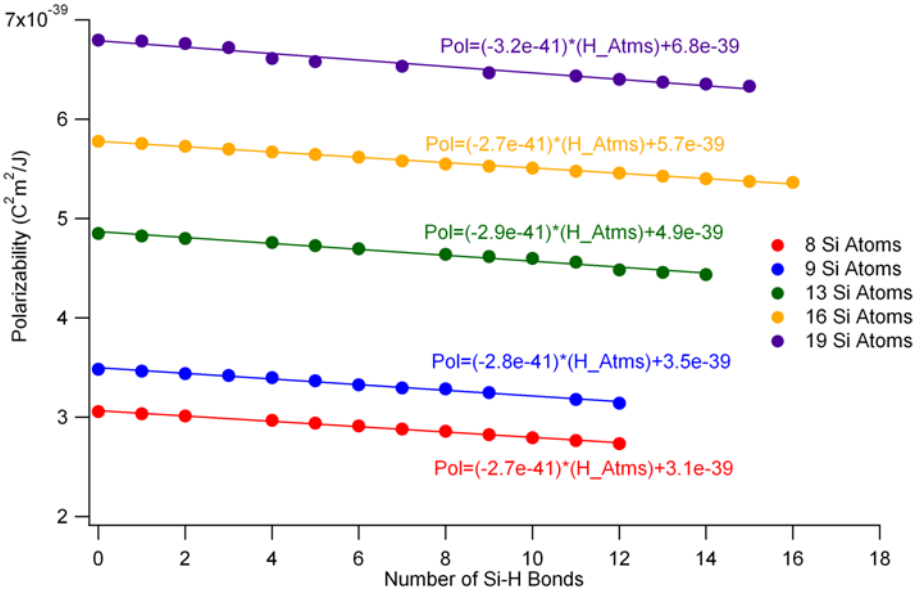

Figure 19. Change in polarizability of the system when Si-O-H bonds are replaced with Si-H bonds. Not surprisingly, the polarizability of a Si-H bond is found to be lower than that of a Si-O-H bond. There is generally little change in slope as the size of the Si motif increases from 8 to 19.

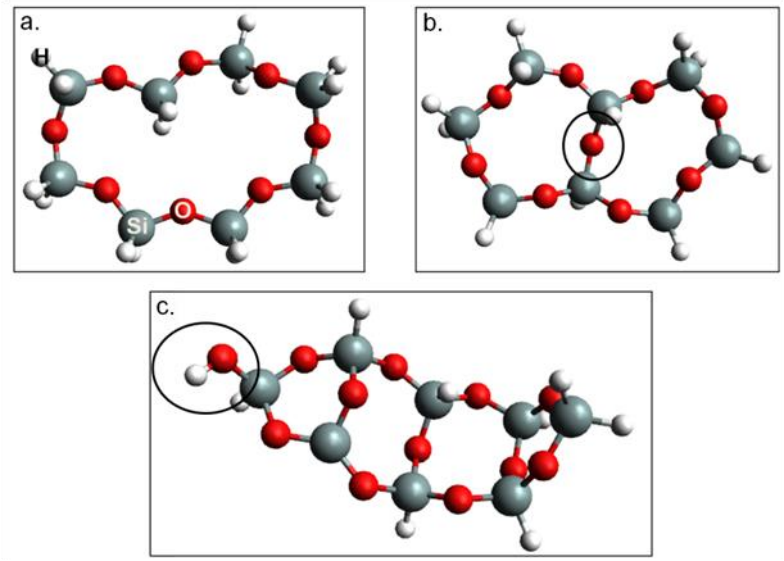

Figure 20. System (a) represents a ring-shaped starting motif for the initial Si-O polarizability study (b) shows the same system with an oxygen atom added to bridge across the ring (circled). System (c) represents the system after three such Si-O-Si "bridge" atoms have been added, and the addition of an O-H bond (circled).

In order to understand how Si and O atoms influence the polarizability, I developed a compendium of silicon-oxygen based structures and focused on the effect of changing the silicon:oxygen *ratio* on the polarizability. I began by creating small Si-atom motif systems containing 6-9 Si atoms, connected in ring-like configurations by oxygen atoms, and then successively added oxygen atoms to the systems calculating the system polarizability for each new structure. This process is outlined in Figure 20.

The results of this systematic change in the Si:O ratio are shown in Figure 21. This shows a marked difference between Si-O-Si modifications to the system compared to Si-O-H modifications. The number of O-H bonds in experimental SiCOH systems is typically very limited, so I focused on Si-O-Si contributions exclusively. To study the influence of Si-O-Si bonds on the polarizability, I used the same procedure outlined in Figure 20 but only added Si-O-Si bonds (no O-H bonds). I conducted this analysis on representative 6-, 8-, 9-, 12-, 16-, and 18-atom Si systems. The results showed a linear trend between the polarizability of the overall system and the ratio of Si:O in Si-O-Si bonded systems, as shown in Figure 22.

Establishment of a Correlation for Polarizability

Once these trends were established, I aggregated the information into a set of polarizability contributions for each type of atom in the SiCOH system. Constant-value contributions to the polarizability can be assigned for silicon, carbon, and hydrogen atoms. However, as discussed above, the contribution per oxygen atom is dependent on the Si:O ratio. As shown in Figure 17**,** the contribution per carbon atom is 2.5×10^{-40} C^2m^2/J, while the contribution per hydrogen atom is -0.25×10^{-40} C^2m^2/J, so that the contribution per CH_3 group is 1.75 C^2m^2/J and the contribution per CH_2 group is 2.0×10^{-40} C^2m^2/J. The contribution per silicon

atom was assumed to be $5.0x10^{-40}$ C^2m^2/J, based on a linear analysis of the base structures in Figure 16. The analysis described in Figure 22 suggests that the contribution per oxygen atom is $(-0.75(Si:O)+1.8)x10^{-40}$ C^2m^2/J. These values are also summarized in Table 11.

Table 11. Contribution to the polarizability as a function of atom type.

Atom Type	Contribution to Polarizability/Atom (C^2m^2/J)
Silicon	$4.7x10^{-40}$
Carbon	$2.5x10^{-40}$
Oxygen	$(-0.75(Si:O)+1.8)x10^{-40}$
Hydrogen	$-0.25x10^{-40}$

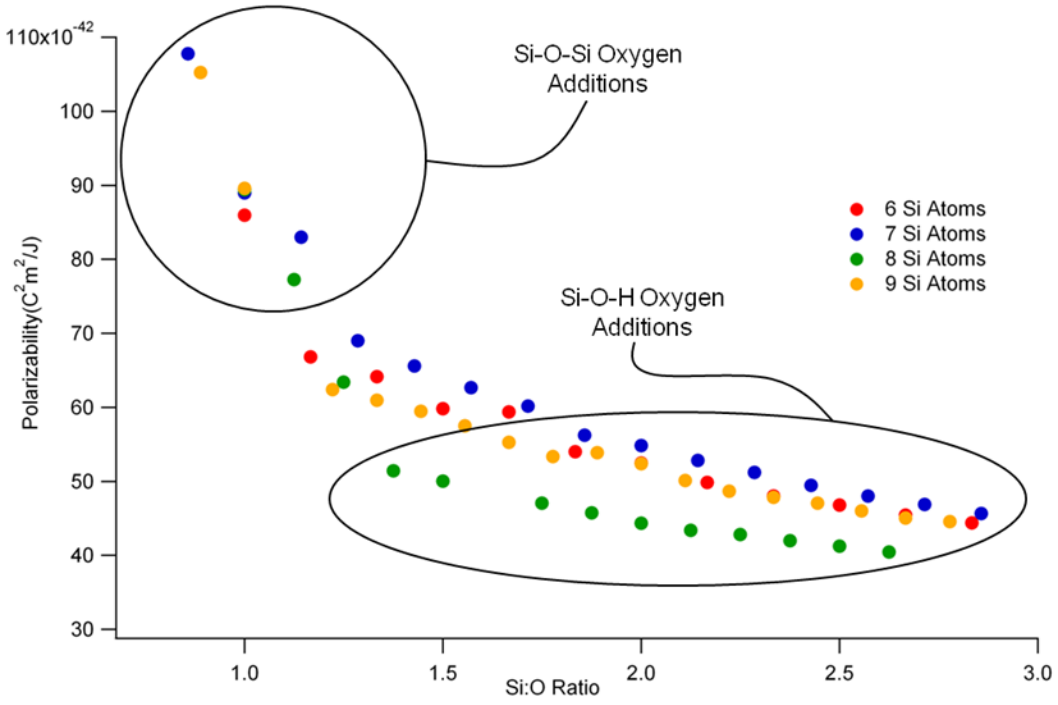

Figure 21. Polarizability change per oxygen atom added to the system versus Si:O ratio shows two linear trends: one corresponding to the addition of Si-O-Si type oxygen atoms and one corresponding to the addition of Si-O-H type oxygen atoms (regions are circled for clarity).

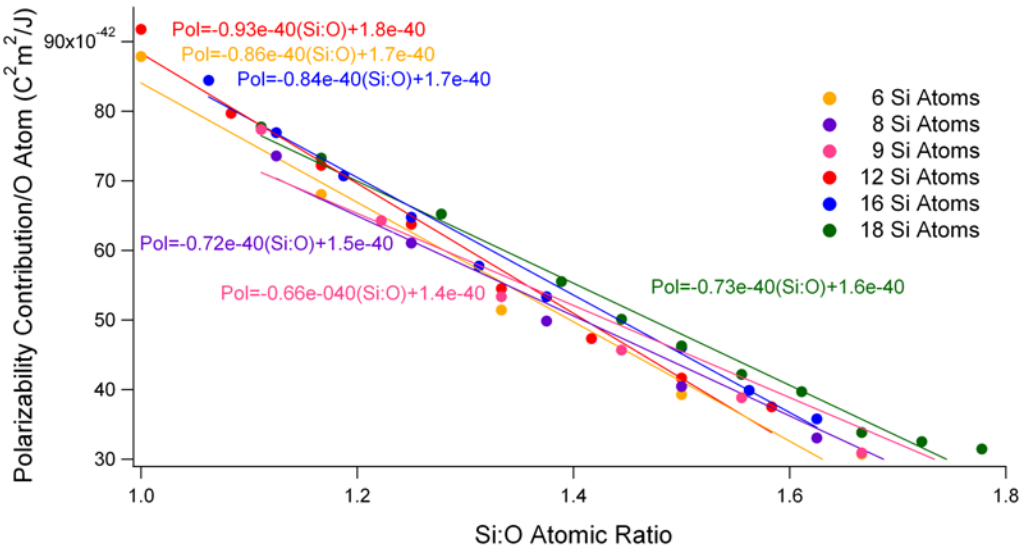

Figure 22. Change in system polarizability per additional oxygen atom versus the Si:O atomic ratio. The polarizability increases by a smaller amount with each additional oxygen atom added to the system.

Using this correlation, it was possible to reproduce the polarizabilities of the initial ten 100-atom structures to within 1-10% of the DFT-calculated polarizability values, as shown in Table 12.

The correlation was then applied to much larger systems of around 4400-6300 atoms modelled using the method described in Figure 5. This tested the ability of the correlation to predict reasonable polarizabilities for systems that are, in this case, 44-63 times larger than the test samples from which the correlations were obtained. Random numbers of Si, C, O and H atoms were present in the six large SiCOH systems tested. The density of the six systems varied from 0.89-1.49 g/cm^3 to conform to known experimental systems. [8, 16, 40, 45] The results are summarized in Table 12.

Table 12. Dielectric constants for six different model SiCOH systems (shown as columns 1-6) predicted using the correlation given in Table 11. The results were compared to experimental data on SiCOH films [40, 45] with the same densities (predicted k column).

Test System No.	1	2	3	4	5	6
No. Si Atoms	537	798	663	552	453	1256
No. C Atoms	1024	1086	1055	1012	885	858
No. O Atoms	526	952	715	525	383	2014
No. H Atoms	3030	3196	3138	3030	2694	2175
Total No. Atoms	5117	6032	5571	5119	4415	6303
Density (g/cm^3)	1.07	1.49	1.27	1.08	0.89	1.11
Calculated k	2.4	3.2	2.8	2.4	2.1	2.2
Predicted k	2.4	3.1	2.7	2.4	2.1	2.5

In all cases, the dielectric constant estimated by the correlation developed using DFT was within 5% of the experimentally predicted value for films of similar density and porosity [40, 45]. This error is roughly consistent with the known error in experimental determinations of the dielectric constant. While these results are encouraging, they merely indicated that the correlation does not produce unreasonable values for larger systems. The correlation was validated further by testing it against experimental data. [9] An experimental study by Volksen *et al*. focused on a film with a density of ~1.3 g/cm^3 and a composition of roughly 25% silicon, 41% oxygen, 11% carbon, and 23% hydrogen atoms. Based on this composition and density, the correlation predicts a dielectric constant of 2.55 while the experimentally determined value was ~2.7, further indicating the validity of this correlation.

I have established a correlation between the composition of an amorphous, porous SiCOH system and the resulting polarizability of the system. This correlation, in conjunction with the Clausius-Mossotti equation, can be used to estimate the dielectric constant of a large amorphous SiCOH-based system without the need for any simulation or other information beyond knowing the number of atoms in the system and the system size. When this correlation, established on systems of 3-20 silicon atoms, is extrapolated to predict the dielectric constant of much larger (several thousand-atoms) systems, the dielectric constant calculated from the Clausius-Mossotti equation is on the order of 2.2-2.5. This is within the range expected from experimental data, and previous work [8, 40, 45] has suggested that this type of estimate is fairly accurate. The existence of a correlation of this type allows a rapid estimation of dielectric constants of candidate SiCOH materials without the need for any computational simulations.

Mechanical Properties

Once the structural accuracy of the ULK model had been established, I also verified its mechanical properties. Mechanical property agreement between the simulated material and the experimental film is crucial for future computational work on this system, as ULK mechanical integrity is at the heart of problems surrounding ULK use in devices.

The elastic constants for a system are defined by the equation $\sigma_{ij} = C_{ijkl}\varepsilon_{kl}$, where σ_{ij} represents the system stress tensor and ε_{kl} represents the system strain tensor. The constants embodied by C_{ijkl} describe the elasticity of the system. [78] For an anisotropic homogenous material the symmetry of stress and elasticity tensors allows the stiffness tensor, C, to be reduced in order using Voigt notation. Using this mapping $\sigma_{ab}=\sigma_{ba}$, so $\sigma=(\sigma_{xx}, \sigma_{yy}, \sigma_{zz}, \sigma_{yz}, \sigma_{xz}, \sigma_{xy})\equiv (\sigma_1, \sigma_2, \sigma_3, \sigma_4, \sigma_5, \sigma_6)$, and likewise for ε. C_{ijkl} can therefore be expressed as $C_{\alpha\beta}$, where $C_{\alpha\beta}=C_{\beta\alpha}$, $\alpha=(1\text{-}6)$, $\beta=(1\text{-}6)$. [78] The elastic constants were calculated using the following procedure:

1. Equilibrate the system at 0 atm until a stable volume is reached.
2. Compress the system in a direction corresponding to the desired constant. For example, the C11 constant is based on compression in the xx direction, while the C44 constant is based on compression in the xy direction.
3. Re-equilibrate the system at the new compressed volume.
4. Measure the change in stress (pressure).
5. Calculate the desired constant.

Table 13 summarizes the compression directions used to find each constant. The term 'e' refers to the magnitude of the compression applied to the system. If the original length of a simulation box is x_0 and the length of the box after compression is x_1, then $x_0(1\text{-}e) = x_1$. σ refers to the stress (pressure) of the system after compression, in the designated direction.

After the elastic C11 and C12 constants were found, the bulk (K) and Young's (E) moduli were calculated using eqn. 7 and eqn. 8.

$$K = \frac{1}{3}(C_{11} + 2C_{12}) \qquad (7)$$

$$E = \frac{(C_{11} - C_{12}) x (C_{11} + 2C_{12})}{(C_{11} + C_{12})} \qquad (8)$$

The calculated elastic constants and bulk and Young's moduli are described in Table 14. The table only shows elastic constants for C11, C12 and C44. These represent an average of the three different directions associated with each constant. So, for example, C_{11} = ⅓(C_{11} +C_{22} +C_{33}).

Table 13 Compression directions associated with different elastic constants.

Constant	Compression Direction	Equation
C_{11}	xx	$\frac{1}{e}\sigma_{xx}$
C_{12}	xx	$\frac{1}{2e}(\sigma_{yy} + \sigma_{zz})$
C_{22}	yy	$\frac{1}{e}\sigma_{yy}$
C_{23}	yy	$\frac{1}{2e}(\sigma_{xx} + \sigma_{zz})$
C_{33}	zz	$\frac{1}{e}\sigma_{zz}$
C_{31}	zz	$\frac{1}{2e}(\sigma_{xx} + \sigma_{yy})$
C_{44}	xy	$\frac{1}{e}\sigma_{xy}$
C_{55}	yz	$\frac{1}{e}\sigma_{yz}$
C_{66}	xz	$\frac{1}{e}\sigma_{xz}$

Table 14 Elastic constants (C11,C12,C44),Bulk (K) and Young's (Y) Moduli

Constant	(GPa)
C11	4
C12	4
C44	2
K	4
E	1

In this study I also estimated the mechanical properties of SiCOH structures based on spin-on type films. The majority of this work has focused on the development of a model to mimic SiCOH films made using chemical vapor deposition (CVD). These films can also be made, however, using spin-on techniques. The resulting structures are much more ordered and possess fewer defining structural motifs. Two spin-on films I modelled were based on Si-CH_2CH_2-Si type structures and Si-CH_2CH_2-Si-CH_3 –type structures. This means all of organic material present in the Si-O based film was present in those described arrangements. So, in the first type, all of the organic material functioned as bridging bonds while in the second type one out of every six Si-O network bonds was replaced with an Si-CH_3 bond. The results comparing these to structures, as well as the CVD-type structure, are shown in Figure 23.

The results show that as the amount of organic networking in the films decreases, so do the mechanical properties. The first spin-on type film has excellent mechanical integrity, showing a Young's modulus of 78 GPa, and a bulk modulus of 37 GPa. Even if just one of every six Si-O networking bonds is replaced with an un-networked, pendant, Si-CH_3 bond, the Young's modulus is reduced to 35 GPa, and the bulk modulus is reduced to 18 GPa. The properties of the CVD film are obviously even worse, with a Young's modulus close to 1 GPa, and a bulk modulus of barely 4 GPa.

Conclusions

This study is distinct from past efforts in showing that the porosity, dielectric, and mechanical measurements are all in agreement with experiment (not just one or the other). This is the first time that all of these properties have been calculated for a given computational study. In particular, this chapter's discussion of the dielectric and mechanical properties showed how the porosity is the strongest influence on the dielectric constant, while the system networking is the key link to the resulting mechanical properties.

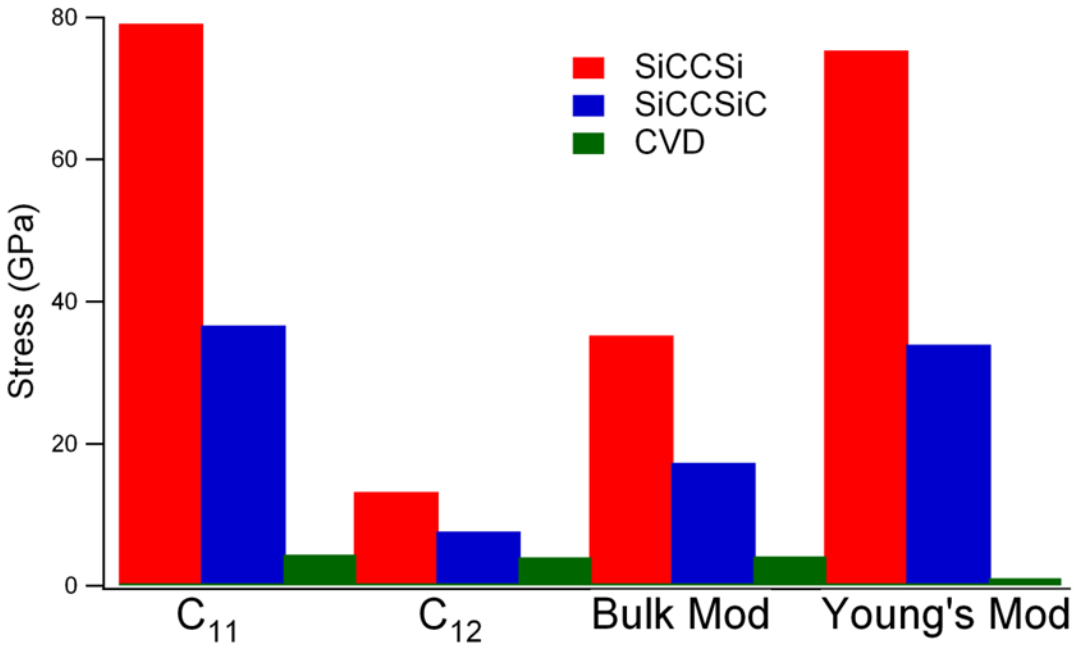

Figure 23. Mechanical properties of three types of SiCOH films: in red, a spin-on type film based on Si-CH_2CH_2-Si motifs; in blue, a spin-on type film based on Si-CH_2CH_2-Si-CH_3 motifs; and in green, a CVD type film based on all of the motifs shown in Figure 4. As the amount of organic networking decreases, the mechanical integrity of the film also significantly decreases. Just moving from the first spin-on type film to the second, where only one in six Si-O bonds are replaced, reduced the mechanical properties by approximately half. Moving to the CVD-type film, the mechanical properties are further cut dramatically.

CHAPTER 4

SIMULATED THERMAL ANNEALING OF ORGANOSILICATE GLASS MATERIALS

Having established an organosilicate glass model that simultaneously encapsulates structure, porosity, dielectric constant, and mechanical properties comparable to experimental materials, I am well positioned to understand how these properties are affected by ultra-rapid thermal annealing. UV curing techniques, currently the most popular in the semiconductor industry, are characterized by anneals on the order of minutes to hours. [7-8] The hypothesis was that rapid thermal annealing might favorably "shift" the dielectric constant *versus* mechanical property curve. Traditional Molecular Dynamics force fields are unfavorable for this type of study, as they do not allow for the evolution of the bonding topology during simulation. I therefore begin with a discussion of using the REAX force field to model SiCOH materials, which has the capability to embrace bonding changes. I then discuss the structural, porosity, dielectric, and mechanical changes that result from simulated rapid thermal annealing, using the previously established methods.

The REAX Force Field

There are few molecular-scale computational studies that characterize the properties of SiCOH films. Previous atomistic-scale simulation studies of SiCOH systems [18, 24-33, 53, 56] focused primarily on the relationship between the material's structure and its resulting mechanical properties. There has been no molecular-scale computational investigation into the evolution of the material structure during thermal annealing. This may be due, in part, to the nature of traditional Molecular Dynamics (MD) force fields which do not traditionally allow for

bonds to break or form during the course of the simulation. Clearly, in a situation such as this, where the intent of the processing is to reconstruct the bonding using a rapid thermal process, such force fields will be largely ineffectual in capturing the reorganization.

I overcame this difficulty by employing the REAX force field in my MD simulations to represent the interatomic potentials among the atomic species. The REAX force field was first described in 2001 by van Duin and Goddard to study reactions in hydrocarbons. [79] Since then, led by the van Duin group's parameterization of additional species, the force field has been successfully applied to a number of different applications. [80-87] This force field is almost unique in its approach to creating bonding definitions for use within MD simulations, in that the bonding topology can change and is continually updated throughout the course of the simulation. There is currently only one other such MD force field specifically designed to model bonding changes, COMB, which was originally developed to study materials used in the nuclear waste industry and has not focused on Si-C-O-H atom-type interactions until recently. [88] Bonding in REAX is determined based on interatomic distances and calculation of bond orders, which are updated each time step. Using this force field, I gain the ability to describe thermally induced structural and network bonding changes, and hence precisely demonstrate the effect of rapid thermal annealing on SiCOH films.

Rapid thermal annealing simulations of SiCOH films were performed using Molecular Dynamics techniques to solve the equations of motion of the system, and using the REAX force field to describe the forces between particles. Sandia's LAMMPS [51] code was used for all the MD simulations.

The REAX force field is the only input to the LAMMPS MD code beyond temperature and pressure settings. This force field is defined by a combination of 11 different possible contributions to the overall energy of the system, as described in equation 9.

$$E_{system}=E_{bond}+E_{lp}+E_{over}+E_{under}+E_{val}+E_{C2}+E_{tors}+E_{conj}+E_{H\text{-}bond}+E_{vdWaals}+E_{Coulomb} \quad (9)$$

In equation 9, E_{bond} is the bond energy, E_{lp} is the energy from lone electron pairs, E_{over} is the over-coordination energy – a penalty term for over-coordinated atoms, E_{under} is the under-coordination energy term, E_{val} is the angle-strain energy term, E_{C2} is a correction term for carbon-carbon double bonds, E_{tors} is the torsional energy, E_{conj} is the torsional conjugation energy, $E_{H\text{-}bond}$ is the energy from hydrogen bonding, $E_{vdWaals}$ is the energy from van der Waals interactions, and $E_{Coulomb}$ is the Coulombic interaction energy. Energies derived from bonded interactions are calculated based on the bond orders of each atom so that, as bonds are created or destroyed, the energies are able to adapt easily. Pair-wise interactions like van der Waals and Coulomb interactions are calculated between every pair of atoms. [79] The REAX parameters were used, without alteration, from the list available for Si, C, O and H, provided in private communication with Prof. Adri van Duin (Penn. State University). This is a slight drawback to the use of the force field, in that the parameterization is dense (upwards of 100 parameters) and not well described in the literature, and so there is a reliance on Prof. van Duin's group for these values. The force field is also known to be better at bond-breaking than forming, and so may not show the structural rearrangements we hope to observe because of this bias.

Computational Methodology: MD Methods

The system consisted of approximately 6,500 atoms, which were initially laid out in a grid-like configuration using an algorithm described elsewhere [89-90] to create a typical SiCOH-like

amorphous porous material. The overall box size was 105Åx105Åx105Å, for a total volume of 1.1E6Å^3. The actual sample within the box was laid out on a 44Åx44Åx44Å grid, for a total volume of 8.5E4Å^3. That is, the system set-up consisted of a sample surrounded by a vacuum layer, extending 30Å in each direction. This was designed to allow organic species to escape during the thermal annealing.

The system was then annealed at 25°C for 1 ns of simulation time, using a time step of 0.25 fs, in an NVT ensemble, with periodic boundaries in all directions. After thermal equilibration at 25°C, the system was heated to 1900°C over the course of 190 ns (~800 million time steps) of simulation time, at a rate of 10^{10}°C/s, at constant volume. The system was also heated initially without the vacuum layer, using the same temperature range and heating rate, at a constant pressure of 1 atm, in order to observe the effect of increasing temperature on the system volume. This allowed for the estimation of a glass transition temperature (Tg) for the system and therefore better understand the overall thermal profile of the system.

Verification of a REAX model for SiCOH thin films

As noted in the preceding section, the aim was to explore the thermal profile of SiCOH films using MD techniques and use of the REAX force field. I created and then verified the accuracy of a model for the SiCOH system using REAX to define the interactions among the atomic species (C, H, O, Si). REAX replaced the previously reported combination of intermolecular potentials (Stillinger-Weber and the Optimized Potential for Liquid Simulation – henceforth S-W and OPLS, respectively) that I used successfully to characterize SiCOH films. [51-52] Clearly, the annealing application that is the focus of this work renders traditional force fields unusable.

The SiCOH system was laid out geometrically using the grid-based structure generation algorithm. [51-52] Employing the REAX force field to describe the forces between each of the species in the system, I simulated equilibrating the SiCOH system at a constant volume of 1.1E6$Å^3$ and 25°C for 1 ns of simulation time (in an NVT ensemble), with a time step of 0.25 fs. The first step was to verify the structural composition and bonding against that used in the earlier (S-W/OPLS) rendition of the material. The results are shown in Figure 24.

I also verified that the REAX-modeled simulated system exhibited a pore size distribution, porosity, and predicted a dielectric constant that agreed with experimental films of a similar nature, using methods described elsewhere. [51-52] The film discussed in this dissertation consisted of approximately 6,500 atoms, corresponding to a density of 1.4 g/cm^3, a porosity of 11%, an average pore diameter of 0.9 nm, and a predicted dielectric constant of 2.6. These properties correlate well with typical experimental SiCOH films. [40]

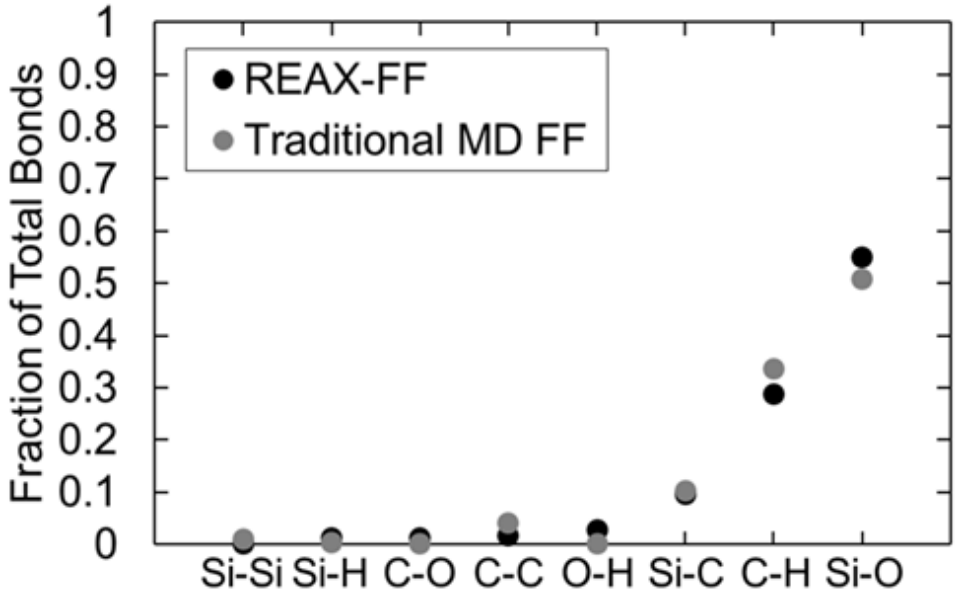

Figure 24. Bonding distribution predicted using REAX force field models for the simulated SiCOH system. As expected, the system is dominated by silicon-oxygen bonding (~60%), indicating the presence of the underlying silicon-oxygen framework. Carbon-hydrogen (~28%) and silicon-carbon (~10%) bonds are the next most prevalent. Carbon-hydrogen bonds result from the presence of $-CH_3$ and $-CH_2$ organic elements; silicon-carbon bonds result from the substitution of organic moieties into the silicon-oxygen framework. All remaining bond types have a low occurrence, as expected. This compares favorably to bonding distributions predicted by more traditional MD force fields (S-W/OPLS), where bonding is pre-determined by the initial set-up.

Thermal Annealing

REAX/MD simulation to estimate the glass transition temperature, Tg

Having verified that the computational model behaved similarly to experimental SiCOH materials, the next task involved developing a point of comparison between the thermal profiles predicted by the simulated and laser-annealed films. While MD simulations are able to accurately predict the evolution of property changes within a suitably modeled simulated material, there is no guarantee that the temperatures indicated in the simulation for these property changes will match real-world temperatures. Thus, the prediction of particular temperatures (boiling point, melting point, critical point, *etc*.) is typically a fairly stringent test of a simulation model and method. I used the glass transition temperature Tg, the point at which the amorphous material 'melts' or becomes fluid (*i.e.*, the devitrification temperature), to compare simulated and experimental thermal profiles.

This presented its own challenges, as the experimental glass transition is not well-defined for this class of materials. This is due to the materials' varied compositions and porosities, the effect of the heating rate on the apparent Tg value, and the difference in behavior of the organic features of the film and the underlying Si-O framework. The experimental complexity of Tg measurement, also makes it difficult to determine accurately. Tg of amorphous SiO_2 is well known to be 1200°C, and is an upper limit to so the Tg of SiCOH. [91] The actual Tg has been reported to be as low as 600°C. [3] Consequently, the Tg of SiCOH must be in the range 600-1200°C.

When I originally created an MD model for this SiCOH system, I used the Optimized Potential for Liquid Simulations (OPLS) [51] to describe the Si-CH interactions, and the

Stillinger-Weber [52] potential to describe the Si-O interactions. The details of this combination of models can be found in the structure generation section.

Having established a model for the system using these force fields, I initially attempted to use this combination of models to determine Tg. The system was heated from room temperature at 1 atm in a constant temperature, constant pressure (NPT) ensemble until a transition in the physical state of the system was observed. This transition was noted in one of three ways: as a change in system volume, the average coordination numbers of oxygen and silicon, or the radial distribution functions. The system was heated to an extremely high temperature of 4700°C (5000K) at a heating rate of 10^{11}K/s over the course of 37 ns, with a time step of 0.25 fs.

The OPLS force field includes bond, angle, and dihedral parameters to define the Si-C bonds. These bonds do not contribute significantly to the underlying framework of these materials, and so I did not investigate them closely when looking for the glass transition point. However the transition should be visible in the Si-O behavior, as these interactions account for the structural integrity of the material. This means that a proper understanding of the Stillinger-Weber Si-O description is critical.

Part of the process in studying the silicon-oxygen interaction originally was determining the correct parameterization of the Stillinger-Weber (SW) interaction. The parameterization I used was based on a 1999 study by Watanabe *et al.*, entitled "Novel Interatomic Potential Energy Function for Si,O Mixed Systems." [52] Their study employed a two-body term and a three-body term, as is typical for the Stillinger-Weber potential. Their three-body term parameterization matched that provided in Sandia's well-used LAMMPS incorporation of the Stillinger-Weber three-body term. I used LAMMPS as a source of the Molecular Dynamics code to study these

materials. [50] However, there exists a difference in formalism between the Stillinger-Weber two-body term used by LAMMPS (eqn. 10) and that in the Watanabe *et al*. paper (eqn. 11).

$$\emptyset_2(r_{ij}) = A_{ij}\varepsilon_{ij}\left[B_{ij}\left(\frac{\sigma_{ij}}{r_{ij}}\right)^{p_{ij}} - \left(\frac{\sigma_{ij}}{r_{ij}}\right)^{q_{ij}}\right]\exp\left(\frac{\sigma_{ij}}{r_{ij}-a_{ij}\sigma_{ij}}\right) \quad (10)$$

$$\emptyset_2(r_{ij}) = \mathbf{g_{ij}}A_{ij}\varepsilon_{ij}\left[B_{ij}\left(\frac{\sigma_{ij}}{r_{ij}}\right)^{p_{ij}} - \left(\frac{\sigma_{ij}}{r_{ij}}\right)^{q_{ij}}\right]\exp\left(\frac{\sigma_{ij}}{r_{ij}-a_{ij}\sigma_{ij}}\right) \quad (11)$$

It is evident that the two equations are identical with the exception of the g_{ij} term in the Watanabe equation, which essentially controls the strength of the interaction. This g term is equal to 1 for oxygen-oxygen and silicon-silicon interactions; however, for oxygen-silicon interactions, it is a function of the coordination number of oxygen. Table 15 shows the value of g for different coordination numbers of oxygen.

Table 15. g_{ij} function values for different coordination number of oxygen

Coordination Number	g value
0	0.305
1	0.813
2	1.00
3	0.46

The coordination number of a given oxygen atom is determined based on the distance between that atom and its nearest silicon neighbors. The function is designed so that the binding energy between silicon and oxygen is strongest at a coordination number of two. This proved to be problematic in the calculations as it appears that the g value for a coordination number of two causes the attraction between silicon and oxygen atoms to be so strong that the structure of the material is completely uninfluenced by temperatures as high as 4500°C. Indeed, no glass transition was observed for a g(2) value anywhere in the 25-4700°C temperature range.

The heating process was then repeated using other g values given in Table 15. For g=0.813 corresponding to an oxygen coordination number of one, a glass transition was observed at ~2500°C as determined by the change in system volume upon heating (see Figure 25). For values of g corresponding to coordination numbers of either zero or three, glass transitions were found to occur near 1250°C and 2300°C, respectively. These transitions are summarized in Figures 25 and 26. Thus, unless g is treated as essentially an adjustable parameter, thereby losing any physical meaning as a coordination number, there were no values of g from 0.3-1.0 that lead to an experimentally reasonable glass transition temperature. The overall results suggest that this combination of OPLS+ SW potentials is not suitable for thermal annealing, since g has become an arbitrary parameter. The most reasonable value of g (corresponding to oxygen coordination of two), produces an unrealistic Tg in excess of 4700°C.

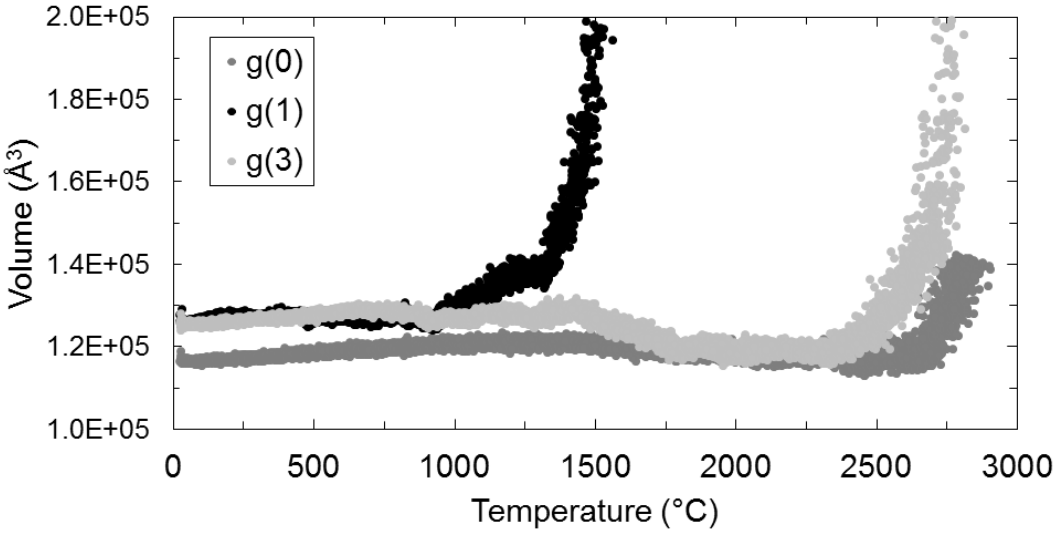

Figure 25. Volume versus temperature curves for the constant-pressure thermal annealing of the OPLS+SW models with g(0), g(1), and g(3) values for the SiCOH systems. Transition temperatures are observed near 1250°C, 2300°C, and 2500°C, respectively, for the three values of g.

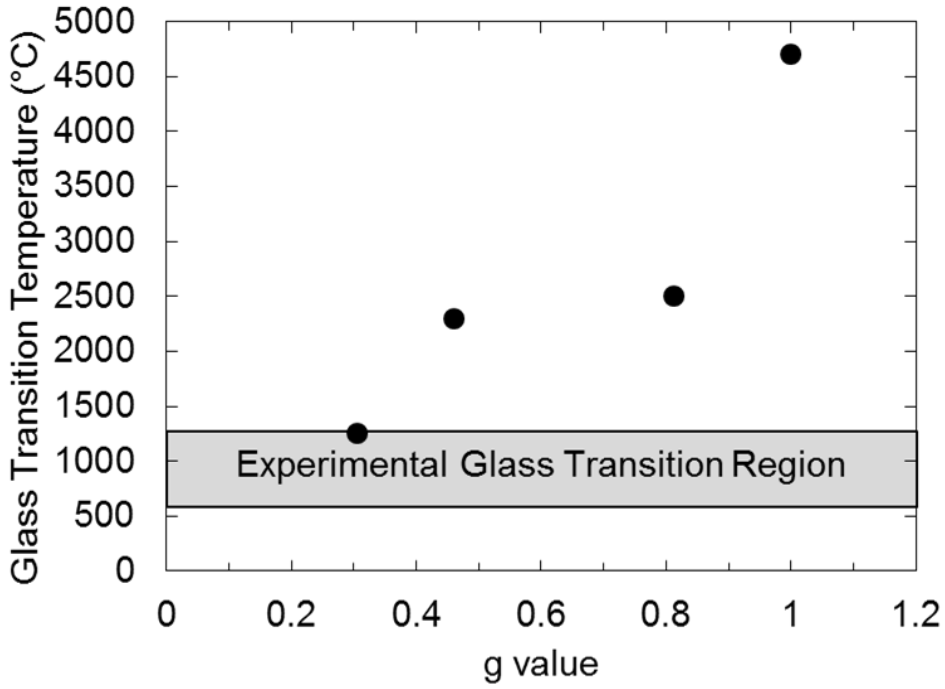

Figure 26. Estimated glass transition temperature as compared to the value of g for the SiCOH system. Clearly, there is an increase in Tg with increasing g, as the Si-O interactions become stronger. A g value of one, corresponding to an oxygen coordination number of two, suggests an unreasonably high Tg value indicating that this combination of force fields is unsuitable for thermal annealing processes.

After establishing that traditional MD force fields are unsuitable for thermal annealing, I proceeded to anneal using the REAX force field. Following equilibration, the simulated system was first subjected to thermal annealing under constant pressure in order to establish the overall system behavior at the pressure used in experiments and to estimate the MD-predicted value of Tg. I estimated the simulation-generated value of Tg based on two metrics: changes in volume while annealing at constant pressure, and changes in the average mean squared displacement (MSD) across all the atoms in the system. As the system transitions out of the glassy state and begins to devitrify or "flow," the volume will rapidly increase, as shown in Figure 27.

I was able to demonstrate that the REAX/MD-generated glass transition, at an annealing rate of 10^{10}°C/s over the course of 190 ns, was around 1180°C. It should be noted that heating rates in MD simulations are typically extremely fast, with 10^{10}°C/s being the slowest rate I could achieve with the computational resources available. A simulation at this heating rate requires one to three months of run time depending on system size (in the range 1,000-10,000 atoms).

In terms of self-consistency, I confirmed the estimated Tg value of 1180°C by also looking at the change in the average MSD from one time step to the next during thermal annealing. That is, I looked at the average MSD of all atoms in the system at one time step, and then looked at the average MSD at the next time step, and evaluated the difference. As the temperature increases and the system passes through Tg, the difference in the average MSD between time steps should increase.

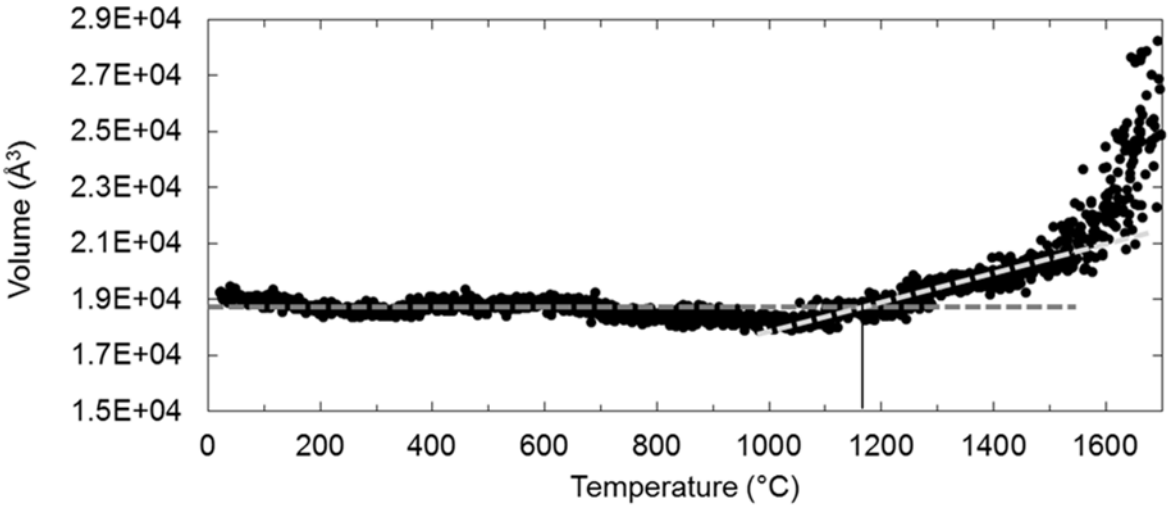

Figure 27. Change in simulation system volume of a 6,500-atom SiCOH simulated material thermally annealed at a constant pressure of 1 atm. The system volume steadily increases starting at 1000°C. Using the typical estimation of Tg as the intersection of the solid and melt phases, I estimate a Tg value of ~1180°C. The rapid increase in volume starting at ~1550°C corresponds to the vaporization of the system.

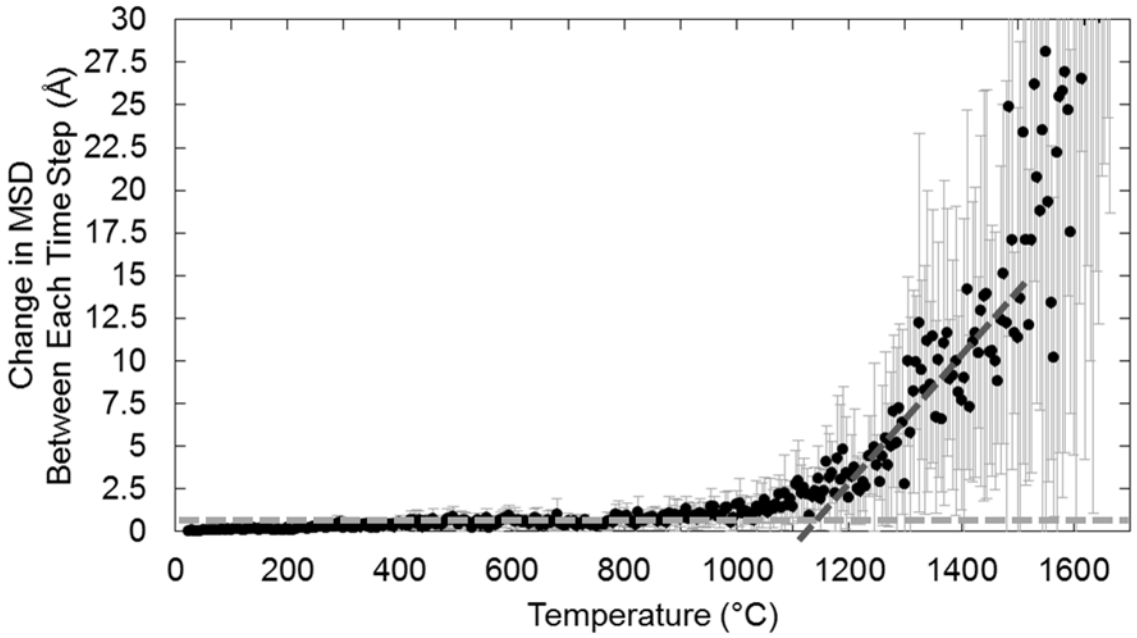

Figure 28. Change in average MSD between time steps as the system is thermally annealed at 1 atm. The difference between the mean squared displacement is averaged over the movements of all the atoms in the system from one data point to the next, showing larger changes in the average atom movement as temperature increases. The points represent the average change in MSD for a given temperature, while the error bars show the range of MSD changes. The average change in MSD begins to increase from between 0-2Å to 5-15Å in the previously estimated glass transition region between 1000°C and 1500°C, with the slope of the melt region suggesting a Tg around 1120°C (the intersection of the two tangents shown).

Figure 28 shows an exponential increase in the change in MSD starting at ~1000°C, with variations in excess of 5Å starting at around 1200°C. Thus, the MD-predicted value of Tg lies in the range 1000-1200°C and is likely to be ~1100°C. Since the simulation value is an unfitted prediction, based on extremely rapid heating, and given the uncertainty in the experimental value, the predicted value of Tg was deemed to be sufficiently good as a reference point for the thermal response of rapidly annealed simulated SiCOH films.

Rapid thermal annealing of a SiCOH film

Encouraged by the preceding estimation of Tg, I undertook a thermal annealing process at constant volume. Keeping the volume constant allowed for the creation of a vacuum around the system, allowing atoms to "escape" the thin film during processing as they would in experiments. Figure 29 shows a snapshot of the simulation clearly demonstrating this situation.

Once the vapor phase was established at room temperature, I observed the system as it was heated to 1900°C (well above Tg) at a rate of 10^{10}°C/s.

During annealing I am most concerned with changes in the system bonding topology. I looked at changes in the bonding between all types of atoms in the system, as well as changes in different key groupings (*e.g.*, SiO_4, SiO_3R, SiO_2R_2, etc.). The results predicted by the REAX-modeled system showed two key changes: a loss in the presence of organic units (a decrease in Si-C bonding while C-H bonding remained constant), and an increase in Si-O networking at the expense of silicon sub-oxides (a silicon atom bonded to less than four oxygen atoms).

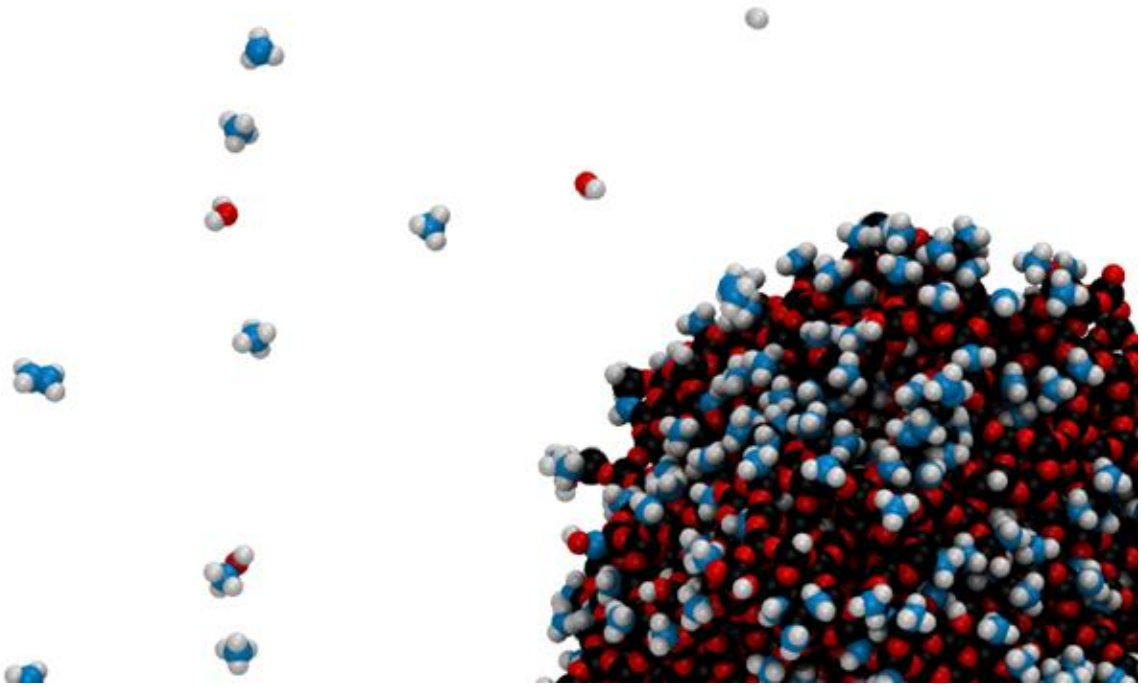

Figure 29. Representative snapshot of the edge of the simulated SiCOH system at 800°C showing the establishment of a vapor phase around the SiCOH solid. Silicon atoms are shown in black, carbon atoms are shown in blue, oxygen atoms are shown in red, and hydrogen atoms are shown in white. It is clear that the vapor contains exclusively organic moieties (no escaped silicon atoms). Image prepared using Visual Molecular Dynamics (VMD). [45]

The first observed change in the simulated system began at 400-500°C with loss of organic units from the main silicon-oxygen framework. This increase in free carbon atoms, not bonded to any part of the silicon-oxygen framework, is shown as a function of temperature in Figure 31. Bonds were counted by calculating the distances between all pairs of atoms in the system, and determining whether an atom pair was bonded or not-bonded based on whether their distance were within a pre-determined threshold. For silicon-carbon bonds, for example, this distance was 2.5 Å. This value was chosen by observing the first nearest neighbor distance in the radial distribution function for this pair of atoms (Figure 30).

Following the loss of organic units, there is an increase in silicon-oxygen networking as the underlying silicon-oxygen framework responds to the loss. This was quantified by comparing the number of fully-networked silicon atoms (SiO_4 units) and silicon-suboxides (SiO_3, SiO_2, SiO units), as a function of temperature. As shown in Figure 31, there is an increase in the extent of silicon-oxygen networking starting at 700-800°C, some 200-300°C above the initial loss of organic units.

In order to better understand the nature of organic loss, carbon bonding was studied in further detail (Figure 32). The analysis shows that the extent of carbon-hydrogen bonding remains relatively constant across all temperatures. This is expected as hydrogen atoms are only present in the form of carbon-hydrogen bonding, and the organic units within the system remain intact throughout the simulation. Carbon atoms bonded to the Si-O Network – that is carbon atoms bonded to a silicon atom or networked oxygen atom – steadily decrease in number throughout the simulation with a more rapid decrease once the system exceeds the glass transition temperature.

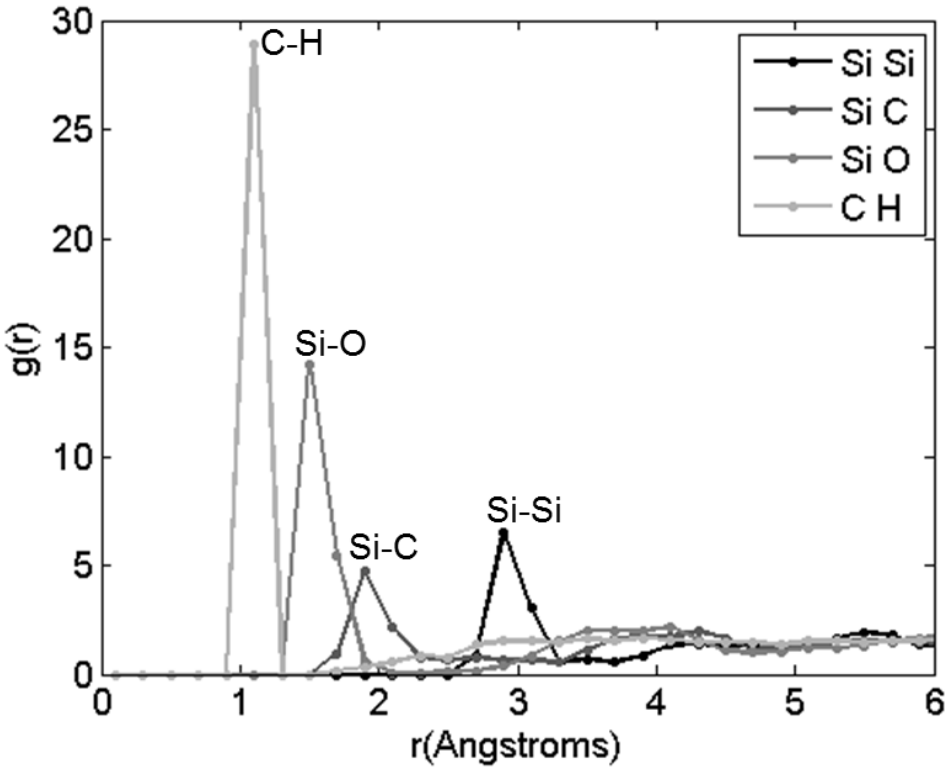

Figure 30. Radial distribution functions (RDFs) for silicon-silicon, silicon-carbon, silicon-oxygen, and carbon-hydrogen interactions resulting from simulating the system using the REAX force field. These curves suggest the most common distances for neighboring pairs of atoms of these types, and therefore the bond length for these atom pairings. Si-Si bonds are approximately 3 Å in length, Si-C bonds are 2 Å long, Si-O bonds are 1.7 Å long, and C-H bonds are 1.2 Å long. RDFs for other atom pairings not shown (*e.g.*, Si-H, C-C, C-O, O-H), were present in numbers too low to be strongly correlated, and bond lengths for these interactions were assumed to be on the order of 1 Å. This may introduce some small error in bond counting, but the bond counts for these bond types were less than 20 bonds for the entire system, in comparison to bond counts in the hundreds and thousands for the bond types shown in the figure (29) above, and so would not significantly affect the analysis of the bonding in the system.

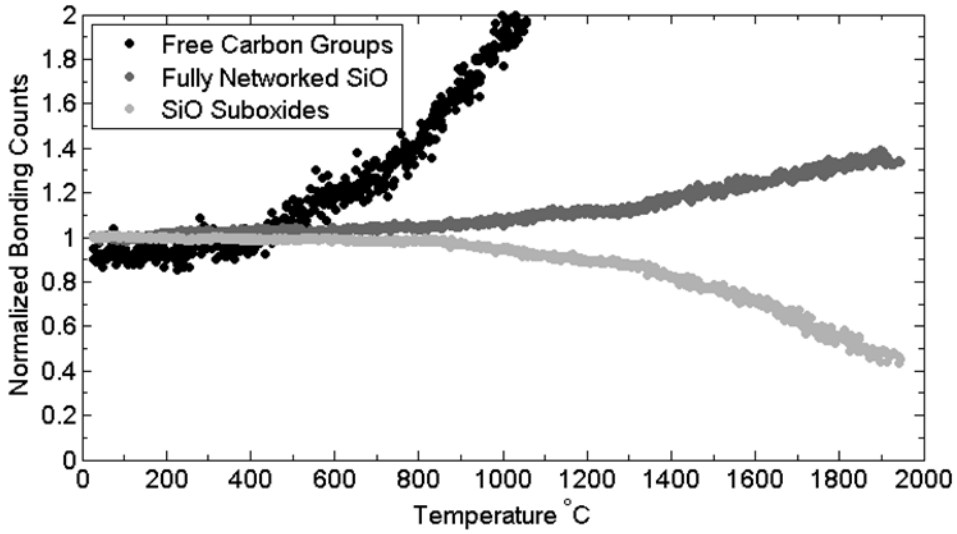

Figure 31. Change in silicon-oxygen networking and carbon-group networking with temperature, as predicted by MD simulations using the REAX force field. This chart shows an increase in fully networked SiO_4 starting at 700°C, with a simultaneous loss of silicon suboxides. The rate of networking improvement and suboxide loss increases beginning at around 900°C. There is also an increase in free carbon groups - that is, carbon atoms not bonded to either silicon or oxygen atoms - beginning at around 500°C, with a slight increase in organic loss rate beginning at 800°C.

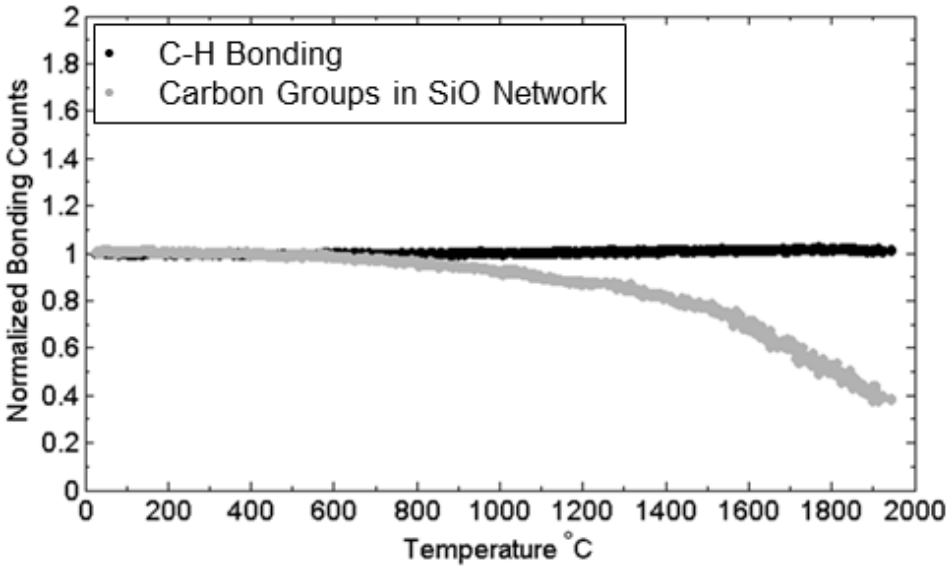

Figure 32. Changes in carbon bonding versus temperature. This confirms the loss of organic units in the system since networked carbon bonding decreases, while carbon-hydrogen bonding remains essentially constant throughout. The extent of networked carbon decreases very slightly throughout the simulation, with a visible deviation from the baseline occurring only at ~600°C, followed by an increased rate of organic loss for the remainder of the simulation.

The extent of carbon-oxygen and carbon-carbon bonds are not shown since they were present in low numbers (<300 bonds of each type, compared to 3,250 carbon-hydrogen bonds and 1,500 carbon-silicon bonds), and remained constant throughout the simulation.

Overall, these MD simulation results, predicted using the REAX force field, suggest that a favorable rearrangement of organic units within the system as a result of thermal annealing treatments is unlikely; carbon atoms prefer to leave the system rather than change their bonding behavior within the silicon-oxygen network. Using an estimated simulation Tg of 1180°C, the results suggest that organic units will begin to leave the system at about 0.5Tg, followed by an increase in Si-O networking beginning at about 0.67Tg.

Experimental Results

Figure 33 shows FTIR spectra of two films, one annealed at low temperature (300 °C) and one annealed at high temperature (1200 °C), covering only the range of the Si-O peaks. The behavior of the system is dominated by loss of the SiO sub-oxide peak at 1027 cm^{-1} and the commensurate rise of the fully networked peak at 1061 cm^{-1}. The ladder and cage peaks are reduced as well, but not nearly as strongly as the sub-oxide peak. The methyl peak is almost entirely removed by 1200° C.

These data are summarized in Figure 34 showing the normalized peak area as a function of the annealing temperature for a 1 ms LSA anneal. In addition to the Si-O peaks, data for the organic (methyl) peak at 1274 cm^{-1} are also shown. At temperatures below 800°C, the FTIR peaks remain essentially unchanged. The organics, particularly the pendant methyl groups, are the first structure to become unstable and above 850°C they begin to decompose. No substantial organics remain at temperatures above 1200°C.

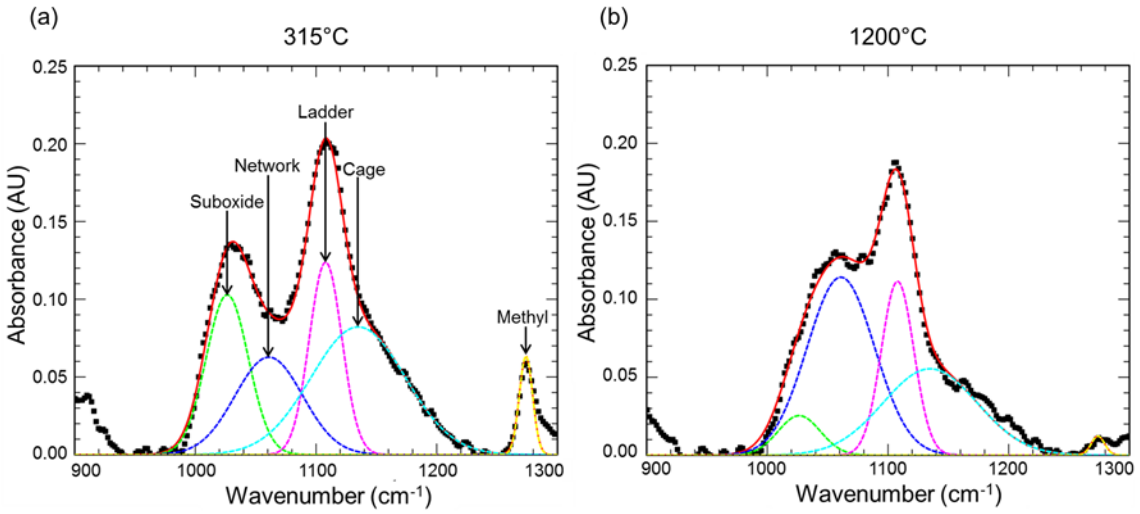

Figure 33. FTIR spectra of samples annealed at 315°C (a) and at 1200°C (b). Extracted FTIR peaks for the Si-O structures are shown as dashed curves. The dominant effect of temperature is an increase in the intensity of the Si-O network peak at the expense of the methyl and Si-O suboxide

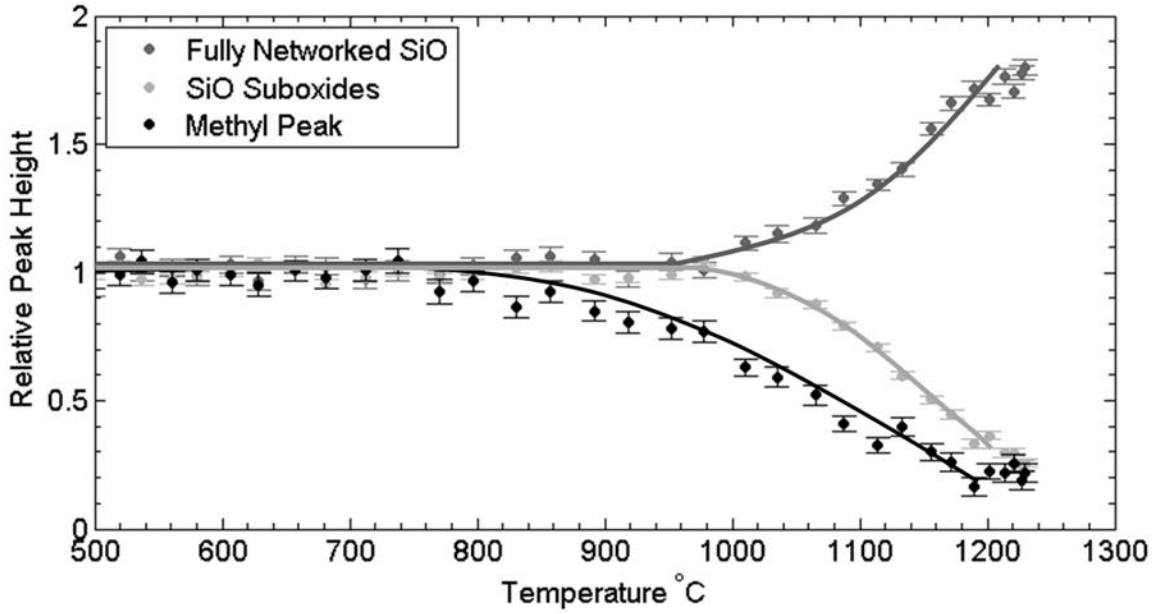

Figure 34. Peak heights of suboxide structure (light grey symbols), fully networked structure (medium grey symbols), and methyl groups (black symbols) taken from FTIR spectra over a range of annealing temperatures. Peak heights are scaled relative to unannealed regions located some distance removed from the laser scan. Lines are a guide to the eye only. The methyl peak begins to decrease in area around 850°C, followed by an increase in SiO networking at 1000°C, and a symmetric loss in SiO suboxides also beginning at 1000°C.

The network structure, as formed, remains stable to temperatures above 1000°C. Thus, the primary effect with increasing temperature is conversion of sub-oxide structures to the fully networked configuration. Again, for a 1 ms anneal, this requires significant additional temperature with full conversion of sub-oxide structures only possible at temperatures above 1200°C. This behavior is consistent across dwell times from 200 μs to 2 ms with only small shifts in the critical temperatures.

Comparison of computational and experimental results

The computational MD thermal annealing simulations of SiCOH materials using the REAX force field, and the experimental LSA treatments of SiCOH films characterized by FTIR spectra, predict the same structural changes as a function of temperature. Both studies show a loss of organic units from the underlying silicon-oxygen framework followed by an increase in silicon-oxygen networking.

The experimental studies show FTIR methyl peak loss beginning at 850°C, followed by an increase in the Si-O networking FTIR peak at around 1000°C. The computational studies show these changes beginning to occur at lower temperatures, with a much more gradual rate of change. Both experiment and computation predict that there is roughly 150-200 °C difference between the loss of organic moieties and the densification of the Si-O framework.

The atomic-level detail possible with the computational results is able to identify deviations in the fully networked silicon-oxygen moieties and the silicon sub-oxides at temperatures as low as 600°C; however, this deviation does not become substantial (which I estimate, arbitrarily, to be synonymous with a 10% change in bonding behavior as compared to the initial system) until around 900°C. Experiments cannot be expected to observe the earliest-stage bonding differences

possible in simulations; but it is encouraging that the experiments show observable changes in the FTIR at ~850°C , which corresponds to a change of less than 10% of the original bonding found computationally. Similarly, computational results show organic units leaving the system at temperatures as low as 500°C, but with an increase in the rate of loss at around 800°C. These results are summarized in Figure 35.

Simulation results show the same structural changes as the experimental studies, but beginning at lower temperatures than the experimental system, and progressing at a slower rate. In the future, it may be of interest to anneal the simulated system at the various transition temperatures for longer time periods, to see if the extent of structural change is greater at lower temperatures than is suggested by the rapid anneal rate. Both the experimental and computational studies do, however, eventually reach the same end-point (little-to-no organic units left in a fully-networked Si-O system). Ideally, a comparison of the temperature at which the simulation and experimental structural transitions occur is best made in terms the glass transition temperature. The simulations show that these changes occur at about 0.5 Tg and 0.67 Tg, respectively. Such a comparison to the experimental system is currently impossible. What can be definitively concluded when comparing the results of the experimental LSA and the MD simulations is, that once the SiCOH system passes through its glass transition temperature, the organic units will completely escape the system, leaving behind a fully networked, amorphous Si-O framework.

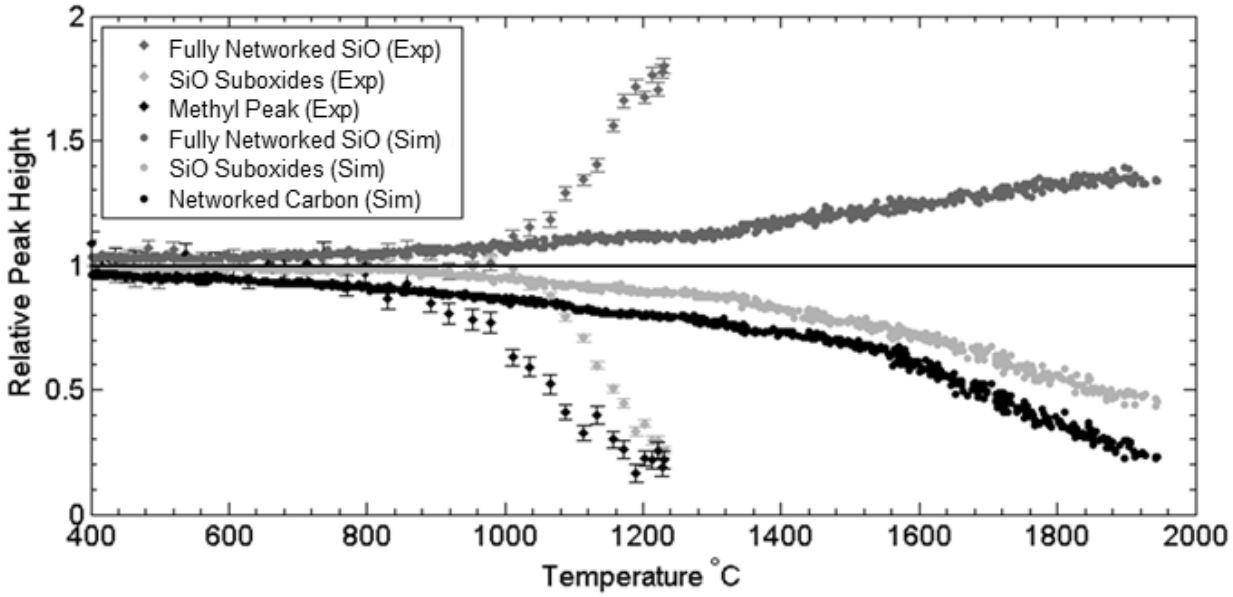

Figure 35. SiCOH structure as a function of temperature in both the MD simulated system and the experimental LSA system. Both the experimental and simulation studies show a loss of organic material, followed by an increase in Si-O networking at the expense of silicon sub-oxides. The computational results show these changes beginning at lower temperatures than the experimental studies, but occurring at a slower rate. The end point of both the experimental and simulation studies is the same, however, with the organic units completely leaving the system.

Porosity Changes during Thermal Annealing of SiCOH Materials

Having observed the structural changes that result during simulated thermal annealing of the SiCOH material using the REAX force field, I investigated whether the porosity also changed concomitantly. As the organic units leave the system, the remaining bulk appears to increase its networking and "densify," which would suggest a decrease in system porosity, and a decrease in average pore diameter.

To study this, I chose 11 equally spaced snapshots of the system along the thermal profile and then used the porosity algorithm described in Chapter 2 to investigate the change in porosity as a function of annealing temperature. The results shown in Figure 36 below suggest that the overall porosity of the SiCOH material begins to decrease around 900°C. This corresponds well with the increased Si-O networking discussed previously, and follows expected trends. Figure 37 also shows that there is a change in the pore size distribution with increasing temperature with larger pores collapsing to form smaller pores. The average pore diameter shifts slightly from 1.0 nm to 0.9 nm. It is an anticipated that this trend would continue to higher temperatures where further densification is expected to occur; however, this is outside the realm of processing interest.

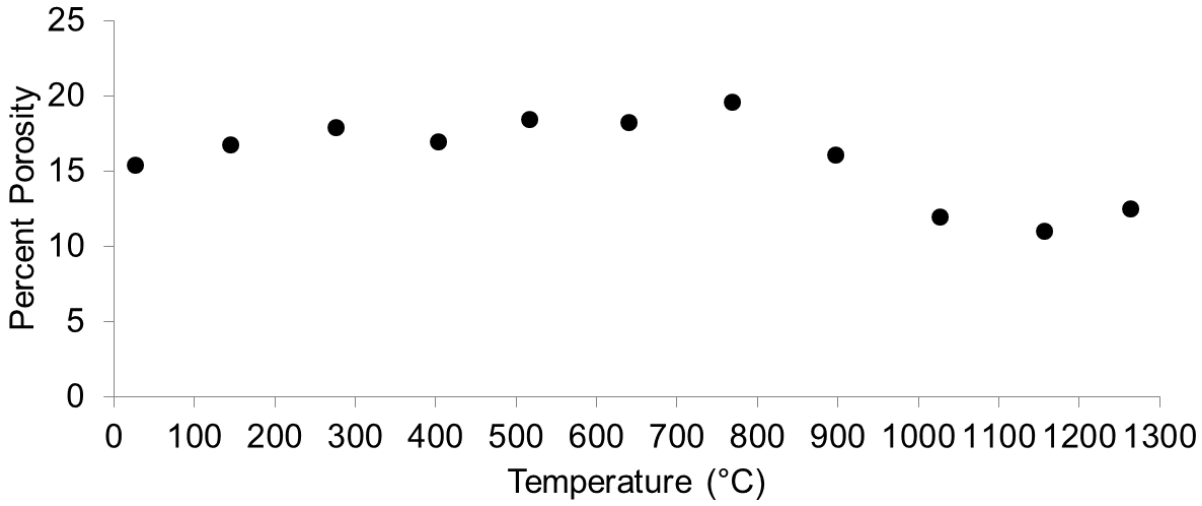

Figure 36. Change in porosity of the annealed SiCOH material with temperature. The porosity is relatively steady during the early annealing process, and even increases slightly as organic material is lost to the surroundings. Once the Si-O networking begins to increase at 900°C, however, the porosity decreases rapidly, and the film begins to densify.

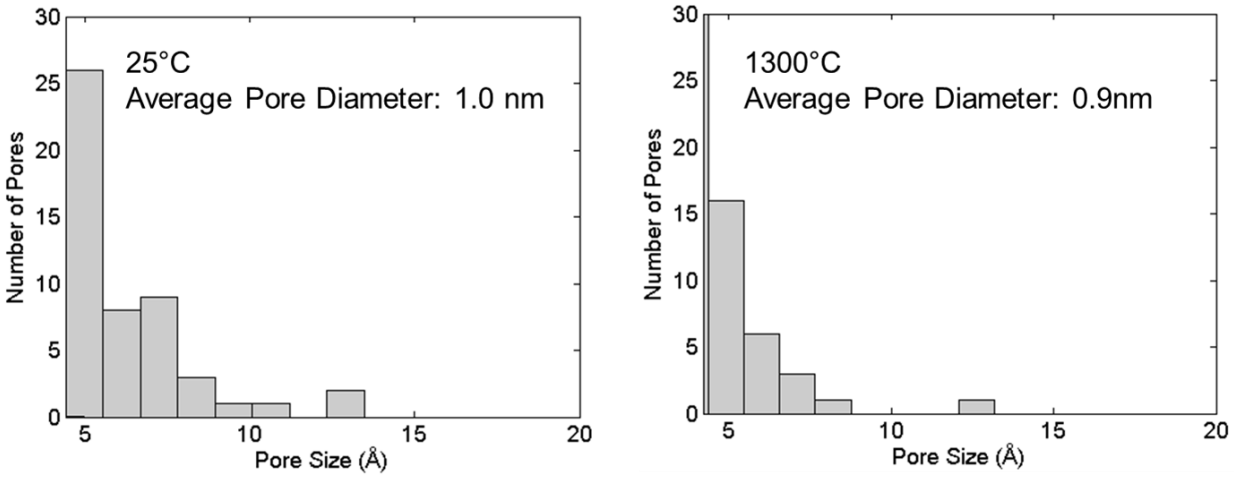

Figure 37. Pore size distributions of the annealed SiCOH material at room temperature, and 1300°C. There is a shift in the pore size distribution as large pores are lost and smaller pores form.

Monitoring the Dielectric Constant during the Thermal Annealing of SiCOH thin films

In a similar manner, I also investigated trends in other macroscale properties, including the dielectric constant. The main task was to determine whether changes in the dielectric constant and mechanical properties mirror the microstructural changes that I observed earlier as the SiCOH material is annealed.

In order to estimate the change in dielectric constant as a function of temperature, I used the previously developed correlation to estimate the polarizability of the structure of the SiCOH material in a given thermally annealed state. In the simulated system, the composition and volume of the bulk SiCOH material constantly varies as a function of temperature as organic material is lost to the surrounding environment. Therefore, the resulting calculation of dielectric constant will also vary as a function of temperature, following changes in the composition of the material. This will provide an estimate of how the resulting dielectric constant is affected by thermal annealing processes.

In order to use the correlation, however, it was necessary to develop a method to determine the volume of the bulk material, which constantly changes during annealing as a result of the changing material composition. By including a vacuum layer around the edges of the system, atoms are able to leave the vicinity of the main bulk of the material. The volume of the simulation box is, therefore, meaningless as a measure of the volume of the actual bulk system since it includes a considerable vapor volume. This approach to solving this problem was to use the center of mass of the silicon atoms in the system to locate the approximate center of the bulk material, and then search outwards from that point in all directions to locate the surface of the bulk material. The silicon atoms can be used as a monitor of the behavior of the bulk material because they do not leave the system during the annealing process.

This process works well in general; however, it can be difficult to pin-point which atoms are part of the bulk material and which atoms are essentially part of the vapor but physically close to the material's surface. It was therefore necessary, when determining whether or not an atom was connected to the main bulk of the material, to calculate its proximity to several nearest neighbors, not just its proximity to one atom. For "floater" atoms near the surface there will be a discontinuity in the pairwise distances when crossing the "gap" between this atom and the surface, which is not present in atoms which are truly part of the main "bulk." Using this method to estimate the volume of the structure at each point along the thermal processing path, and the previously developed dielectric constant correlation, I was able to observe the trend shown in Figure 38.

The trend shows that the dielectric constant is initially fairly stable, although it does start very slowly increasing as soon as annealing starts. At around 900°C, when the organic material is rapidly leaving the Si-O networking is increasing, the dielectric constant begins to rapidly increase. This would be expected based on the previously observed structural changes in the material: film densification correlates with an increase in dielectric constant.

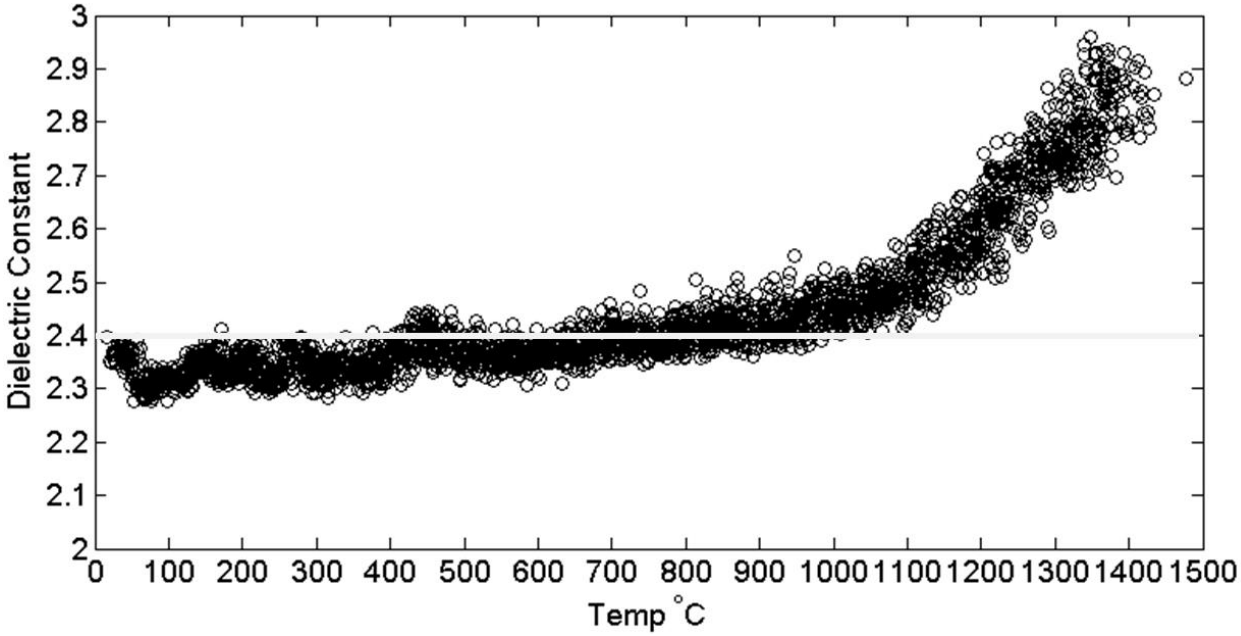

Figure 38. Change in estimated dielectric constant versus annealing temperature for a SiCOH system. The results show that, as anticipated, the dielectric constant of the system increases as the film goes through a transition at ~900°C and begins to densify.

Mechanical Properties During Thermal Annealing

The final task involved evaluating the changes in the mechanical properties during annealing. It is not feasible to study every system snapshot along the thermal profile (there are thousands) using the method described in Chapter 3 to evaluate mechanical properties. I therefore chose 11 structures equally spaced along the thermal profile for evaluation. In each case, I explored the mechanical stability of the structure that resulted from simulated thermal annealing to a given temperature. Due to the limited number of structures studied, I was able to manually determine the identity of the atoms that constitute the main system "bulk" by visual inspection.

For each chosen structural snapshot, I evaluated the elastic constants C_{11} and C_{12} by compressing the material in one direction and then measuring the resulting changes in stress using the LAMMPS-generated pressure tensor. [50] I then used these constants to estimate the bulk and Young's moduli at each point.

The results (Figure 39) suggest that the mechanical properties are initially fairly stable before thermal annealing (C_{11}=6GPa). The elastic constants then drop to very low levels (C_{11} between 0 and 1 GPa) until the material passes through the glass transition (around 1100°C). Above Tg, the values increase to more reasonable levels (C_{11} between 6 and 12 GPa). The initial apparent drop in mechanical properties may, however, be misleading, and the first data point may simply be improperly annealed relative to the heated data points. Further testing of this point should be conducted in future. The overall results would agree with the apparent densification seen in the material at these temperatures. It should be recognized, however, that the LAMMPS pressure measurements upon which these calculations are based are very imprecise, and so the exact precision and accuracy of these values is unknown. The results reveal

a distinct increase in the material moduli past the glass transition temperature, but any conclusions beyond this are difficult to quantify. Future studies of this material should investigate alternate methods of mechanical property verification.

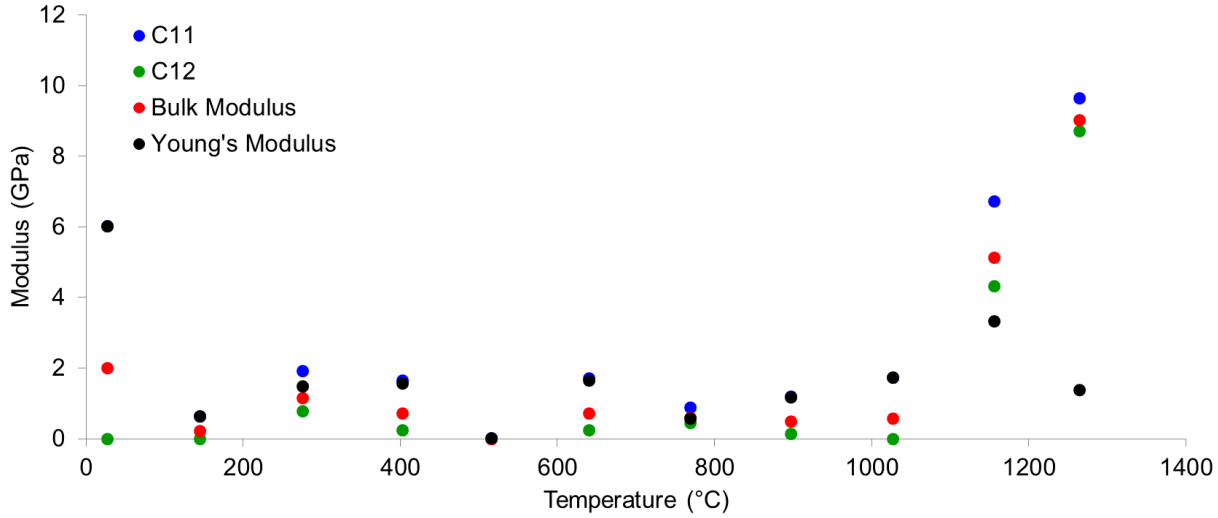

Figure 39. Change in mechanical properties in the SiCOH material as a function of annealing temperature. The properties start out initially at reasonable levels (Young's moduli of 6 GPa); however, the simulated thermal annealing causes the calculated elastic response to immediately weaken. The moduli do pick back up again, however, after passing through the glass transition temperature at 1100°C.

Conclusions

In this study, I was able to successfully demonstrate and quantify the nature of bonding changes that occur in a ULK SiCOH system upon rapid thermal annealing. Both Molecular Dynamics simulations using a reactive force field and experimental laser annealing studies show the same structural changes occurring in the same order relative to temperature. Organic components of the SiCOH material decompose and leave the system rather than recombining into the underlying silicon-oxygen framework. Following this loss of organic material, the second thermally induced transition is an increased networking of the silicon-oxygen framework. This second transition occurs about 150-200°C after the loss of organic moieties in both experiments and simulations. The increased Si-O networking will likely result in densification of the material and it will therefore be difficult to improve the mechanical properties of the material prior to pore collapse and subsequent *k* increase.

To verify this prediction, I studied the densification, change in dielectric constant, and change in mechanical properties of the material during the simulated rapid thermal annealing process. The material porosity was shown to decrease at the same point the Si-O networking begins to significantly increase. The dielectric constant remains relatively stable until this point is reached as well. This suggests that under rapid thermal annealing conditions, the porosity and therefore dielectric constant of the material are stable until the material reaches 900°C. Mechanical properties were not shown to improve, however, until temperatures exceeded Tg, at 1100°C. More experimental verification is necessary to determine the exact nature of the mechanical property changes.

CHAPTER 5

A POTENTIAL NEW CLASS OF LOW-K MATERIALS: POROUS ORGANIC POLYMERS (POPs)

The studies of SiCOH materials have provided many insights into the relationships between material structure and the resulting dielectric and mechanical properties. As the semiconductor industry looks to the future of low-k materials, it will also be necessary to consider new candidate materials, both in the realm of SiCOH materials containing as-yet unexplored structural units, and beyond the SiCOH class of materials.

One of the key findings of the simulation work is that the inherent porosity of the material plays a critical role in driving down the dielectric constant. Arguably, the porosity is the single most important variable in determining low-k characteristics of materials. This suggests that structural motifs which beneficially improve the film's performance will be those which:

1) do not dramatically (or significantly) increase the polarizability of the SiCOH film,
2) promote porosity and
3) provide improved mechanically stability,.

This was shown in previous studies of the differences between Si-CH_2-Si and Si-CH_3 bonding structures, which suggested that, while both units have similar polarizabilities, Si-CH_2-Si structures add greatly to film mechanical stability as compared to Si-CH_3 structures. It is difficult, however, to maintain Si-CH_2-Si bonding in porous structures. This suggests that a larger organic unit may be more inclined to incorporate into the underlying Si-O film framework, beneficially improving the mechanical strength while negligibly affecting the material's

polarizability. If this unit could also be used to frustrate packing and promote porosity, the material performance might be improved still further.

Thus the hypothesis for potential replacements for SiCOH materials is to look for materials with the following characteristics [3, 7-8]:

1. Nanoporosity (average pore sizes below 2 nm in diameter)
2. Larger carbon-based moieties
3. Structural motifs that frustrate packing, *e.g.,* those facilitating jamming transitions.

With this hypothesis in mind, I decided to test the influence of carbon-based ring structures on the polarizability of a SiCOH film.

Polarizability of Ringed Structures

In order to predict new low-k material possibilities, some groundwork was needed to quickly rule out (or in) whole "classes" of organic motifs based on their inherent polarizability contributions. To this end, I analyzed the polarizabilities of different classes of aromatic and hydrogenated carbon rings, as described in Figures 40 and 41. I started with "interconnected" polycyclic hydrocarbons, and then studied "linked" phenylenes. I then compared these polarizabilities to those of SiCOH motifs, focusing specifically on the overall rate of polarizability increase with the addition of equivalent numbers of atoms.

The results confirm that, as expected, the π-bonding characteristic of aromatic rings is highly polarizable. This contributes to a rate of polarizability increase much higher than that of SiCOH materials, as shown in Figure 42. In contrast, (non-aromatic) cyclohexanes exhibited lower polarizabilities and low rates of polarizability increase with increasing numbers of atoms, which suggests that these units are more promising candidates than their aromatic counterparts, as shown in Figure 42. I then incorporated these cyclohexane units into small Si-O based motifs,

to study their interactions with silicon and oxygen atoms. As shown in Figure 42, the rate of polarizability increase as a result of introducing ringed structures into the Si-O motifs is essentially identical to the influence of Si-CH_3 motifs. I hypothesize that a material built upon such cyclic motifs could create porous space through frustrated packing, while –at the same time- maintaining reasonable mechanical stability through the inherent strength of the ring structures.

This hypothesis about the inherent porosity and mechanical integrity of cyclic organic materials led to the consideration of a new class of materials called "porous organic polymers" or "POPs." These are similar in nature to covalent organic framework (COF) materials, except for the amorphous character of the POPs. Both POP and COF materials are composed of covalently bonded "linker" and "connector" fragments, which chemically react in solution to form ordered networks with inherent nanoscale porosities. [92] In order to get a sense of whether or not these materials may exhibit a reasonable polarizability, I investigated several structural motifs that are inherent to the make-up of both COF and common POP materials. Figure 43 shows the motifs tested based on common COF structures. These are based on boron-oxygen rings connected by aromatic rings. Figure 45 shows motifs tested based on common POP connectors and linkers. These are based on varying numbers of aromatic rings.

The results shown in Figure 44 and 46 indicate that, while those structures which are highly aromatic have high intrinsic polarizabilities, similar materials with lower aromatic character have polarizabilities which are comparable to those of SiCOH motifs. Combined with the additional benefit of having high porosities, it is likely that these materials will have favorable dielectric and mechanical properties for low-k interconnect applications. All organic materials are unfavorable for these applications because of their low etch-resistance, so it will

also be important to be able to incorporate stabilizing materials into these structures, like silicon or boron atoms.

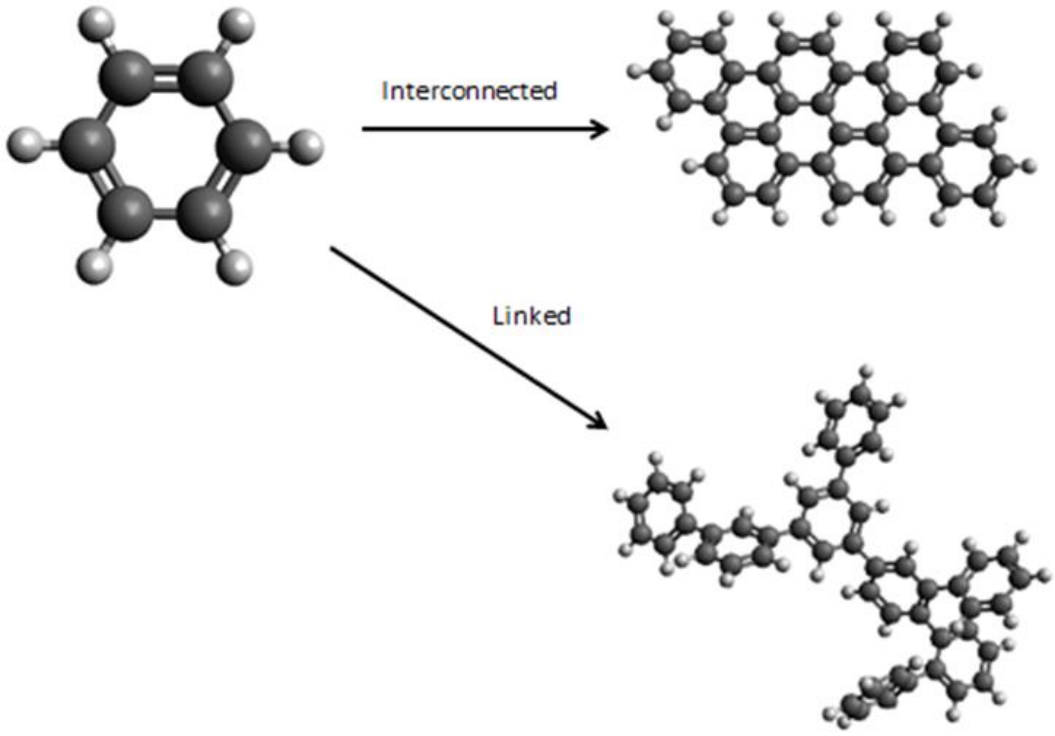

Figure 40. The definition of "interconnect" aromatics, *i.e.*, those moieties that are bonded to one another through multiple carbon atoms to create one flat sheet, and "linked" aromatics, *i.e.*, those that are bonded only at one ring site, rather than multiple sites.

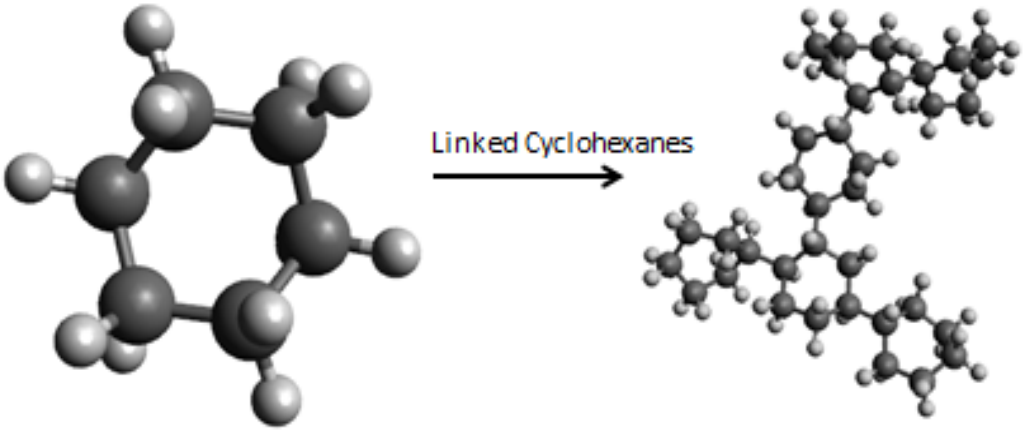

Figure 41. Hydrogenated carbon ring structures (cyclohexanes) were linked through carbon-carbon bonds, linking only at one carbon site per ring to create a branching chain of rings, rather than an interconnected, more rigid surface.

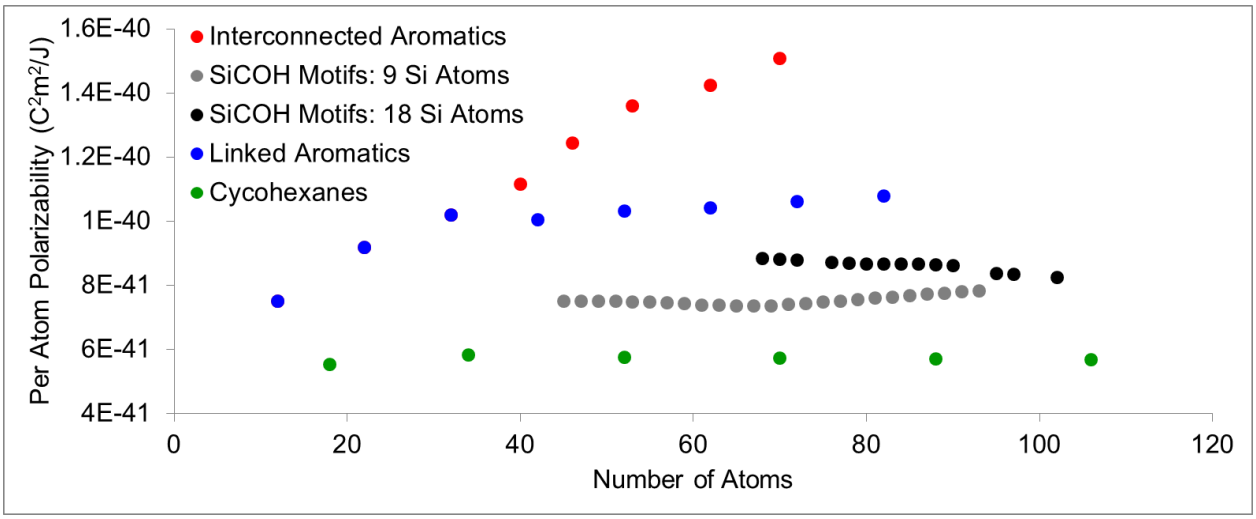

Figure 42. Polarizability *versus* the number of atoms in motifs representing different ring-based organic structural moieties. Most motifs maintain a constant per-atom polarizability regardless of the number of atoms present in the motif. Interconnected aromatics, however, (polycyclic hydrocarbons), actually increase their per-atom-polarizability as more rings are added. This suggests that additional aromatic rings further delocalize the electrons associated with the material. Linked aromatics do not show this behavior, although their polarizabilities do not compare favorably with SiCOH motifs. Cyclohexanes, which do not have the π-bonding feature of aromatics, have a much lower polarizability, even lower than traditional SiCOH materials. Such motifs could offer a more encouraging route for future low-k materials development.

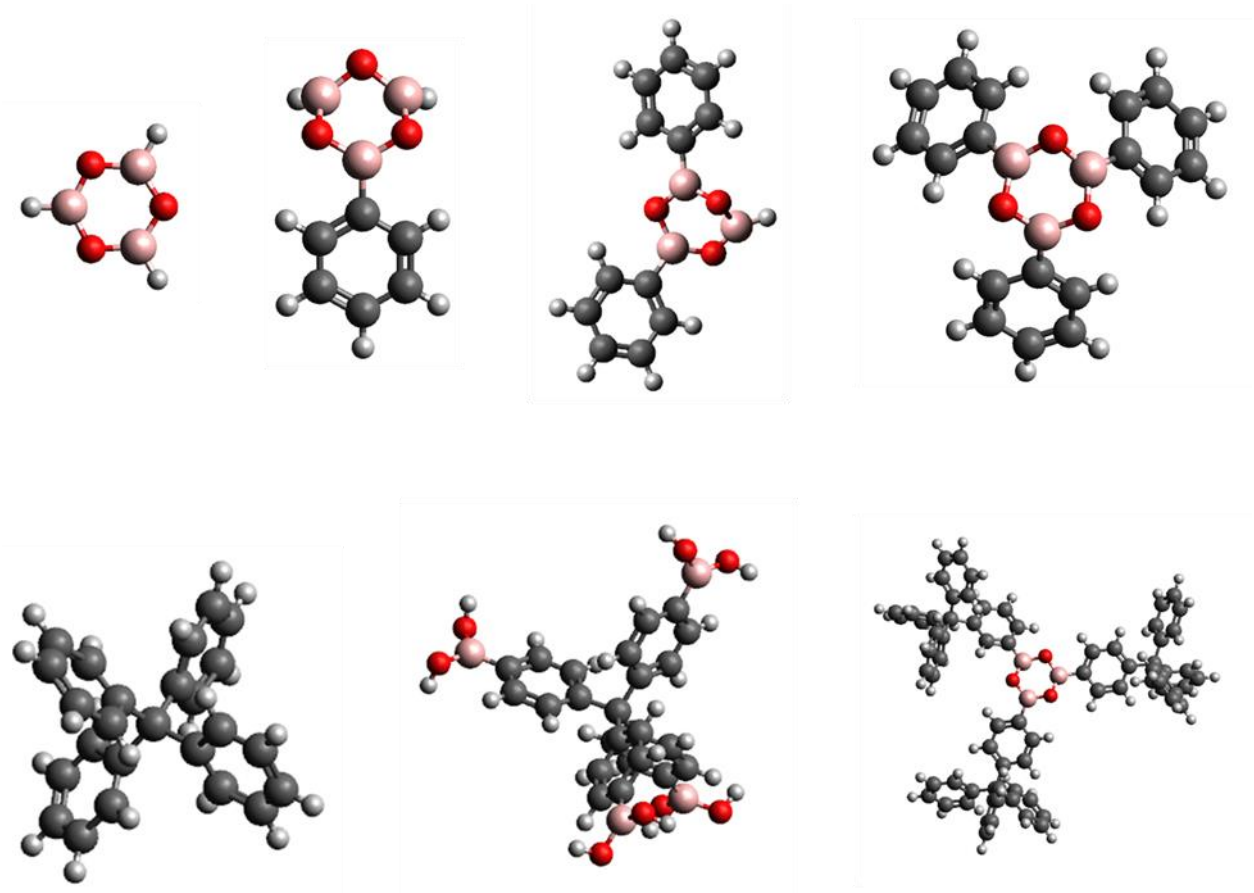

Figure 43. Boron-oxygen-based COF motifs tested to study intrinsic polarizabilities. Boron shown in pink, carbon in gray, hydrogen in white, and oxygen in red. Beginning with the boron-oxygen ring shown in the upper left, aromatic rings were added to study the interaction between the aromatics and the boron-oxygen ring. A complex four-ringed aromatic connector molecule was then analyzed both separately and in conjunction with boron atoms and a boron-oxygen ring.

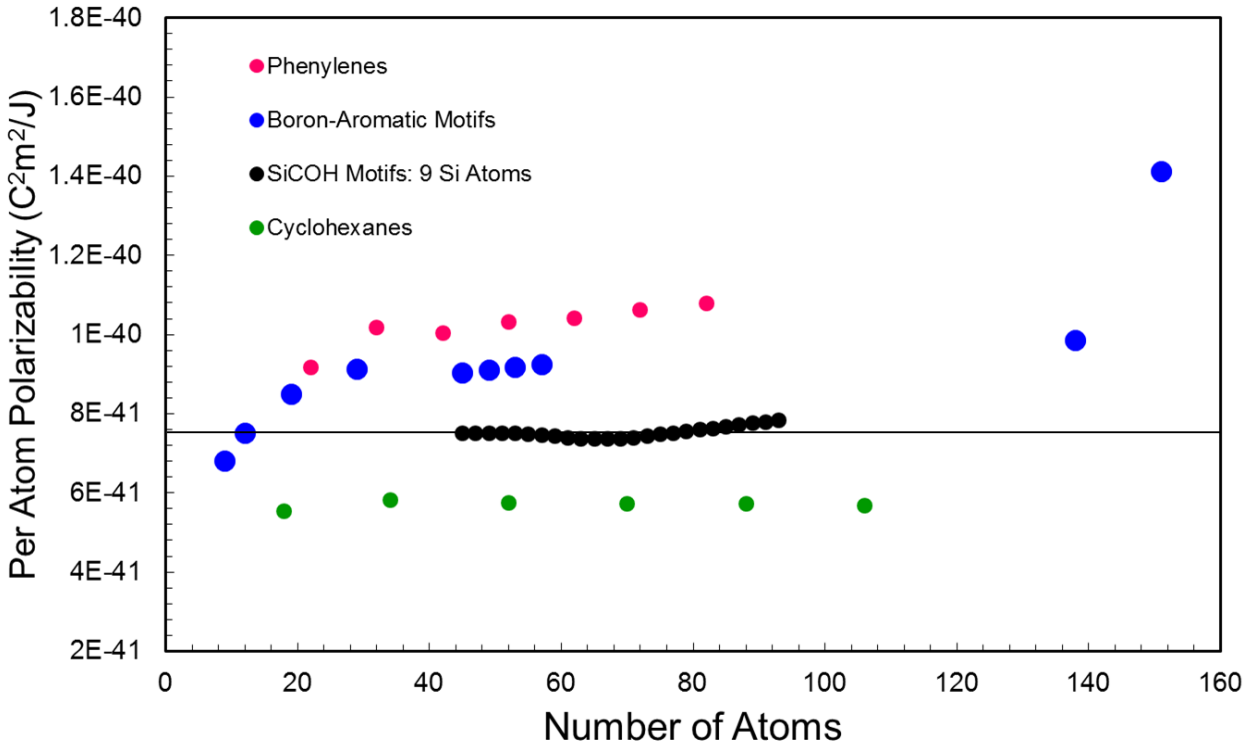

Figure 44. Polarizabilities of boron-oxygen based motifs in comparison with phenylenes, SiCOH motifs, and cyclohexanes. Motifs based only on boron-oxygen rings compare favorably to SiCOH motifs, as shown in blue on the far left. As the aromatic character of the motifs increases the motifs approach the polarizabilities of phenylenes. When the aromatic character becomes very high, as shown on the far right, the per-atom polarizability far exceeds that of the phenylenes. This suggests that boron-oxygen based motifs would be favorable if the aromatic character of the compound could be kept to a minimum.

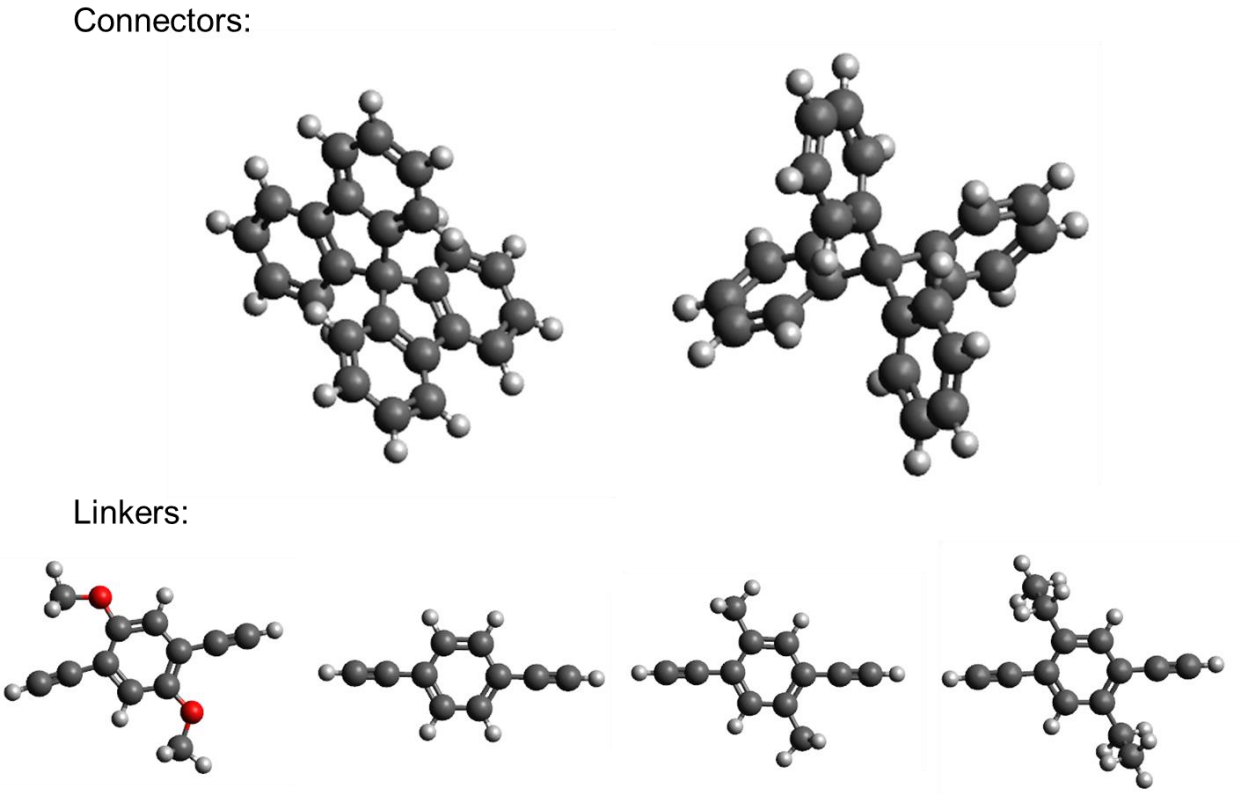

Figure 45. Common POP connectors and linkers. The connectors have four connection points (one on each of the outer aromatic rings), while the linkers have two connection points (on either side of the triple bonds). Carbon atoms are shown in gray, hydrogen atoms in white, and oxygen atoms in red.

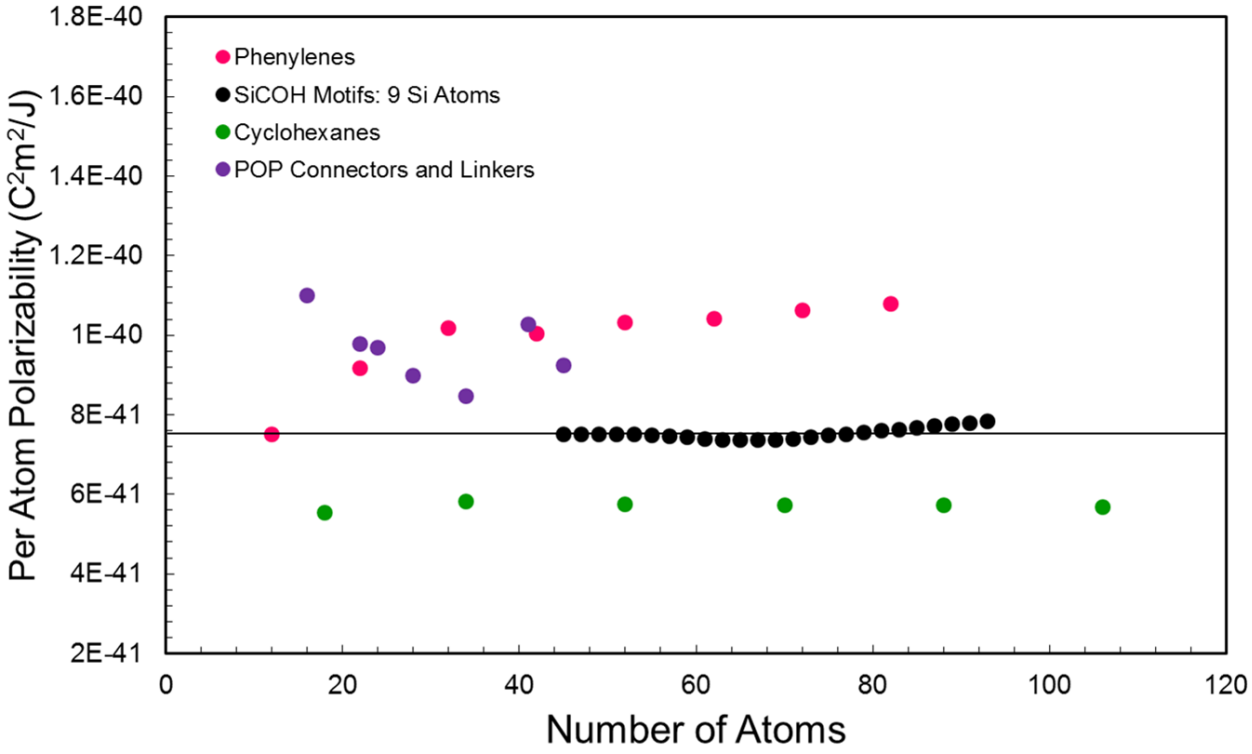

Figure 46. Polarizabilities of common POP connectors and linkers as compared to the per-atom polarizabilities of phenylenes, SiCOH motifs, and cyclohexanes. The POP motifs do not display the linear trend exhibited by the other motifs; this is likely to be due to the very similar compositions of the different motifs. The linker molecules are also very asymmetrical in nature which may skew their polarizability values. Clearly, the aromatic nature of the molecules places them in line with the polarizabilities of phenylenes. If the frameworks are highly porous, however, it is possible for the overall dielectric constant to still achieve a low value.

Simulations of a Prototype POP Molecule

The study of POP materials began with the simple test case of a POP based on one molecule acting as both the "connector" and the "linker". This molecule, shown in Figure 47, has been termed the "triforce" molecule because of its three-fold symmetry around the central ring. It can exist in both a fully aromatic form pictured on the left-hand side of Figure 47, and a hydrogenated form pictured on the right-hand side of Figure 47.

The polarizability of this molecule in its aromatic form is relatively high and generally unfavorable, as shown in Figure 48; however, its hydrogenated form compares favorably with SiCOH motifs. This, combined with its anticipated high intrinsic porosity, should make its dielectric properties very favorable for ULK applications.

I simulated the molecule by randomly rotating and translating it throughout a simulation box, and then annealing the material at low temperatures (100°C) in an NVT molecular dynamics simulation. I initially attempted to use the OPLS force field for this study, but found that the dihedral terms produced an unstable representation of the molecule. Instead, I used the REAX force field to simulate the molecule and found that it maintained the molecule shape both in isolation and in the presence of other triforce molecules. This force field also promotes more stable bonding between the triforce molecules.

Figure 49 shows the initial set-up of randomly distributed molecules as well as the post-annealed network that forms. While this network does not appear to have any large pores (>1 nm in diameter), upon closer inspection, it does appear to have a high number of very small pores, as shown in the pore size distribution in Figure 50. I estimated the overall porosity of this structure, using the previously described algorithm (Chapter 1), to be around 20%. Further, I used the calculation of the polarizability of the triforce molecule (Figure 48) with the Clausius-Mossotti

equation (Equation 1), to obtain an estimate for the dielectric constant of this network. Despite the lack of large pores, I found the estimate of the k to be 1.8, which is below the desired goal of 2.0. This promising result suggests that the consistent distribution of small pores throughout the material may be the best route to identifying a material with strong mechanical stability and a low dielectric constant.

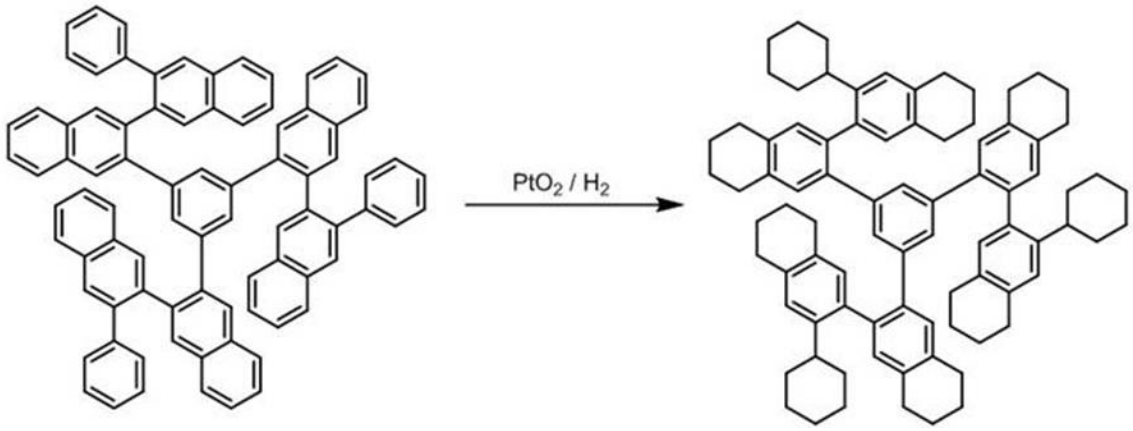

Figure 47. A test case small molecule candidate that could be used to make a porous organic polymer. The molecule has been called the "triforce" molecule because of its three-fold symmetry around the central aromatic ring. The form on the left hand side is fully aromatic and has an unfavorably high polarizability; however, it can be hydrogenated to make the molecule on the right which has a much more favorable polarizability.

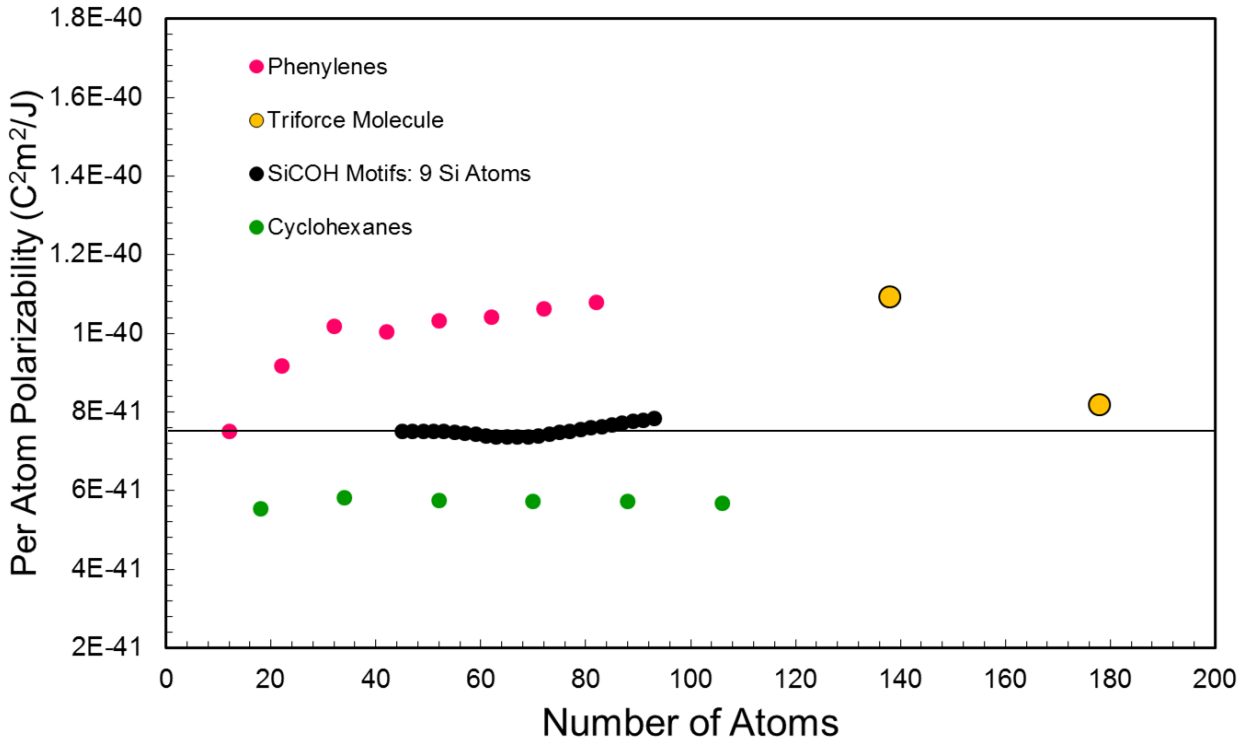

Figure 48. Polarizability of the triforce molecule as compared to SiCOH motifs, phenylenes, and cyclohexanes. The aromatic form of the molecule is the form of the molecule corresponding to about 140 atoms. This molecule has polarizabilities similar to phenylenes, and has a higher polarizability than SiCOH motifs. The hydrogenated form of the molecule on the right, corresponding to a motif containing about 180 atoms, compares favorably with traditional SiCOH motifs, although it does not approach the low polarizabilities of the cyclohexanes.

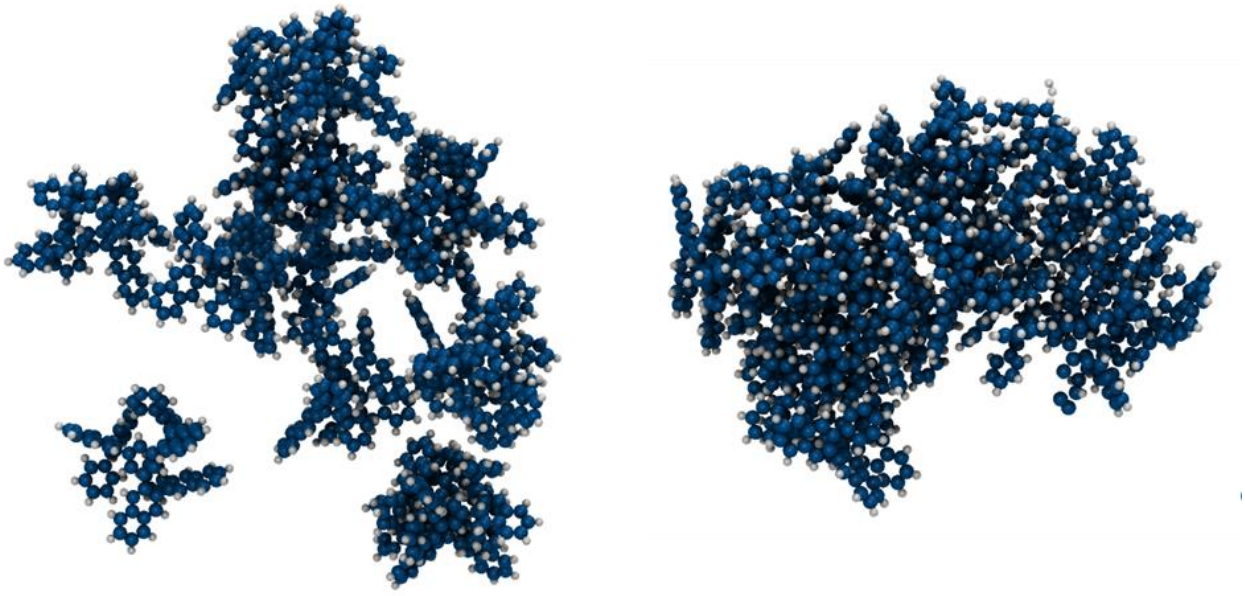

Figure 49. The left hand image shows the randomly distributed triforce molecules prior to simulated annealing. The image on the right shows the result after relaxation. Carbon atoms are shown in blue, and hydrogen atoms in white. While there are no obvious large pores present in the film, the regular distribution of small pores create favorable dielectric properties.

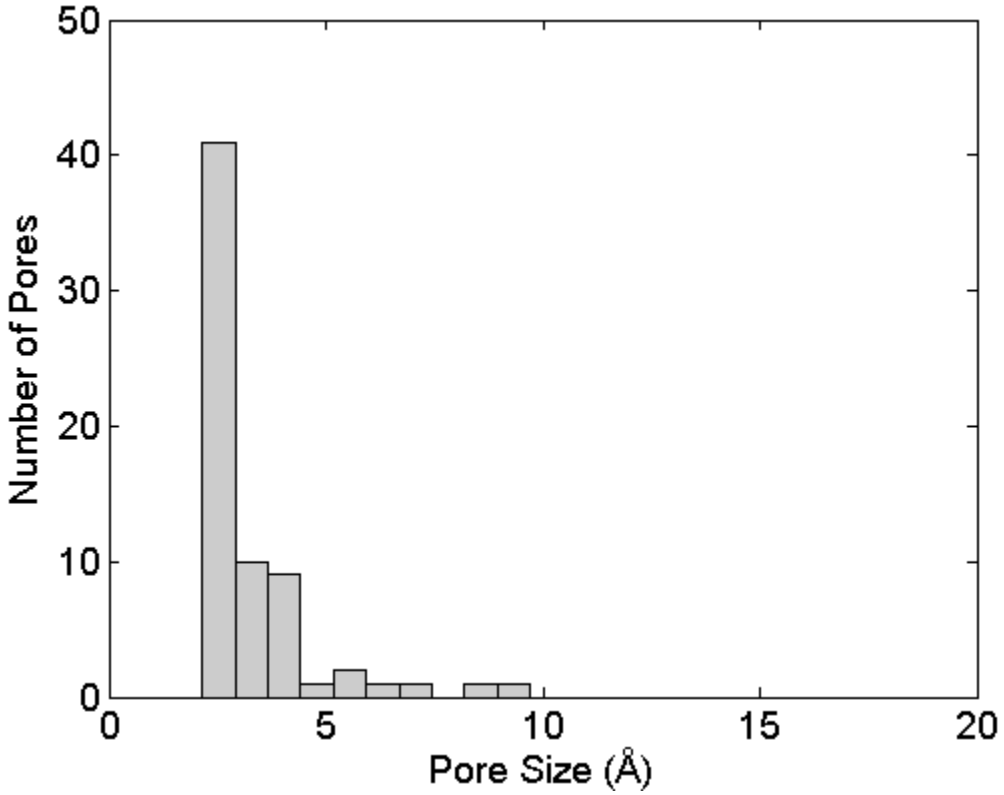

Figure 50. Pores size distribution of the relaxed network of triforce molecules. While there are no large pores present in the film, the large number of small pores is sufficient to create a low overall dielectric constant.

Creation of a POP Structure Generation Code

In order to study these amorphous POP materials further, I expanded upon the existing structure generation algorithm to allow for the development of atomic-scale models of the structure of POP materials. As described previously, the existing structure generation algorithm is based on systems composed of 'four-connecting' silicon atoms and 'two-connecting' oxygen atoms. As shown in Figure 45, the most common linkers and connectors currently used to make POP materials are also based on four-connecting and two-connecting motifs. The goal of the new code was, therefore, to expand the point-based silicon and oxygen connections into center-points which would define the locations of the POP motifs. This is by no means the only, or perhaps even "the best" way to simulate POP materials. An alternative would be to course-grain the connectors and linkers and let them settle naturally in simulation before attempting to cross-link them together, as has been described in literature. [93] I was interested, however, in whether or not the previously developed algorithm could be expanded to encompass new areas.

There were a number of challenges associated with modifying the existing code. The original SiCOH structure generation code outlines a grid based on points which are connected four other points. The distances between these points are approximately 3Å, or two Si-O bonds apart. The new code needs to fit whatever motifs are being substituted into those points, so the spacing now needs to be the size of one full 'four-connector' motif plus one full 'two-connector' motif. The code, therefore, needs to be able to read in xyz data describing the motifs being substituted, and resize the grid accordingly. I begin by generating a starting grid of four-coordinated points, and then read in the xyz coordinate data for the connector and linker molecules being used for the given system set-up. The grid is then resized based on the

dimensions of these molecules, so that each molecule will have enough space to lie on its assigned grid-point, without overlapping a neighboring molecule.

When the "four-connecting" connector molecules are placed at each point in the system grid, they need to be randomly rotated before being translated in place, to avoid creating a more crystalline structure. The more difficult rotation that needs to be performed is associated with the placement of the "two-connecting" linker molecules. Because the linker molecules, as shown previously in Figure 45, are two-connecting, they are linear in orientation. They therefore need to be rotated so that their central axis aligns with the axis of the two connector molecules they are meant to be linking. For example, if the linker is initially lying along the x-axis, and it needs to link a pair of connectors lying along the z-axis, it needs to be rotated appropriately. Therefore, before the linkers are introduced between neighboring connector molecules, a list of each connector's orientation to its neighbors needs to be generated, and all linker molecules need to be appropriately rotated. This is shown schematically in Figure 51. An example of a resulting starting configuration is shown in Figure 52.

The promising study of the triforce molecule described previously suggests that these materials should have a large number of pores and promising dielectric properties. Future efforts will focus on Molecular Dynamics simulations of these materials. I attempted to model these materials using the REAX force field, as was successfully done in the case of the triforce molecules. However, because the force field is less adept at bond-forming, as compared to bond-breaking, the simulations ultimately resulted in an unstructured final state. A more traditional force field, like OPLS, is likely to be more suitable to describe these materials.

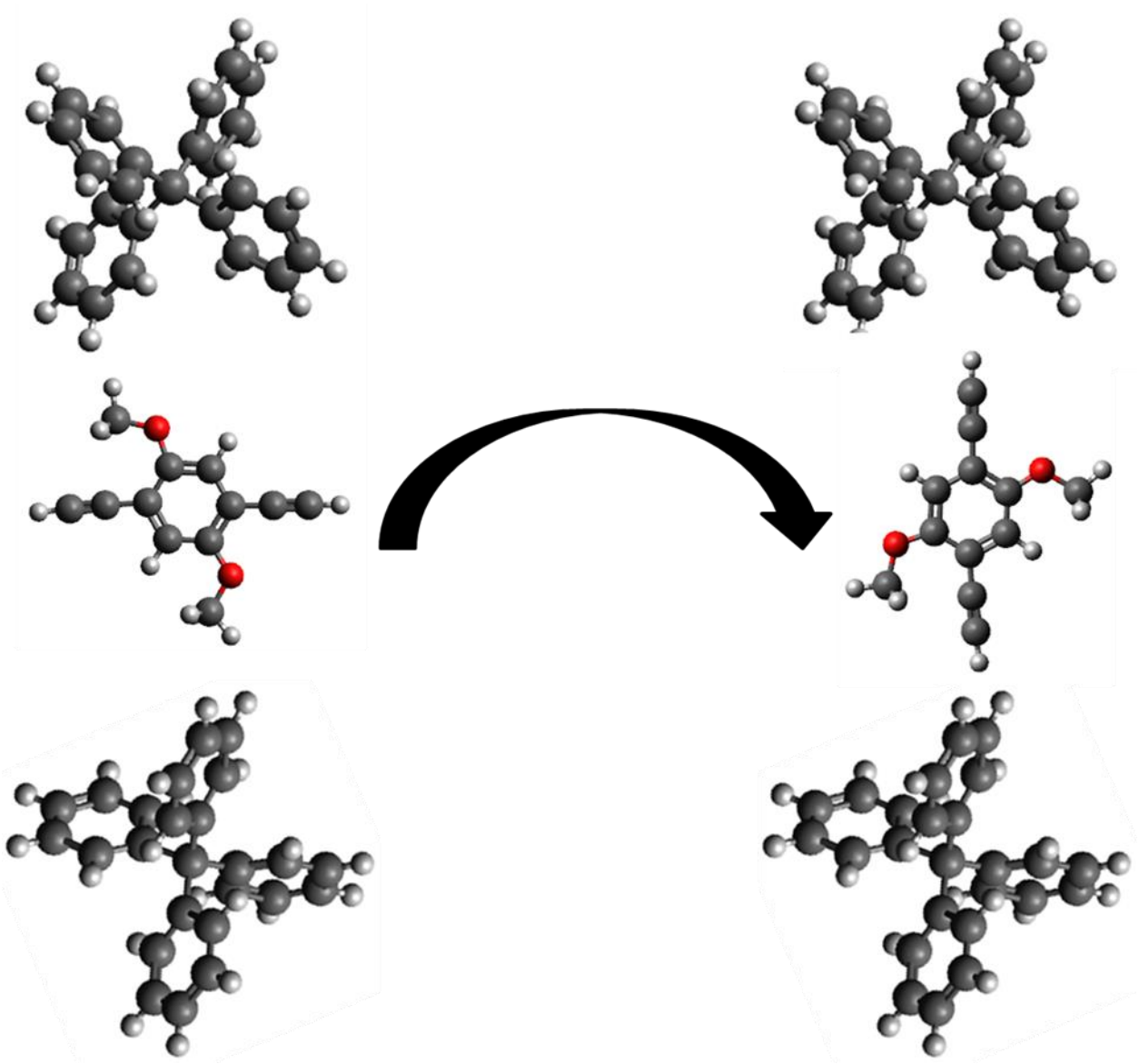

Figure 51. Schematic representation of POP code rotations. First, each four-connector is randomly rotated around its central point before being translated into place on the grid. The four molecules shown in each corner above are all identical, but are rotated differently. The linker molecules are linear in orientation and need to be rotated to align with the appropriate connector molecules. In the example above, the linker molecule is originally placed so that its connecting ends are parallel to the two connectors that it is meant to link together. Therefore, it needs to be rotated 90°, as shown on the right hand side of the schematic.

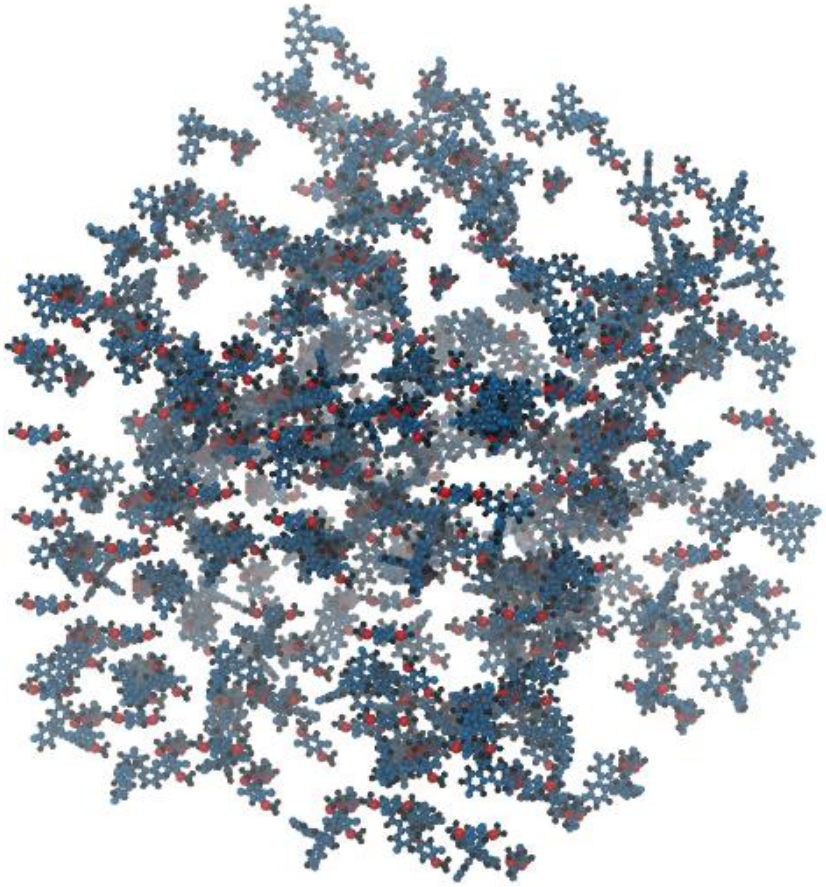

Figure 52. Sample starting layout of a POP material. The connectors and linkers are all laid out on a grid initially and the individual molecules are clearly visible throughout. Carbon atoms are shown in blue, hydrogen atoms in black, and oxygen atoms in red.

Conclusions

Overall, the studies of the polarizabilities of ringed structures suggest that aromatic compounds have higher polarizabilities than SiCOH motifs, and would therefore be unlikely to have favorable dielectric properties. It is possible, however to find a balance between aromatic character, hydrogenated cycloalkane structures, and high porosity, to reach favorable dielectric estimates. Both COF and POP motifs were shown to have polarizabilities that, while slightly higher than SiCOH motifs, are not so high as to be unusable as a viable alternative to SiCOH.

The simulation of a POP material based on "triforce" molecules indicated that the large number of small pores spread throughout the material created a favorable dielectric environment. I estimate that such a structure would have a dielectric constant below the desired threshold of 2.0. I also modified the original structure generation algorithm for SiCOH materials, to make it more agile and capable of laying out a POP framework. Future efforts will focus on creating working simulations of these materials to better understand their behavior and properties.

CHAPTER 6

CONCLUSIONS AND FUTURE WORK

Overall, this study has been successful in providing understanding of structure-property relationships in ULK materials. This model of SiCOH materials is the first computational study to simultaneously investigate the links between the underlying framework of the SiCOH material, the system porosity and pore size distribution, the dielectric constant, and the material's mechanical integrity. I showed that while porosity is the largest driving force behind obtaining a low dielectric constant, the amount of cross-linking throughout the film is the biggest contribution to the mechanical stability of the material.

I also simulated rapid thermal annealing of the material and observed the changes in system structure, porosity, dielectric constant, and elastic moduli induced by this thermal annealing. The use of the REAX force field to study structural and compositional changes in the film was very successful, and agreed well with complimentary laser annealing experiments. I identified a potential processing window between 700-900°C, where the unstable organic fragments of the film have left the material, but the Si-O networking has yet to dramatically increase. I found that the porosity and dielectric constant are both indeed stable to 900°C. At higher temperatures the film begins to densify and the dielectric constant increases as a result. The mechanical properties, however, are not shown to improve until after the system has passed through Tg (1100°C).

Using the intuition I had garnered during the study of SiCOH materials, I also endeavored to identify potential new classes of low-k materials. I learned from the development of a SiCOH model, that porosity drives favorable dielectric properties, while cross-linking drives

strong mechanical properties. I therefore looked at materials with frustrated packing and large functional groups that would be intrinsically porous but highly networked. I focused particularly on organic ring structures, due to their bulky size but high stability. Studying the polarizabilities of these structures suggested that aromatic compounds may be too highly polarizable, but with hydrogenation can have reasonable dielectric properties. POP materials were identified as being a potential class of new low-k materials, and it was shown that the regular number of small pores present in these polymers creates a favorable dielectric environment.

Going forward, stable simulations of these POP materials will give more insight into their structural stability and porous nature. These materials may have potential not only as future low-k materials, but also as materials used to detect explosives. [94] After successfully simulating a POP structure, proceeding to simulate the interaction of suitably functionalized molecules could allow it to sense explosive materials (like TNT) using the POP structure as a highly sensitive sensor, may help advance this field as well.

In order to be useful as a low-k material, the all-organic nature of the POP materials will need to be modified, as organic materials are generally degraded during the electronic device manufacturing process. Simulating and studying ways of incorporating silicon content into the polymer, for example, may be key to transitioning POP materials from the point of having intriguing properties, to being a strong low-k candidate material.

REFERENCES

[1] G. E. Moore, "Cramming more components onto integrated circuits," *Electronics*, vol. 38, no. 8, pp. 114-117, 19 April 1965.

[2] R. D. Miller, "In Search of Low-k Dielectrics," *Science*, vol. 286, no. 5439, pp. 421-423, 15 October 1999.

[3] C. L. Borst, W. N. Gill and R. J. Gutmann, "Overview of IC Interconnects: Organosilicate GLasses," in *Chemical-Mechanical Polishing of Low Dielectric Constant Polymers and Organosilicate Glasses: Fundamental Mechanisms and Application to IC Interconnect Technology*, Kluwer Academic Publishers, 2002, p. 9.

[4] J. Gambino, F. Chen and J. He, "Copper Interconnect Technology for the 32 nm Node and Beyond," in *IEEE 2009 Custom Integrated Circuts Conference (CICC)*, 2009.

[5] "Interconnect Summary," in *International Technology Roadmap for Semiconductors*, 2013.

[6] "International Technology Roadmap for Semiconductors, Interconnects," 2009.

[7] W. Volksen, R. D. Miller and G. Dubois, "Low Dielectric Constant Materials," *Chemical Reviews*, vol. 110, no. 1, pp. 77-80, 2010.

[8] A. Grill, S. M. Gates, T. E. Ryan, S. V. Nguyen and D. Priyadarshini, "Progress in the development and understanding of advanced low k and ultralow k dielectrics for very large-scale integrated interconnects - State of the art," *Appl. Phys. Rev.*, vol. 1, p. 011306, 2014.

[9] W. Volksen, G. Dubois, A. Kellock, T. P. Magbitang, R. D. Miller, D. Miller, S. Cohen, E. E. Simonyi, L. Ramirez, D. Markle, S. Chen, S. Zhou, X. Wang and Y. Wang, "Mechanical Enhancement of Low-k Organosilicates by Laser Spike Annealing," *Journal of The Electrochemical Society*, vol. 155, pp. G224-G230, 2008.

[10] W. Volksen, G. Dubois, A. Kellock, T. P. Magbitang, R. D. Miller, S. Cohen, E. E. Simonyi, L. Ramirez and Y. Wang, "Laser Spike Annealing: A Novel Post-Porosity Treatment for Significant Toughening of Low-k Organosilicates," in *IEEE Proceedings of the Interconnect Tech. Conf.*, Burlingame, California, 2006.

[11] S. Lee, J. Yang, S. Yeo, J. Lee, D. Jung, J.-h. Boo, H. Kim and H. Chae, "Effect of Annealing Temperature on Dielectric Constant and Bonding Structure of Low-k SiCOH Thin Films Deposited by Plasma Enhanced Chemical Vapor Deposition," *Japanese*

Journal of Applied Physics, vol. 46, pp. 536-541, 2007.

[12] C. S. Yang, Y. H. Yu, K.-M. Lee, H.-J. Lee and C. K. Choi, "Investigation of low dielectric carbon-doped silicon oxide films prepared by PECVD using methyltrimethoxysilane precursor," *Thin Solid Films,* vol. 506, pp. 50-54, 2006.

[13] J. S. Rathore, L. V. Interrante and G. Dubois, "Ultra Low-k Films Derived from Hyperbranced Polycarbosilanes (HBPCS)," *Advanced Functional Materials,* vol. 18, pp. 4022-4028, 2008.

[14] J.-M. Park, J. K. Choi, C. J. An, M. L. Jin, S. Kang, J. Yun, B.-S. Kong and H.-T. Jung, "Nanoporous SiCOH/CxHy dual phase films with an ultralow dielectric constant and a high Young's modulus," *Journal of Materials Chemistry C,* vol. 1, pp. 3414-3420, 2013.

[15] S. Yasuhara, T. Sasaki, T. Shimayama, K. Tajima, H. Yano, S. Kadomura, M. Yashimaru, N. Matsunaga and S. Samukawa, "Super-low-k SiOCH film (k=1.9) with extremely high water resistance and thermal stability formed by neutral-beam-enhanced CVD," *Journal of Physics D: Applied Physics,* vol. 43, pp. 065203.1-065203.8, 29 January 2010.

[16] F. Iacopi, Y. Travaly, B. Eyckens, C. Waldfried, T. Abell, E. P. Guyer, D. M. Gage, R. H. Dauskardt, T. Sajavaara, K. Houthoofd, P. Grobet, P. Jacobs and K. Maex, "Short-ranged structural rearrangement and enhancement of mechanical properties of oganosilicate glasses induced by ultraviolet radiation," *Journal of Applied Physics,* vol. 99, no. 053511, pp. 1-7, 8 March 2006.

[17] H.-J. Lee, C. L. Soles, D.-W. Liu, B. J. Bauer, E. K. Lin and W.-l. Wu, "Structural characterization of porous low-k thin films prepared by different techniques using x-ray porosimetry," *Journal of Applied Physics,* vol. 95, no. 5, pp. 2355-2359, 1 March 2004.

[18] H. Li, J. M. Knaup, E. Kaxiras and J. J. Vlassak, "Stiffening of organosilicate glasses by organic cross-linking," *Acta Materialia,* vol. 59, pp. 44-52, 2011.

[19] C. S. Yang and C. K. Choi, "Mechanical property of the low dielectric carbon doped silicon oxide thin film grown from MTMS/O2 source," *Current Applied Physics,* vol. 6, pp. 243-247, 2006.

[20] S.-I. Nakao, J. Ushio, T. Ohno, T. Hamada, Y. Kamigaki, M. Kato, K. Yoneda, S. Kondo and N. Kobayasi, "UV/EB Cure Mechanism for Porous PECVD/SOD Low-k SiCOH Materials," in *IEEE International Interconnect Technology Conference,* San Francisco, 2006.

[21] G. Aksenov, D. De Roest, P. Verdonck, F. N. Dultsev, P. Marsik, D. Shamiryan, H. Arai, N. Takamure and M. R. Baklanov, "Optimization of low-k UV curing: effect of wavelength on critical properties of the dielectric," 2009.

[22] T. Yoda, K. Fugita, H. Miyajima, R. Nakata, N. Miyashita and N. Hayasaka, "Properties of High-Performance Porous SiCOH Low-k Film Fabricated Using Electron-Beam Curing," *Japanese Journal of Applied Physics*, vol. 44, p. 3872, 2005.

[23] N. Tajima, T. Ohno, T. Hamada, K. Yoneda, N. Kobayashi, S. Hasaka and M. Inoue, "Molecular modeling of low-k films of carbon-doped silicon oxides for theoretical investigations of the mechanical and dielectric propoerties," *American Institute of Physics*, vol. 89, no. 061907, pp. 1-3, 2006.

[24] N. Tajima, T. Ohno, T. Hamada, K. Yoneda, S. Kondo, N. Kobayashi, M. Shinriki, Y. Inaishi, K. Miyazawa, K. Sakota, S. Hasaka and M. Inoue, "Carbon-Doped Silicon Oxide Films with Hydrocarbon Network Bonds for Low-k Dielectrics: Theoertical Investigations," *Japanese Journal of Applied Physics*, vol. 46, no. 9A, pp. 5970-5974, 2007.

[25] C. A. Yuan, O. van der Sluis, G. Q. Zhang, L. J. Ernst, W. D. van Driel, R. B. van Silfhout and B. J. Thijsse, "Chemical-mechanical relationship of amorphous/porous low-dielectric film materials," *Computational Materials Science*, vol. 42, pp. 606-613, 2008.

[26] C. A. Yuan, O. van der Sluis, G. Q. Zhang, L. J. Ernst, W. D. van Driel and R. B. R. van Silfhout, "Molecular simulation on the material/interfacial strength of the low-dielectric materials," *Microelectronics Reliability*, vol. 47, pp. 1483-1491, 4 September 2007.

[27] J. M. Knaup, H. Li, J. J. Vlassak and E. Kaxiras, "Bottom-up Modeling of the Elastic Properties of Organosilicate Glasses and their Relation to Composition and Network Defects," in *Materials Research Society Symposium Proceedings Vol. 1297*, 2011.

[28] P. Kroll, "Modelling and simulation of amorphous silicon oxycarbide," *Journal of Materials Chemistry*, vol. 13, pp. 1657-1668, 14 May 2003.

[29] M. S. Oliver, G. Dubois, M. Sherwood, D. M. Gage and R. H. Dauskardt, "Molecular Origins of the Mechanical Behavior of Hybrid Glasses," *Advanced Functional Materials*, vol. 20, pp. 2884-2892, 2010.

[30] Y. Shioya, T. Ohdaira, R. Suzuki, Y. Seino and K. Omote, "Effect of UV Wavelength on the hardening process of porogen-containing and porogen-free ultralow-k plasma-enhanced chemical vapor deposition dielectrics," *Journal of Vacuum Science and*

Technology B, vol. 29, p. 032201, 2011.

[31] J. Ushio, T. Hamada, T. Ohno, S.-I. Nakao, K. Yoneda, K. Manabu and N. Kobayashi, "Structures and Properties of an Ultra-Low-k Material: Classical-molecular-dynamics and First-principles Calculations," in *Materials Research Society Symposium Proceedings*, 2006.

[32] J. Zhang, R. Wu, M. Gao, J. Huang, Y. Wang, Z. Yu, Y. Ashizawa and H. Oka, "Atomistic Simulation of plasma enhanced chemical vapor deposited SiCOH dielectrics," in *IEEE Conference Proceedings*, 2006.

[33] N. Tajima, T. Ohno, T. Hamada, K. Yoneda, S. Kondo, N. Kobayashi, M. Shinriki, Y. Inaishi, K. Miyazawa, K. Sakota, S. Kasaka and M. Inoue, "Carbon-Doped Silicon Oxide Films with Hydrocarbon Network Bonds for Low-k Dielectrics: Theoretical Investigations," *Japanese Journal of Applied Physics,* vol. 46, no. 9A, pp. 5970-5974, 2007.

[34] D. D. Do, L. F. Herrera and H. D. Do, "A new method to determine pore size and its volume distribution of porous solids having known atomistic configuration," *Journal of Colloid and Interface Science,* vol. 328, pp. 110-119, 5 September 2008.

[35] L. F. Herrera, S. Junpirom, D. D. Do and C. Tangsathitkulchai, "Computer synthesis of char and its characterization," *Carbon,* vol. 47, pp. 839-849, 2009.

[36] K. T. Thomson and K. E. Gubbins, "Modeling Structural Morphology of Microporous Carbons by Reverse Monte Carlo," *Langmuir,* vol. 16, pp. 5761-5773, 9 February 2000.

[37] L. D. Gelb and K. E. Gubbins, "Characterization of Porous Glasses: Simulation Models, Adsorption Isotherms, and the BET Analysis Method," *Langmuir,* vol. 14, no. 8, pp. 2097-2111, 1998.

[38] R. S. Brusa, C. Macchi, S. Mariazzi and G. P. Karwasz, "Porosity of Low-k Materials Studied by Slow Positron Beam," *Acta Physica Polonica A,* vol. 107, no. 5, pp. 702-711, 2005.

[39] D. W. Gidley, W. E. Frieze, T. L. Dull, J. Sun, A. F. Yee, C. V. Nguyen and D. Y. Yoon, "Determination of pore-size distribtuion in low-dielectric thin films," *Applied Physics Letters,* vol. 76, no. 10, pp. 1282-1284, 6 March 2000.

[40] A. Grill, V. Patel, K. P. Rodbell, E. Huang, M. R. Baklanov, K. P. Magilnikov, M. Toney and H.-C. Kim, "Porosity in plasma enhanced chemical vapor deposited SiCOH dielectrics: A comparative study," *Journal of Applied Physics,* vol. 94, no. 5, pp. 3427-

3435, 1 September 2003.

[41] R. C. Hedden, H.-J. Lee and B. J. Bauer, "Characterization of Nanoporous Low-k Thin Films by Small-Angle Neutron Scattering Contrast Variation," *Langmuir,* vol. 20, pp. 416-422, 2004.

[42] N. Kemeling, K. Matsushita, N. Tsuji, K.-i. Kagami, M. Kato, S. Kaneko, H. Sprey, D. de Roest and N. Kobayashi, "A robust k ~2.3 SiCOH low-k film formed by porogen removal with UV-cure," *Microelectronic Engineering,* vol. 84, no. 11, pp. 2575-2581, 26 May 2007.

[43] Q. Wu and K. K. Gleason, "Plasma-enhanced chemical vapor deposition of low-k dielectric films using methylsilane, dimethylsilane, and trimethylsilane precursors," *Journal of Vacuum Socience Technology A - Vacuum, Surfaces, and Films,* vol. 21, no. 2, pp. 388-393, 17 January 2003.

[44] H. L. Xin, P. Ercius, K. J. Hughes, J. R. Engstrom and D. A. Muller, "Three-dimenstional imaging of pore structures inside low-k dielectrics," *Applied Physics Letters,* vol. 96, p. 223108, 2 June 2010.

[45] A. Grill and D. A. Neumayer, "Structure of low dielectric constant to extreme low dielectric constant SiCOH films: Fourier transform infrared spectroscopy characterization," *Journal of Applied Physics,* vol. 94, no. 10, pp. 6697-6707, 15 November 2003.

[46] H. Momida, T. Hamada and T. Ohno, "First-Principles Study of Dielectric Properties of Amorphous High-k Materials," *Japanese Journal of Applied Physics,* vol. 46, no. 5B, pp. 3255-3260, 2007.

[47] D. Vanderbilt, X. Zhao and D. Ceresoli, "Structural and dielectric properties fo crystalline and amorphous ZrO2," *Thin Solid Films,* no. 486, pp. 125-128, 2005.

[48] A. Courtot-Descharles, F. Pires, P. Paillet and J. L. Leray, "Density functional theory applied to the calculation of dielectric constant of low-k materials," *Microelectronics Reliability,* vol. 39, pp. 279-284, 20 July 1999.

[49] N. Basdevant, T. Haduong and B. Daniel, "Dielectric constant of a highly polarizable atomic fluid: the Clausius-Mossotti versus the Onsager relation," *Molecular Physics,* vol. 102, no. 8, pp. 738-788, 20 April 2004.

[50] S. J. Plimpton, "Fast parallel Algorithms for Short-Range Molecular Dynamics," *J Comp*

Phys, vol. 117, pp. 1-19, 1995.

[51] W. L. Jorgensen, D. S. Maxwell and J. Tirado-Rives, "Development and Testing of the OPLS All-Atom Force Field on Conformational Energetics and Properties of Organic Liquids," *J. Am. Chem. Soc.,* vol. 118, pp. 11225-11236, 1996.

[52] T. Watanabe, H. Fugiwara, H. Noguchi, T. Hoshino and I. Ohdomari, "Novel Interatomic Potenial Energy Function for Si, O Mixed System," *Jpn. J. Appl. Phys.,* vol. 38, pp. 366-369, 1999.

[53] H. S. Choi, T. Lee, H. Lee, J. Kim, K.-H. Hong, K. H. Kim, J. Shin, H. J. Shin, H. D. Jung and S. H. Choi, "Prediction of Young's Moduli of Low Dielectric Constant Materials by Atomistic Molecular Dynamics Simulation," in *Materials Research Society Symposium Proceedings,* 2006.

[54] D. J. Earl and W. M. Deem, "Parallel tempering: Theory, applications, and new perspectives," *Phys. Chem. CHem. Phys.,* vol. 7, pp. 3910-3916, 2005.

[55] M. Eleftheriou, A. Rayshubski, J. W. Pitera, B. G. Fitch, R. Zhou and R. S. Germain, "Parallel Implementation of the Replica Exchange Molecular Dynamics Algorithm on Blue Gene/L," in *Parallel and Distributed Processing Symposium, 2006.,* 2006.

[56] J. M. Knaup, H. Li, J. J. Vlassak and E. Kaxiras, "Influence of CH2 content and network defects on the elastic properties of organosilicate glasses," *Phys Rev B,* vol. 83, pp. 054204.1-7, 2011.

[57] L. Pauling, "Atomic Radii and Interatomic Distances in Metals," *Journal of the American Chemical Society,* vol. 69, no. 3, pp. 542-553, 1947.

[58] V. M. Burlakov, Y. Tsukahara, G. A. D. Briggs and A. P. Sutten, "Monte Carlo Simulation of Vapour Deposition of Nonstoichiometric Amorphous Silica," *Materials Research Society Symposium Proceedings,* vol. 648, pp. 1-8, 2001.

[59] M. J. Frisch, G. W. Trucks, H. B. Schlegel, G. E. Scuseria, M. A. Robb, J. R. Cheeseman, G. Scalmani, V. Barone, B. Mennucci, G. A. Petersson, H. Nakatsuji, M. Caricato, X. Li, H. P. Hratchian, A. F. Izmaylov, J. Bloino, G. Zheng, J. L. Sonnenberg, M. Hada, M. Ehara, K. Toyota, R. Fukuda, J. Hasegawa, M. Ishida, T. Nakajima, Y. Honda, O. Kitao, H. Nakai, T. Vreven, J. J. A. Montgomery, J. E. Peralta, F. Ogliaro, M. Bearpark, J. J. Heyd, E. Brothers, K. N. Kudin, V. N. Staroverov, R. Kobayashi, J. Normand, K. Raghavachari, A. Rendell, J. C. Burant, S. S. Iyengar, J. Tomasi, M. Cossi, N. Rega, N. J. Millam, M. Klene, J. E. Knox, J. B. Cross, V. Bakken, C. Adamo, J. Jaramillo, R. Gomperts, R. E. Stratmann, O. Yazyev, A. J. Austin, R. Cammi, C. Pomelli, J. W.

Ochterski, R. L. Martin, K. Morokuma, V. G. Zakrzewski, G. A. Voth, P. Salvador, J. J. Dannenberg, S. Dapprich, A. D. Daniels, O. Farkas, J. B. Foresman, J. V. Ortiz, J. Cioslowski and D. J. Fox, "Gaussian 09, Revision A.1," Wallingford CT, 2009.

[60] A. D. Becke, "Density-functional thermochemistry. III. The role of exact exchange.," *Journal of Chemical Physics,* vol. 98, pp. 5648-5652, 1993.

[61] J. P. Perdew, "Density-functional approximation for the correlation energy of the inhomogeneous electron gas," *Physics Review B,* vol. 23, pp. 5048-5079, 1981.

[62] A. D. Boese and J. M. L. Martin, "Development of Density Functionals for Thermochemical Kinetics," *Journal of Chemical Physics,* vol. 121, pp. 3405-16, 2004.

[63] J. Heyd and G. E. Scuseria, "Assessment and validation of a screened Coulomb hybrid density functional," *Journal of Chemical Physics,* vol. 120, p. 7274, 2004.

[64] J. Heyd and G. Scuseria, "Efficient hybrid density functional calculations in solids:The HS-Ernzerhof screened Coulomb hybrid functional," *Journal of Chemical Physics,* vol. 121, pp. 1187-1192, 2004.

[65] J. Heyd, J. E. Peralta, G. E. Scuseria and R. L. Martin, "Energy band gaps and lattics parameters evaluated with the Heyd-Scuseria-Ernzerhof screened hybrid functional," *Journal of Chemical Physics,* vol. 123, pp. 174101: 1-8, 2005.

[66] Y. Zhao and D. G. Truhlar, "The M06 suite of density functional for main group thermochemistry, thermochemical kinetics, noncovalent interactions, excited states, and transition elements: two new functionals and systematic testing of four M06-class functionals and 12 other functions," *Theor. Chem. Acc.,* vol. 120, pp. 215-241, 2008.

[67] X. Xu and W. A. Goddard III, "The X3LYP extended density functional for accurate descriptions of nonbond interactions, spin states, and thermochemical properties," *Proc. Natl. Acad. Sci.,* vol. 101, pp. 2673-2677, 2004.

[68] J. P. Perdew, K. Burke and M. Ernzerhof, "Generalized Gradient Approximation Made Simple," *Physical Review Letters,* vol. 77, no. 18, 1996.

[69] C. Adamo and V. Barone, "Toward reliable density functional methods without adjustale parameters: the PBE0 model," *J. Chem. Phys,* vol. 110, pp. 6158 -6169, 1999.

[70] M. Head-Gordon, J. A. Pople and M. J. Frisch, "MP2 energy evalution by direct methods," *Chemical Physics Letters,* vol. 153, pp. 503-506, 1988.

[71] J. S. Binkley, J. A. Pople and W. J. Hehre, "Self-Consistent Molecular Orbital Methods, 21. Small Split-Valence Basis Sets for First-Row Elements," *J. Am. Chem. Soc.,* vol. 102, pp. 939-947, 1980.

[72] A. D. McLean and G. S. Chandler, "Contracted Gaussian-basis sets for molecular calculations. 1. 2nd row atoms, Z=11-18," *J. Chem. Phys.,* vol. 72, pp. 5639-5648, 1980.

[73] P. J. Hay and W. R. Wadt, "Ab initio effective core potentials for molecular calculations - potentials for the transition-metal atoms Sc to Hg," *J. Chem. Phys.,* vol. 82, pp. 270-283, 1985.

[74] J.-H. Lii and N. L. Allinger, "Molecular Mechanics. The MM3 Force Field for Hydrocarbons. 3. The van der Waals' Potentials and Crystal Data for Aliphatic and Aromatic Hydrocarbons," *Journal of the American Chemical Society,* vol. 111, pp. 8576-8582, 1989.

[75] J. W. Ponder, "Tinker: User Guide," May 21 2010. [Online]. Available: http://dasher.wustl.edu/tinker/. [Accessed 2 August 2010].

[76] H. B. Schlegel, "Optimization of Equilibrium Geometries and Transition Structures," *Journal of Computational Chemistry,* vol. 3, pp. 214-218, 1982.

[77] "Avogadro: an open-source molecular builder and visualization tool. Version 1.0.1".

[78] "Materials 2: the solid state," in *Atkins' Physical Chemistry*, 8th ed., New York, NY: Oxford University Press, 2006, pp. 697-739.

[79] A. C. T. van Duin, S. Dasgupta, F. Lorant and W. A. Goddard III, "ReaxFF: A Reactive Force Field for Hydrocarbons," *J. Phys. Chem. A,* vol. 105, no. 41, pp. 9396-9409, 2001.

[80] W. A. Goddard III, Q. Zhang, M. Uludogan, A. Strachan and T. Cagin, "The ReaxFF Polarizable Reactive Force Fields for Molecular Dynamics Simulation of Ferroelectrics," in *AIP Conference Proceedings*, 2002.

[81] W. A. Goddard III, A. van Duin, K. Chenoweth, M.-J. Cheng, S. Pudar, J. Oxgaas, B. Merinov, Y. H. Jang and P. Persson, "Development of the ReaxFF reactive force field for mechanistic studies of catalytic selective oxidation processon BiMoOx," *Topics in Catalysis,* vol. 38, pp. 93-103, 2006.

[82] K. Chenoweth, A. C. van Duin and W. A. Goddard III, "ReaxFF Reactive Force Field for Molecular Dynamics Simulations of Hydrocarbon Oxidation," *J. Phys. Chem. A,* vol. 112, pp. 1040-1053, 2008.

[83] K. Joshi, A. C. van Duin and T. Jacob, "Development of a ReaxFF description of gold oxides and inital applications to cold welding of partially oxidized gold surfaces," *J. Mater. Chem.,* vol. 20, pp. 10431-10437, 2010.

[84] L. Huang, K. L. Joshi, A. C. van Duin, T. J. Bandosz and K. E. Gubbins, "ReaxFF molecular dynamics simulation of thermal stability of a Cu3(BTC)2 metal-organic framework," *Phys. Chem. Chem. Physis.,* vol. 14, pp. 11327-11332, 2012.

[85] J. A. Keith, D. Fantauzzi, T. Jacob and A. C. van Duin, "Reactive forcefield for simulating gold surfaces and nanoparticles," *Physical Review B,* vol. 81, pp. 2354041-2354048, 2010.

[86] T. T. Jarvi, A. C. van Duin, K. Nordlund and W. A. Goddard, III, "Development of Interatomic ReaxFF Potentials for Au-S-C-H Systems," *J. Phys. Chem. A,* vol. 115, pp. 10315-10322, 2011.

[87] O. Rahaman, A. C. van Duin, W. A. Goddard III and D. J. Doren, "Development of a ReaxFF Reactive Force Field for Glycine and Application to Solvent Effect and Tautomerization," *J Phys Chem B,* vol. 115, pp. 249-261, 2011.

[88] S. R. Phillpot and S. B. Sinnott, "Simulating Multifunctional Structures," *Science,* vol. 325, pp. 1634-1635, 2009.

[89] A. Cooper Raymunt and P. Clancy, "Structural Characterization of Amorphous Materials Applied to Low-k Organosilicate Materials," *Thin Solid Films,* vol. 562, pp. 411-422, 2014.

[90] A. Cooper and P. Clancy, "Parameter-free correlation for a composition-based prediction of the dielectric constant of amorphous organosilicate materials," *Molecular Simulation,* vol. 38, pp. 1221-1233, 2012.

[91] M. I. Ojovan, "Glass Formation in Amorphous SiO2 as a Percolation Phase Transition in a System of Network Defects," *JETP Letters,* vol. 79, no. 12, pp. 632-634, 2004.

[92] H. P. Hentze and M. Antonietti, "Template synthesis of porous organic polymers," *Current Opinion in Solid State and Materials Science,* vol. 5, pp. 343-353, 2001.

[93] S. Jiang, K. E. Jelfs, D. Holden, T. Hasell, S. Y. Chong, M. Haranczyk, A. Trewin and A. I. Cooper, "Molecular Dynamics Simulations of Gas Selectivity in Amorphous Porous Molecular Solids," *Journal of the American Chemical Society,* vol. 135, pp. 17818-17830, 2013.

[94] J. L. Novotney and W. R. Dichtel, "Conjugated Porous Polymers for TNT Vapor

Detection," *ACS Macro Letters,* vol. 2, pp. 423-426, 2013.

[95] J.-H. Yim, Y.-Y. Lyu, H.-D. Jeong, S. A. Song, I.-S. Hwang, J. Hyeon-Lee, S. K. Mah, S. Chang, J.-G. Park, Y. F. Hu, J. N. Sun and D. W. Gidley, "The Preparation and Characterization of Small Mesopores in Siloxane-Based Materials That Use Cyclodextrins as Templates," *Advanced Functional Materials,* vol. 13, no. 5, pp. 382-386, May 2003.

[96] C.-X. Yang, C. Zhang, Q.-Q. Sun, S.-S. Xu, L.-F. Zhang, Y. Shi, S.-J. Ding and W. Zhang, "Prepartion of Ultra Low-k Porous SiOCH Films from Ring-Type Siloxane with Unsaturated Hydrocarbon Side Chains by Spin-On Deposition," *Chin. Phys. Lett.*, vol. 27, pp. 0277011-0277013, 2010.

[97] A. M. Urbanowicz, K. Vanstreels, P. Verdonck, E. Van Besien, C. Trompoukis, D. Shamiryan, S. De Gendt and M. R. Baklanov, "Effect of UV Wavelength on the hardening process of porogen-containing and porogen-free ultralow-k plasma-enhanced chemical vapor deposition dielectrics," *Journal of Vacuum Science and Technology B*, vol. 29, p. 032201, 2011.

[98] J. P. Perdew, K. Burke and M. Ernzerhof, "Generalized gradient approximation made simple," *Physics Review Letters,* vol. 77, pp. 3865-3868, 1996.

[99] H. G. P. Lewis, T. B. Casserly and K. K. Gleason, "Hot-Filament Chemical Vapor Deposition of Organosilicon Thin Films from Hexamethylcyclotrisiloxane and Octamethylcyclotetrasiloxane," *Journal of The Electrochemical Society*, vol. 148, no. 2, pp. F212-F220, 2 November 2001.

[100] "Matter Polarization and Relative Permittivity," in *Principles of Electronic Materials and Devices*, 3rd ed., New York, NY: McGraw Hill, 2006, pp. 584-594.

[101] C. Jin, S. Lin and J. T. Wetzel, "Evaluation of Ultra-Low-k Dielectric Materials for Advanced Interconnects," *Journal of Electronic Materials,* vol. 30, no. 4, pp. 284-289, 16 January 2001.

[102] K. Iyengar, B. Jung, M. Willemann, P. Clancy and M. O. Thompson, "Experimental determination of thermal profiles during laser spike annealing with quantitative comparison to 3-dimensional simulations," *Applied Physics Letters,* vol. 100, p. 211915, 2012.

[103] K. A. Iyengar, P. Clancy and M. O. Thompson, "A 3D model for simulating temperature and stress profiles during sub-millisecond laser spike annealing," in *Advanced Thermal Processing of Semiconductors (RTP), 2010 18th International Conference on*, Gainesville,

FL, 2010.

[104] W. Humphrey, A. Dalke and K. Schulten, "VMD - Visual Molecular Dynamics," *J. Molec. Graphics*, vol. 14, pp. 33-38, 1996.

[105] C. Guedj, G. Imbert, E. Martinez, C. Licitra, N. Rochet and V. Arnal, "Modification of porous ultra-low k dielectric by electron-beam curing," *Microelectronics Reliability*, vol. 47, no. 4-5, pp. 764-768, 20 February 2007.

[106] H. Dorsett and A. White, "Overview of Molecular Modelling and Ab initio Molecular Orbital Methods Suitable for Use with Energetic Materials," DSTO Aeronautical and Maritime Research Laboratory, Salisbury South Australia, 2000.

[107] M. R. Baklanov, J.-F. de Marneffe, D. Shamiryan, A. M. Urbanowicz, H. Shi, T. V. Rakhimova, H. Huang and P. S. Ho, "Plasma processing of low-k dielectrics," *Journal of Applied Physics*, vol. 113, p. 041101, 2013.

[108] M. P. Allen and D. J. Tildesley, Computer Simulation of Liquids, New York: Oxford University Press, 1987, p. 21.